Investigation of the Copper Metallic Content in Plasma Activated Water from the Electrode Erosion in a Pin-to-Liquid discharge system

Simon Nicolas Dib

McGill University
Montreal QC, Canada

August 2020

A thesis submitted to McGill University in partial fulfillment
of the requirements for the degree of
Master of Engineering

© Simon Nicolas Dib, 2020

Abstract

When it comes to non-thermal plasmas, many questions are, to this day, left unanswered primarily because of the many diverse configurations they can adopt. Due to their extremely small mass, electrons are inefficient at transferring kinetic energy to heavy particles and ultimately to the walls confining the plasma volume. Therefore, non-thermal plasmas implement high reactivity environments at approximately room temperature, which is very advantageous especially when it comes to treating temperature-sensitive materials. Specifically, in a pin-to-water non-thermal plasma configuration, chemical reactions and physical morphologies that are unconventional at room temperature become realized, such as the generation of reactive oxygen and/or nitrogen species (RONS) and the induction of cathodic erosion.

Unlike RONS, cathodic erosion in a pin-to-water plasma system has almost been completely unventured. It proposes a method of metal deposition into water and creates a synergistic effect due to its coexistence with RONS. The synergistic effect applies to the plasma activated water (PAW), whereby aqueous metallic ions and solid metallic particles are deposited as a result of erosion caused by plasma discharges over a water surface. In order to comprehend the role metals play, the goal of this thesis has been to characterize the metal content of PAW and study the effect of different plasma atmospheres on the levels of erosion, which are correlated to metal deposition. Due to its non-refractory properties as well as its known cytotoxic and antibacterial potency, pure copper has been chosen as the cathode material in the plasma system. Using differential pulse anodic stripping voltammetry (DPASV), analyses were carried out to determine the cupric ion content of PAW in three different gaseous atmospheres for plasma generation, namely air, oxygen and argon. Then, particle size analyses (PSA) were performed using dynamic light scattering (DLS) to obtain an average diameter size for the copper nanoparticles formed. Erosion crater morphology and elemental composition were detected and justified through scanning electron microscopy (SEM) imaging accompanied by energy-dispersive X-ray spectroscopy (EDS) analyses.

The SEM results show erosion and crater-like copper erosion profiles for all three gases, with air yielding the highest levels of erosion and unstructured surface morphology, and argon the least levels of erosion with the most homogeneous surface morphology. The DPASV analysis of PAW in air, determined a cupric concentration 0.0928 µM, while the total copper content (obtained via inductively coupled plasma – optical emission spectroscopy (ICP-OES)) was found to be 15.736 µM (1 mg/L). This, in turn, yielded a copper ion:nanoparticle ratio of 0.00590 in air with nanoparticle content dominating. The total copper content for PAW in oxygen, at 0.12 mg/L, was less than that in air, proving the positive correlation between erosion levels and total copper content. Finally, from the PSA-DLS analyses complimented by transmission electron microscopy (TEM) imaging, copper particles within PAW in air were concluded to have the largest average diameter size at ~ 2 µm, and in oxygen the smallest at ~ 200 nm.

Abrégé

La discussion des plasmas non-thermiques porte à plusieurs questions ouvertes de nos jours. Ceci est explicable en raison de leur adaptation de plusieurs états. Le fait que l'équilibre du plasma chaud est difficile à atteindre, pose la question : Pourquoi s'en faire lorsque le plasma non-thermique est connue pour être un composant extrêmement réactif? Le transfert de l'énergie cinétique entre les électrons et leurs paires lourdes est inefficace à cause de la grande différence entre leurs masses. Effectivement, l'énergie transféré aux bordures qui confine le volume du plasma est négligeable. Ainsi, le traitement des matériaux sensible à la température, y compris le plasma non-thermique, dans un environnement d'une température ambiante encourage leurs états réactifs. Donc, les réactions chimique et morphologie physique qui sont autrement inconvénients dans une température ambiante seront réalisées spécifiquement dans une configuration eau-à-broche, où les espèces d'oxygène et/ou de nitrogène réactifs (EONR) sont générer, y compris l'induction de l'érosion cathodique.

Contrairement au EONR, l'érosion cathodique dans un system de plasma en configuration eau-à-broche a été nullement exploré. La proposition comprend d'une méthode de disposition métallique dans l'eau qui mène à un effet synergétique lors d'une coexistence avec les EONR. L'application de cet effet, autrement eau activée par plasma (EAP), est parmi le dépôt des ions métalliques aqueuses et leurs particules métalliques. Le but de cette thèse et justifiée dans les effets d'une atmosphère de plasma et le niveau d'érosion lors d'un contenu métallique de l'EAP, qui mène à la compréhension du rôle des métaux dans cette application. En raison de ses propriétés non-réfractives ainsi que de sa puissance cytotoxique et antibactérienne connue, le cuivre est sélectionné comme le métal cathodique dans l'environnement de plasma. Utilisant une voltampérométrie de dénudage anodique à impulsions différentielles (VDAID), l'analyse de

l’EAP contenue des ions cuivriques est exécuter dans trois environnements gazeuses différentes, compris d’aire, oxygène, et argon. Par la suite, des analyses granulométriques (AG) ont mesuré le diamètre en moyenne des nanoparticules obtenues dans chaque environnement d’EAP par la technique instrumentale de diffusion de lumière dynamique (DLD). L'érosion et la morphologie cathodique ont été détectées et justifiées quant à imagerie par microscopie électronique à balayage (MEB) accompagnée d'analyses par spectroscopie à rayons X à dispersion d'énergie (ASD).

Les résultats MEB démontrent de l’érosion dans la morphologie cathodique de cuivre dans les trois gazes, dont l’aire atteint le plus haut niveau d’érosion et destruction de la morphologie de la surface, et l’argon démontre le moindre d’érosion où la surface demeure hémogénique. L’analyse VDAID de l’EAP dans l’aire détermine une concentration des ions cuivriques de 0.0928 µM, dont le contenue de cuivre (obtenu par plasma à couplage inductif - spectroscopie d'émission optique (PCI-SEO)) demeure à 15.736 µM (1 mg/L). Ainsi, le ratio d’ion:nanoparticule de 0.00590 dans l’aire a été conclu de laquelle les nanoparticules demeurent dominantes. Le contenu total de cuivre de l’EAP dans l’oxygène demeure à 0.12mg/L, étant moins que la concentration dans l’aire, qui confirme la relation positive entre le niveau d’érosion et le contenu de cuivre total. Finalement, à l’aide de l’analyse d’imagerie par microscopie électronique à transmission (MET) accompagner par les AG-DLD, il est conclu que les particules en cuivre dans l’environnement de l’EAP dans l’aire ont en moyenne un plus grand diamètre tenue à ~ 2 µm, contrairement à l’oxygène qui tient la plus petite moyenne à ~ 200 nm.

L’application du cuivre-EAP sert utile dans les domaines médicaux étant dit les secteurs d’oncologie sans avoir la connaissance de leurs interactions avec des mécanismes biologiques. Récemment, des études ont déduit la synergie entre la coexistence des EONR et le cuivre, dont cette thèse servira à la compréhension de la nature de cette paire.

Acknowledgments

To begin, I would really like to thank my primary supervisor, Professor Sylvain Coulombe, who opened doors of hope for me when all others had closed them. You gave me an opportunity to show how serious and hardworking I am and put value to my contributions in your laboratory. You proved to me that people can indeed merit from being true and honourable in life. Working with you these past two years has taught me to believe more in myself and trust the decisions I make. My level of self-confidence would not be where it is today if it weren't for your guidance and moral support. Additionally, the scientific and laboratory experiences you have exposed me to have been so phenomenal and fruitful. I have learned so much and will hold on to this knowledge throughout the course of my professional life. Once again, my deepest and sincerest gratitude.

Secondly, my thanks also go to my co-supervisor, Professor Philip Wong. You have added to my graduate experience by allowing me to collaborate with biologists and biophysicists. The integration of my work in the medical field has been a great learning experience, one which I had been so ignorant about. I thank you as well for making me feel welcome into your laboratory at the Research Center of CHUM, even though the majority of my work was conducted at McGill University.

I would like to acknowledge the funding sources that have enabled my work to flourish: The Eugenie Ulmer Lamothe Graduate Award and the CR-CHUM Graduate Assistance Award. From the Department of Chemical Engineering's technical staff, my thanks go to Andrew, Ranjan, Lou, Roberto, Gerald and most importantly Frank, who was very patient with my initial incompetence in general laboratory skills. Thanks Frank! And hope I did you proud at the end.

To all my colleagues and friends in the Plasma Processing Laboratory (PPL), especially Elena Corella Puertas and Elmira Pajootan. To Elena: You have been more than just a mentor to me but also an amazing friend. You have made feel welcome to the group at the beginning of my graduate journey, which is a kindness I will never forget. My research had excelled at an unimaginable level because of you, and I would be very proud of myself if my work met even a quarter of your expectations. Thank you for all the moral support you have given me, but most of all thank you for our new-found friendship. To Elmira: my research would have failed if it wasn't for your guidance and intellectuality, period. You have helped me overcome so many scientific obstacles that, from hindsight, I would have never been able to conquer on my own. You are such a professional at what you do and wish you the brightest and most successful future.

Lastly, I would like to thank my family: To my parents, Nicolas and Gisèle, thank you for always checking up on me day in and day out and constantly caring and worrying for me throughout my degree. My thoughts of the both of you have always pulled me back up during my moments of weakness and have encouraged me to never give up and to always chase after my dreams. To my sisters, Justine and Cybelle, thank you for being everlasting role models to me and helping me not to succumb to my mental health issues, something I have been struggling with ever since I left home. Because of you it has gradually been ameliorating, and through the mentally and physically demanding end of my degree, both of you have made it feel so effortless with no decadence to my progress. To my best/childhood friends, Hani, Hanna and Ramsey, thank you for always being present at the end of the road and helping me forget my worries and problems in life. The three of you have always been my escape from reality and the struggles of adulthood.

My time away from home and everyone was a bittersweet experience, and now I yearn to reunite with everybody and make up for all the time lost. Life is too short.

Table of Contents

Abstract ………………………………………………………………………………. **I**

Abrégé ………………………………………………………………………………. **III**

Acknowledgments ……………………………………………………………………. **V**

1 Introduction …………………………………………………………………….. **1**

1.1 Objectives ……………………………………………………………………. **2**

2 Literature Review ……………………………………………………………… **3**

2.1 Preface ………………………………………………………………………. **3**

2.2 The Plasma State ……………………………………………………………. **4**

2.2.1 Introduction to Plasma ……………………………………………….... **4**

2.2.2 Gas-Phase Plasma in Direct contact with a Liquid Electrode ………. **5**

2.2.3 Plasma Transitions: Pulsed Corona Discharges (PCDs) in Question . **9**

2.3 The Major Consequences of a Pin-to-Water Surface Plasma Discharge …….. **12**

2.3.1 Plasma Chemistry: Formation of Oxidizing and Reactive Species ... **12**

2.3.2 Cathode Electrode Erosion in Plasma Systems …………………….. **15**

2.4 Copper: An Excellent Cathode Candidate …………………………………… **18**

2.4.1 The Physical and Chemical Properties of Copper …………….….. **18**

2.4.2 Overview of Copper in Cancer and Microbial Biology……..…..…..... **20**

2.5 Experimental Background …………………………………………………….. **22**

2.5.1 Electrochemistry: Metal Ion Concentration Analysis via Anodic Stripping Voltammetry ……………………………………………… **22**

2.5.1.1 The Levich and Cottrell Equations ………………………….. **26**

2.5.2 Particle Size Analysis: Metal Nanoparticle Characterization and Control ………………………………………………………………… **27**

2.5.2.1 Laser Diffraction Technique: Origins behind Volume Distributions …………………………………………………... **30**

2.5.2.2 Dynamic Light Scattering: Intensity Distributions ………… 31

3 Experimental Methods ……………………………………………………………… 34

3.1 Preface ………………………………………………………………………... 34

3.2 The Pin-to-Water Nonthermal Plasma Setup: PAW Sample Preparation …..... 34

3.2.1 Overall Experimental Configuration ……………………………... 34

3.2.2 Plasma Reactor Vessel Setup …….………………………………... 35

3.2.3 Electrical Mechanism and Conditions ……………………………… 38

3.3 Differential Pulse Anodic Stripping Voltammetry Setup: Copper Ion Analysis 41

3.3.1 Overall Experimental Configuration ……………………………... 41

3.3.2 External Standards Method:Construction of the Calibration Curve 42

3.3.3 Electrical Optimization and Specifications of the ASV Setup ..……. 45

3.3.3.1 Gold Working Electrode Polishing ………………………….. 46
3.3.3.2 Gold Surface Activation or Cleaning via Cyclic Voltammetry (CV) ………………………………………………………… 47
3.3.3.3 Differential Pulse Voltammetry vs. Linear Sweep Voltammetry ………………………………………………... 55
3.3.3.4 Deposition Voltage and Accumulation Time Optimization ... 61

3.4 Malvern Zetasizer Nano ZS: Copper Nanoparticle Size Analysis …………….. 64

3.4.1 General Experimental Configuration ……………………………….. 64

3.4.2 PAW Sample Interpretation, Preparation and Insertion ………….. 66

3.4.3 Standard Operating Procedure (SOP) Measurement ……………… 67

3.5 Other Characterization Techniques ……………………………………………... 69

4 Results and Discussion ……………………………………………………………… 70

4.1 Preface ………………………………………………………………………... 70

4.2 Copper Cathode Imaging: Visualizing Electrode Erosion and Morphology …. 70

4.3 Copper Content Results in PAW …………………………………………………. 75

4.3.1 Copper Ion Content in PAW in an Air Atmosphere ……………….. 75

4.3.2 Comparisons to Total Copper Content Results obtained via ICP-OES ………………………………………………………………. 80

4.4 Copper Nanoparticle Analysis Results ………………………………………….. 82

4.4.1 PSA-DLS Data Results: Size Distribution Analysis of Copper Nanoparticles in PAW ………………………………………………... 82

4.4.2 TEM Imaging of the Copper Nanoparticles ………………………… 89

5 Conclusion and Future Work ……………………………………………………… 93

5.1 Conclusion and Ongoing Work ……………………………..………………… 93

5.2 Future Work and Recommendations …………………………………………… 95

6 Appendix …………………………………………………………………………... 96

6.1 MATLAB code for the External Standards Methods used in cupric ion analysis ……………………………………………………………………….. 96

6.2 Average PDIs of the Copper Nanoparticles found with 3 types of gases …..… 100

6.3 Diffractograms of the TEM Images in Section 4.4.2 …………………………... 101

7 References …………………………………………………………………………... 102

List of Figures

Figure 1: Schematic of different discharges used in plasma-liquid interactions: (A) direct discharge in liquid, (B)-(D) gas phase discharges and (E) and (F) multiphase discharges. In more detail: (B) plasma jet without direct contact with liquid, (C) gas phase plasma with liquid electrode, (D) surface discharge, (E) gas phase plasma with dispersed liquid phase (aerosols) and (F) discharges in bubbles. Blue = liquid, pink = plasma, green = dielectric, black = metal electrodes. 6

Figure 2: DC driven air glow discharge in a pin-water geometry with self-organization at the surface of the water anode electrode. 7

Figure 3: (a) Taylor cone before breakdown, (b) and (c) Taylor cone at breakdown for negative and positive polarity of the metal pin respectively. In the lower right corner of each image the time to or after spark formation is noted assuming t = 0 is the moment of spark formation. The lower left corner is the shutter opening time, and the metal electrode polarity is indicated in each image. 8

Figure 4: (a)-(b) streamer-to-spark transition, with water cathode (bottom) and pin anode electrodes (top) (c)-(i) glow-to-spark transition with water anode (bottom) and pin cathode electrodes (top). The lower right and left annotations of each image are representations of the same parameters as described in Figure 3. In all cases, the inter-electrode distance is 7 mm and the pin electrode radius is 0.5 cm. 10

Figure 5: The voltage-current characteristic of a DC low pressure electrical discharge. 12

Figure 6: Overview of important reactions in air plasma-water anode interaction. 13

Figure 7: Current density produces from the surface of a metal electrode as a function of surface temperature and field strength. 17

Figure 8: Graphical comparison of the Fraunhofer Approximation and the Mie theory based on the analysis of a single identical sample. 31

Figure 9: A general instrumental layout of the DLS technique. The laser is used as the light source to illuminate the sample cell. Scattered light is detected by one of two detectors: either a right angle detector or a 173 degree back angle detector. 32

Figure 10: Top graph shows light scattering fluctuations and bottom graph shows how the autocorrelation function converts the top graph as a function of delay time. 33

Figure 11: Schematic of the pin-to-water non-thermal plasma system/reactor. The copper pin cathode is designated by the negative polarity and the submerged stainless-steel anode sparger is designated by the positive polarity. The white circles represent the gas bubbles erupting from the sparger and supplied by the gas cylinder. The zoomed-in portion of the figure shows the gas-liquid interface where a violet plasma discharge originates from the cathode and branches on the water surface. The orange-brown circles represent the copper content transferred into the water via mass transfer. Those with positive signs denote cations and those with no signs denote nanoparticles. It is important to note that this entire schematic is not to scale and the bubble density as well as the ion:nanoparticle ratio are not accurate either. 35

Figure 12: Overall picture of plasma reactor vessel. The column on the far left is the flow meter and the electrical box behind the reaction vessel is the nanosecond pulser with two high voltage probes seated on the top of the box. The elephant trunk (upper right corner) is connected to the fume hood exhaust; this is what the gas line containing exiting gas leads into. 38

Figure 13: The voltage and current profile of a plasma discharge over water using a copper pin cathode in air. The electrical conditions include nanosecond pulses at 3 kHz and a total peak-to-peak voltage drop of 12 kV. 39

Figure 14: The electrical setup with all the electrical components connected to the plasma reactor vessel through the nanosecond pulser. The oscilloscope reads the electrical signals of the voltage pulses at both polarities of the nanosecond pulser. This was used for constantly monitoring the voltage and making sure that the graphs are identical during every PAW sample preparation (no electrical differences between samples). 40

Figure 15: Plasma reactor during a sample preparation in air atmosphere. Violet plasma discharge is seen in the zoomed-in portion of the pin copper cathode millimeters above the RO water surface. 41

Figure 16: Full ASV setup. The electrical box on the right of the computer screen is the potentiostat (an instrument that applies voltage sweeps across electrodes). The glass funnel shaped beaker holds the PAW sample with the electrodes dipped into it. It is where the electrochemical reactions take place. The computer processes the electrical data and converts it into voltage and current plots based on what is desired. The electrochemical software used is NOVA from Metrohm Autolab. 42

Figure 17: (A) Exhibits contamination peaks in a gold working electrode cyclic voltammogram with a sulfuric acid solution of 1 M, and (B) exhibits the same as (A) but in a sulfuric acid solution of 0.5 M. Note that only the last CV scan of 20 is graphed in both cases. Both CVs had a scan rate of 0.1 V/s. 50

Figure 18: (A) Demonstrates how the cyclic voltammogram of the gold working electrode evolves from a bare polycrystalline profile (scan 1) to one with low-index crystal planes (scan 20). It is experimentally seen that the transition is usually complete by the 10th scan with all the scans from 10 to 20 overlapping (completely identical). (B) Demonstrated a cyclic voltammogram of the working electrode starting and ending with an LICP profile. (C) Demonstrates the evolution of current with time at an applied voltage. Used to reduce the hydrous gold oxide layer back to gold. The tendency of current to 0 A is a crucial characteristic telling us that no new phenomenon is being oxidized and reduction processes are halting (in this case). 53

Figure 19: Shows how staircase voltammetry is derived from linear sweep voltammetry. While linear sweep voltammetry measures current at every point in time, staircase voltammetry gives time for non-faradaic currents to sufficiently recede before recording a current measurement. 56

Figure 20: Shows the construction of DPV from linear and staircase voltammetry where E denotes the potential. The side image on the right shows what is happening in parallel to the voltage pulse in terms of current with respect to time. It explains how non-faradaic readings are minimized based on the sampling periods' positionings in time. 57

Figure 21: (A) Shows the change in current during the deposition process. (B) Observation of the stripping peak after running a DPASV on standard (S2) and a blank with a deposition voltage of – 0.3 V and an accumulation time of 150 s. 59

Figure 22: (A) Shows the output of the optimization procedure for the reduction voltage of copper on the gold electrode. (B) Shows the output of the optimization procedure for the accumulation time of copper on the gold electrode. 62

Figure 23: Schematic of the DPASV experimental setup. The whole figure on the left represents a standard solution being analyzed. The three stick-like figures are the electrodes: right = gold working electrode, center = SCE, left = graphite counter electrode. The orange-brown dots depict the cupric ions in solution diffusing. When the reduction voltage is applied for the duration of the accumulation time, the cupric ions will diffuse towards the active surface area of the gold electrode (yellow region) (top right zoomed in portion). The zoomed in portion of the active surface area on the bottom right demonstrates the deposition of the cupric ions onto the surface and being reduced into copper metal to form a metal layer (orange dots do not have + signs). The first version of the zoomed in portion (top right) simultaneously demonstrates the stripping/oxidation step (which follows the deposition step) of the metal copper layer back to cupric ions that will diffuse back into the bulk of the solution (orange dots get back their + signs) once DPASV is run. 63

Figure 24: Live picture during the DPASV analysis of a random PAW sample. This funnel shaped beaker is purposely used for the analysis of liquid samples that are of small volumes. The electrode holder is custom made teflon. 64

Figure 25: A schematic of the DLS setup within the Malvern Zetasizer Nano ZS/S and Nano S90/ZS90. Configuration (A) represents the DLS setup we are interested in with a 175° detection optic (also known as backscatter detection). 65

Figure 26: Estimate plot determining the minimum amount of particle number for different analyte concentrations required with respect to the particle diameter detected. The density of the solvent/dispersant for this plot is assumed to be 1g/cm^3. 67

Figure 27: SEM images of the copper pin cathode tips pre and post plasma treatment for each type of gaseous atmosphere: air, oxygen and argon. 71

Figure 28: Zoomed-in versions of the SEM images captured in Figure 27 of the copper cathode pin post plasma treatment in air, oxygen and argon, along with an overall respective EDS analysis. 72

Figure 29: The overlaid plots of all the average stripping currents of the copper standards; obtained from DPASV analysis. 76

Figure 30: Calibration Curve based on the results from Figure 29. Showing the best fit linear trend line correlation between stripping current peaks and concentration (Error bars are included). The blue dots represent standard solutions and the green dot represents the average value of all analyzed air-PAW samples with horizontal error bars. It is important to note that the green dot does not contribute to the trend line. 78

Figure 31: This is an overlaid plot of the average stripping currents of all three air-PAW samples as a result of DPASV analyses. 79

Figure 32: Results of the total copper content in air-PAW and oxygen-PAW obtained via ICP-OES. The top row represents oxygen and the bottom air. The left column shows the results for every PAW sample at each respective treatment time (4 different samples per treatment time); black circles represent outliers and white circles represent valid trials. The right column shows the average results of all valid samples for each treatment time, with added error bars. 82

Figure 33: Particle size distribution of copper nanoparticles in 3 different argon-PAW samples based on percentage volume (a-c) and percentage intensity (d-f). 83

Figure 34: Particle size distribution of copper nanoparticles in 3 different air-PAW samples based on percentage volume (a-c) and percentage intensity (d-f). Signals below 10 nm were ignored. 85

Figure 35: Particle size distribution of copper nanoparticles in 3 different oxygen-PAW samples based on percentage volume (a-c) and percentage intensity (d-f). 87

Figure 36: The averages of Z-average diameters of copper nanoparticles found in PAW for all three gases. The error bars are the standard deviation of the three Z-average diameters of each sample. 88

Figure 37: TEM images of the copper nanoparticles in an argon-PAW sample. Overall EDS analysis at the bottom. 90

Figure 38: TEM images of the copper nanoparticles in an argon-PAW sample. Overall EDS analysis at the bottom. 92

1 Introduction

The integration of metallic content into a liquid medium has been highly sought out in the advancement of inorganic chemical research. The reason is simple: once integrated, a metallic precursor is present in one form or another (soluble or insoluble). Such a precursor can then be used in several scientific, medical or agricultural applications for instance. Many methodologies have been established throughout the scientific realm in order to achieve consistent, efficient and cheap liquid metallic mixtures. However, the resolve is not always as simple as wet chemistry, whereby a metal solute is directly dissolved into a solvent, for that only produces a very meek matrix that can very well be inapplicable and even dangerous/fatal when surrounded by more complex matrices such as ones that are biological (human cells) or environmental (soil).[1]

The field of plasma sciences and technology introduces a synergistic method[2] of incorporating metals into liquid media. To elaborate, plasma technologies can induce the erosion of metallic electrodes into liquid media in the form of ions and nanoparticles.[3,4] In addition to these metals, highly oxidizing and reactive species such as reactive oxygen and nitrogen species (RONS) are another major by-product.[2,3] The combined efficiency of both the reactive species and metallic species is what makes plasma technology unique compared to the chemical/physical techniques of creating matrices rich in either component only. Furthermore, the sum of each by-products' separate effects has less worth compared to the combination of both.[2,5,6] Plasma technology allows for both these entities to coexist and spawn simultaneously in the same medium at a specific moment in time, by which its application to different scientific fields will be more advantageous and profitable due to the synergy created.[3] It is important to note that while RONS, metals and ultra-violet (UV)[2] rays are commonly the main additives of producing plasma activated liquids

(PALs), they are also less toxic than many others produced via wet chemical methods (such as the presence of lethal counter ions). Moreover, the only expense in producing these by-products is electrical energy from an outlet along with a power supply. This expense is non-costly and (in a relative perspective) infinitely replenishable, highlighting the economic and environmental advantages that can be presented through the use of plasma technology. Thus, this alludes to the primary motivations that were dedicated to this thesis project.

1.1 Objectives

In order to properly study the potential synergistic effect of PALs and the impact they have on their various applications, one must first identify and quantify the factors involved as well as investigate how to control them and whether or not their quantities affect each other in a positive or negative correlation. Unlike the erosion of high-voltage electrodes in in-liquid electrical discharges, the erosion caused by discharges created right above a liquid surface are rarely investigated.[3] Consequently, according to recent literature reviews, the characterisation of these PALs is the most challenging.[3] This thesis focuses particularly on characterizing the metallic content induced by electrode erosion in plasma activated water (PAW). The non-thermal plasma system is a pin-to-water surface configuration, whereby a copper electrode acting as the cathode is placed millimeters above a water surface and confined within a desired gaseous atmosphere (either air, oxygen or argon in the case of this thesis). Recent findings on cathode erosion caused by plasma discharges in contact with liquids, have proof that the resultant metallic content in the liquid is of two forms: ionic metals and nanoparticles.[3,4] Hence, the main goal of this thesis is to characterize both these metallic forms via various instrumental and newly developed techniques, in order to discern a ratio of dominance between them via comparisons of the detected ionic content to the total metallic content. By properly determining this ratio, insight will be given on the level of metallic contribution towards the synergy of PAW. In turn, this may unfold the role that metals play in the plasma medical field and disinfection applications in terms of cytotoxic and antimicrobial potency respectively.[7,8,9]

2 Literature Review

2.1 Preface

The erosion of electrodes in various plasma systems (thermal and non-thermal) have been extensively studied in previous years. As researchers we always strive to fill in the missing pieces that have been overlooked or subjected to extrapolation based on previous data. It so happens that not every non-thermal plasma system in contact with liquids has in fact been thoroughly investigated in terms of electrode erosion. As mentioned previously, one of those neglected systems is the pin-to-liquid surface discharge configuration.

In addition to electrode erosion, non-thermal plasma discharges in a gas/liquid setup produce highly oxidizing and reactive species along with UV photons.[2] Erosion is hypothesized to be caused by the acidic medium that is created during a corona discharge over a water surface, in conjunction with physical phenomena including sputtering, melting (local heating), evaporation and electrochemically-driven processes.[3] The acidity comes from the presence of nitrous and nitric acids, which are formed from hydroxyl and oxygen radical propagation reactions (when considering an oxygen- and/or nitrogen-containing gaseous atmosphere).[10,11] This means that both product entities of a plasma discharge over a water surface (RONS and metal) do interact with one another.

This section of the thesis gives background information, focusing on non-thermal plasmas in contact with liquids followed by the detailed comprehension of both its by-products. The main characteristics of copper are also introduced in order to understand its specific selection and priority over other metals. This will thereby transition to the possible applications that results from extensive research and finalizing with experimental background that aids the completion of this research at the present and in the possible future.

2.2 The Plasma State

2.2.1 Introduction to Plasma

To be able to understand how metal particles and ions can be integrated into aqueous media through plasma discharges in gas-liquid environments, it is crucial to first have a good fundamental understanding on what a plasma is, the general terms that are associated with it and how it interacts with liquid interfaces specifically.

Irving Langmuir introduced the term *plasma* in 1928 because the multicomponent highly interactable ionized gas reminded him of blood plasma. Plasma is sometimes referred to as the "fourth state of matter", whereby at high enough temperatures and energies, the gaseous state of a substance will ionize at certain ratios.[12] This means that a plasma medium consists of an ionized gas that includes neutral atoms/molecules as well as charged particles in the form of cations and electrons.[13] Due to these charged particles, plasma is an electrically conductive state, strongly responsive to electromagnetic fields and internally interactive.[12] One important aspect of plasma to keep in mind is that it should be in a state of local quasi-neutrality. Quasi-neutrality is in fact what distinguishes plasma from typical ionized gas.[13]

Plasmas constitute more than 99% of the visible universe and can occur naturally or artificially in laboratory and in industry.[12] In nature, plasma is perceived in Earth's ionosphere, through lighting, aurora borealis and solar wind. Plasmas are often described by their electron density and temperature, as well as the temperature of the heavy species (atoms, ions and molecules). In thermal plasmas, the gas temperature equals the electron temperature. In non-thermal plasmas, the electrons and heavy species are considered in equilibrium only amongst themselves, thus resulting in different temperatures for the electrons and heavy species. Most manmade non-thermal plasmas feature an electron temperature significantly higher than the heavy species temperature.[14,15] Typically, electron gas temperatures exceed 10,000 K while the heavy species temperature remains low, often close to room temperature. This unique set of conditions enables high chemical reactivity (i.e. often driven by the electron kinetics) and low heat transfer (mostly driven by the heavy species), thus enabling the plasma treatment of temperature-sensitive materials.[14]

With that being said, it is now quite evident that plasma offers advantageous features that are atypical in conventional chemical and biochemical systems. Firstly, plasmas can produce very high concentrations of energetic and chemically active species such as radicals, and second, non-thermal plasmas allow treatment at or near room temperature. Thus, certain chemical reactions, normally impossible in conventional chemistry at ambient temperatures, are stimulated in plasma. For example, the erosion of a metallic substance without the application of a voltage at room temperature is almost impossible with a very slow reaction rate, so the need to use corrosive substances or wet chemical leaching can lead to disastrous environmental and health side effects.[12]

2.2.2 Gas-Phase Plasma in Direct contact with a Liquid Electrode

Plasma-liquid systems can be classified based on the method of generation or configuration geometry (refer to Figure 1). The type of interaction with liquid defines the plasma properties of a plasma-liquid system. The classification includes the following categories and sub-categories:

1. Direct liquid phase plasma
2. Gas phase plasma producing reactivity in the liquid
    a. Without direct contact/electrical coupling with the liquid

    b. With direct contact/electrical coupling with the liquid (liquid electrode)
    c. At the plasma liquid interphase (surface discharges)
3. Multiphase plasma including
    a. Gas phase plasmas with dispersed liquid phase (aerosols)
    b. Gas phase plasmas dispersed in the gas phase (bubbles) in liquid[10]

Figure 1 shows general schematics of all experimental geometries. For the purposes of this thesis, the adapted configuration in Figure 1(C), depicting gas phase plasma with liquid electrode, is the most important since it prompts reactivity in liquids with pH variations and negligible thermal effects.[16] Although the discharge channel originates in the gas phase, it can propagate along the surface of the liquid, resembling branched discharge propagation patterns over solid surfaces.

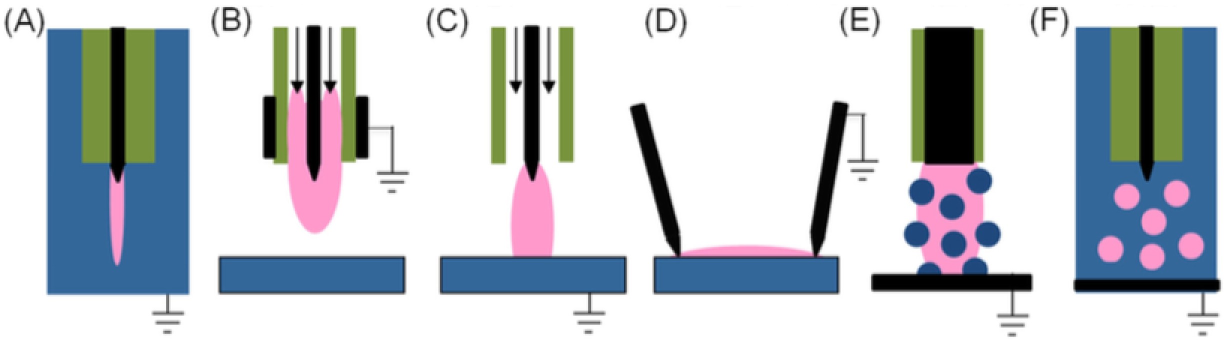

Figure 1: Schematic of different discharges used in plasma-liquid interactions: (A) direct discharge in liquid, (B)-(D) gas phase discharges and (E) and (F) multiphase discharges. In more detail: (B) plasma jet without direct contact with liquid, (C) gas phase plasma with liquid electrode, (D) surface discharge, (E) gas phase plasma with dispersed liquid phase (aerosols) and (F) discharges in bubbles. Blue = liquid, pink = plasma, green = dielectric, black = metal electrodes.[10]

With the exception of certain ionic liquids, plasmas generated in the presence of a distinct liquid and gas phase operate at atmospheric pressure or higher.[10] Figure 2 shows an example of a glow discharge in air with a water anode. These direct contact discharges have similarities with in-liquid glow discharge electrolysis where the metal anode is submerged in the liquid and the plasma is formed in a vapor layer. The vapor layer surrounds the electrode and is composed of gases produced by electrolysis, evaporation and the bombardment of electrons onto molecules. Note that liquid electrodes can stabilize the discharge as resistive electrodes do, which means that the contraction of the discharge at the electrode is prevented.[10]

Figure 2: DC driven air glow discharge in a pin-water geometry with self-organization at the surface of the water anode electrode.[10]

Common types of discharges that strongly interact with the liquid are diffuse glow, corona and spark discharges (assuming atmospheric gas pressure). Moreover, a large fraction of the discharge power is dissipated during liquid contact leading to fast rates of evaporation, especially when the liquid electrode is the cathode. Otherwise, when the liquid electrode is the anode, self-organization patterns are observed as seen in Figure 2.[16,17]

In the case where water is defined to be the liquid and air is defined to be the gas, certain distinctive reactive species are produced. High densities of hydroxyl, monoatomic oxygen, nitrogen monoxide and water radicals have been previously detected by some researchers.[10] Details about these species will later follow. Studies have reported that the resulting high electric field in the cathode sheath may be the reason behind instabilities at the plasma-liquid interface causing enhanced/efficient mass transport between the gas and the liquid phase, which explains how the remnants of reactive species are transferred to the liquid.[10,16]

When investigating the electrical breakdown in a metal (pin)-to-water electrode system with applied DC voltages, two important parameters that must be considered are the inter-electrode distance and the r/d ratio (where r is the electrode radius and d is the inter-electrode distance).[18] When r/d ≥ 1, breakdown is usually instigated by water surface instabilities, such as a bubbling surface or the formation of a Taylor cone, and the breakdown is a streamer-to-spark transition.[18] Figure 3 shows that the Taylor cone is fully developed before electrical breakdown occurs. Therefore, one can infer that the stability threshold of the water surface can also correspond to the experimentally observed breakdown voltage. This mentioned threshold is dependent on water surface tension and gravitational force.[18] If the liquid were to be ethanol, for example, (which has lower surface tension) an ethanol jet is formed from the Taylor cone (a liquid spraying phenomenon) before breakdown whereby the plasma channel begins.[18]

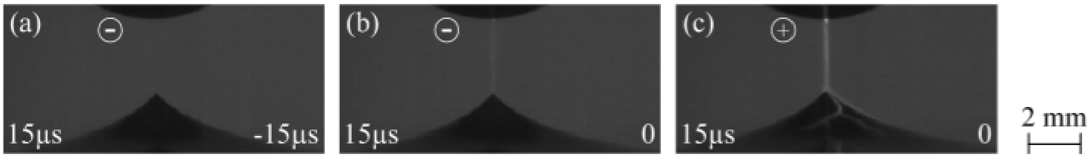

Figure 3: (a) Taylor cone before breakdown, (b) and (c) Taylor cone at breakdown for negative and positive polarity of the metal pin respectively. In the lower right corner of each image the time to or after spark formation is noted assuming t = 0 is the moment of spark formation. The lower left corner is the shutter opening time, and the metal electrode polarity is indicated in each image.[18]

Taylor cones have also been known to withstand subsequent corona discharges; however, stable corona discharges are observed near the metal pin electrode when r/d ≪ 1. This occurs right before electrical breakdown.[19] The corona induced ionic wind causes a depression in the water level beneath the pin. Furthermore, both negative and positive coronas are possible, yielding glow-to-spark and streamer-to-spark transitions, respectively.[19] When r/d = 1, the same transitions are observed, but no stable corona discharge is formed initially, meaning that the water surface is static when breakdown occurs (no ionic wind). The streamers formed in both ratios branch off from the main channel, indicating that there are different contact points with the water.[18]

The breakdown mechanism / glow-to-spark transition with a water anode is not comparable to that of a metal plate anode.[19] The difference is hypothesized to be due to the difference in conductivity of the anode. With a metallic plate, there is an obvious contraction of the anode spot. Whereas, the anode spot on a distilled water anode remains diffuse.[19] There is, though, a slight constriction of the glow in the bulk and near the pin cathode of the discharge gap, which in turn leads to the broadening of the spark near the water anode.[19] The broadened spark has a diameter that is almost equivalent to that of the anode spot of the glow. A bit of time is needed (~ 760 ns) for the broadened spark to constrict into a filament. This time is called the rise time of the spark peak and is heavily dependent on the liquid's conductivity.[19] It is more formally defined as the propagation time of the constriction of the glow from the pin metal cathode to the liquid anode. Some experiments have shown that an increase in water vapor in the discharge gap can have a stabilizing effect against constriction of the glow discharge.[19] Figure 4 shows the described glow-to-spark and streamer-to-spark transitions with a water anode and a metal pin cathode.

Whether a glow discharge or a streamer discharge is observed in this thesis's experimental setup is still under debate. Thus, for that reason it is important to understand the different plasma transitions as system energies increment.

2.2.3 Plasma Transitions: Pulsed Corona Discharges (PCDs) in Question

Pulsed corona discharges have asymmetric electrode configurations such as pin-to-plate and wire-to-cylinder electrodes on which high-voltage pulses with short rise time and duration are applied. When the breakdown voltage is achieved, a discharge is formed as follows: Electrons accelerate towards the positive electrode; upon their migration, they collide with neutral gas atoms/molecules thereby ionizing them and releasing more electrons in a cascade process. This phenomenon is called an electron avalanche and is self-amplifying.[20] When a critical local electron density is achieved after a series of electron cloud propagation, a thin cylindrical conductive glow/corona or streamer channel appears (depending on whether there is low or high voltage respectively)[20], which spreads towards the counter electrode. The characteristic visible light emission from the streamer is due to the recombination of electrons and cations at the edge of the discharge channel.[21,20,22]

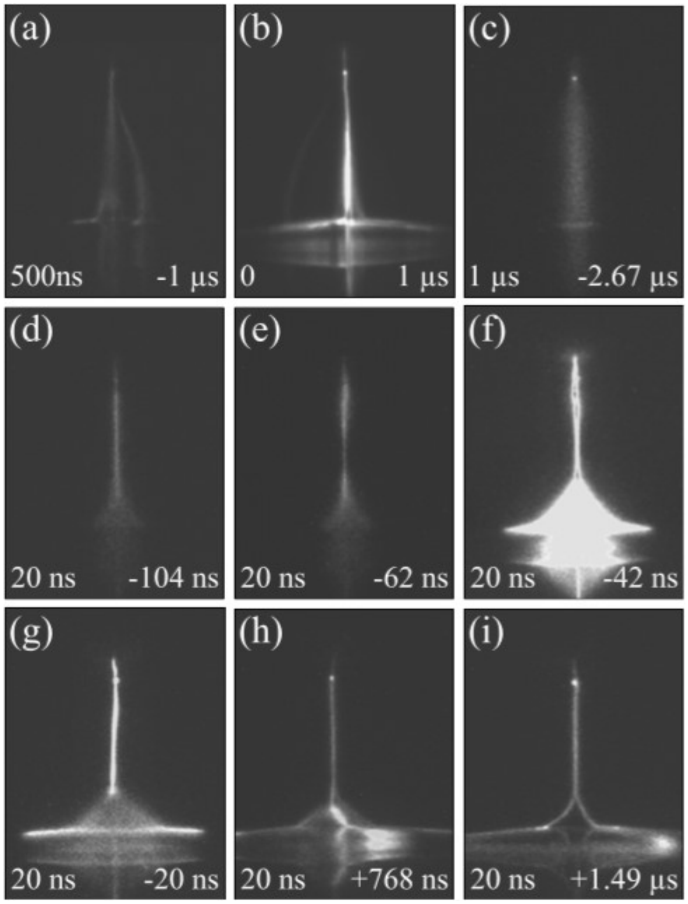

Figure 4: (a)-(b) streamer-to-spark transition, with water cathode (bottom) and pin anode electrodes (top) (c)-(i) glow-to-spark transition with water anode (bottom) and pin cathode electrodes (top). The lower right and left annotations of each image are representations of the same parameters as described in Figure 3. In all cases, the inter-electrode distance is 7 mm and the pin electrode radius is 0.5 cm.[19]

The formal plasma transition spectrum depicted in Figure 5 as a voltage-current characteristic graph goes as follows: starting from dark discharge to glow/corona to streamer (a phase transition between an abnormal glow and a non-thermal arc) to spark/arc, and the spectrum is dependent on electron density/current and voltage. Corona, normal glow and abnormal glow are different variants of non-thermal plasma, whereas the last arc region in Figure 5 (non-thermal and thermal arcs/sparks) is classified as thermal plasma.[8] With a constant supply of power (assuming a direct current (DC)) to the circuit, the plasma transition is expected to follow its common transitions starting from glow/corona to streamer to spark/arc once the breakdown voltage is achieved.[20,22] However, in the case of PCDs at atmospheric pressure, the voltage pulse decay halts the glow-to-streamer-to-spark transition at glow or streamer (non-equilibrium plasmas) depending on what is experimentally desired.[8,21] It is important to note that it takes thousands of collisions between electrons and heavy species before they equilibrate. At atmospheric pressure, the minimum time needed to reach equilibrium is on the nanosecond scale. Therefore, with nanosecond pulsed power supplies a high degree of non-equilibrium can be maintained (not allowing electrons enough time to transfer their energy to the heavy species).[22] So the resulting plasma can be quite intriguing, lying between glow and streamer regions of the plasma medium spectrum (this is also dependent on the frequency of the pulsed excitations).[22] As corona discharges do not essentially require a counter electrode, the discharges in our PCD setup are in fact not corona discharges but ones that are at the midpoint of glow-to-streamer region.[21] This is a plausible hypothesis, because the discharges observed form an electrical bridge between the cathode and the anode, which is not characteristic of a corona discharge.[20,8]

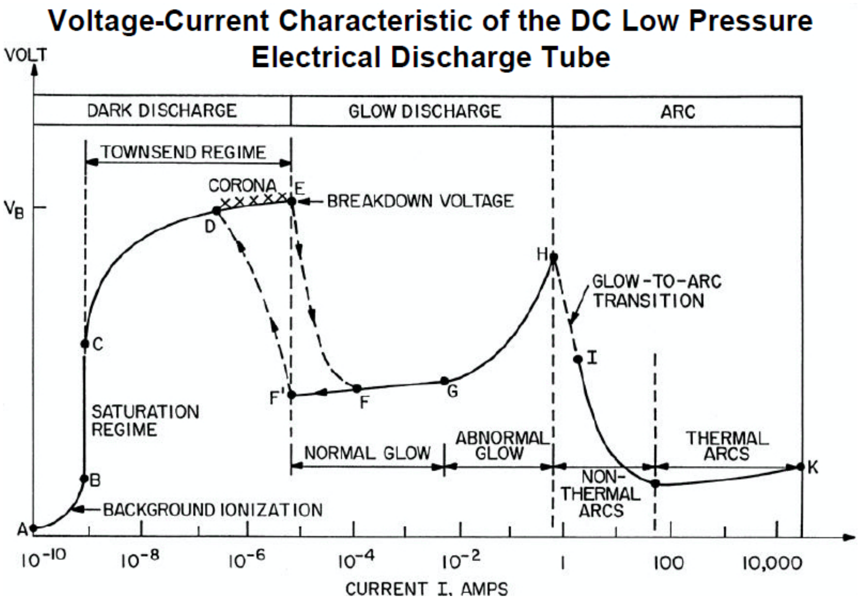

Figure 5: The voltage-current characteristic of a DC low pressure electrical discharge.[22]

2.3 The Major Consequences of a Pin-to-Water Surface Plasma Discharge

2.3.1 Plasma Chemistry: Formation of Oxidizing and Reactive Species

A reactive plasma environment comprises of many types of species that can be classified as either ions, electrons, radicals, neutrals or photons. The reason behind investigating this environment is because reactive species are the origin of new extraordinary properties demonstrated by the liquid component of the system. They are simply transferred to the liquid electrode through mass transfers during plasma activation. With water as the liquid electrode, these newfound properties can be easily used and examined when in contact with foreign media (outside the plasma system/setup like a bacteria or cell culture).[23] Once the water has become reactive from its contact with plasma, it is called plasma-activated water (PAW). In response, not only do the plasma generated ions and electrons activate the water, but water species can also transfer into the plasma and affect its properties.[23] Figure 6 displays a schematic of all the key species and chemical mechanisms involved in humid air plasma in contact with water.

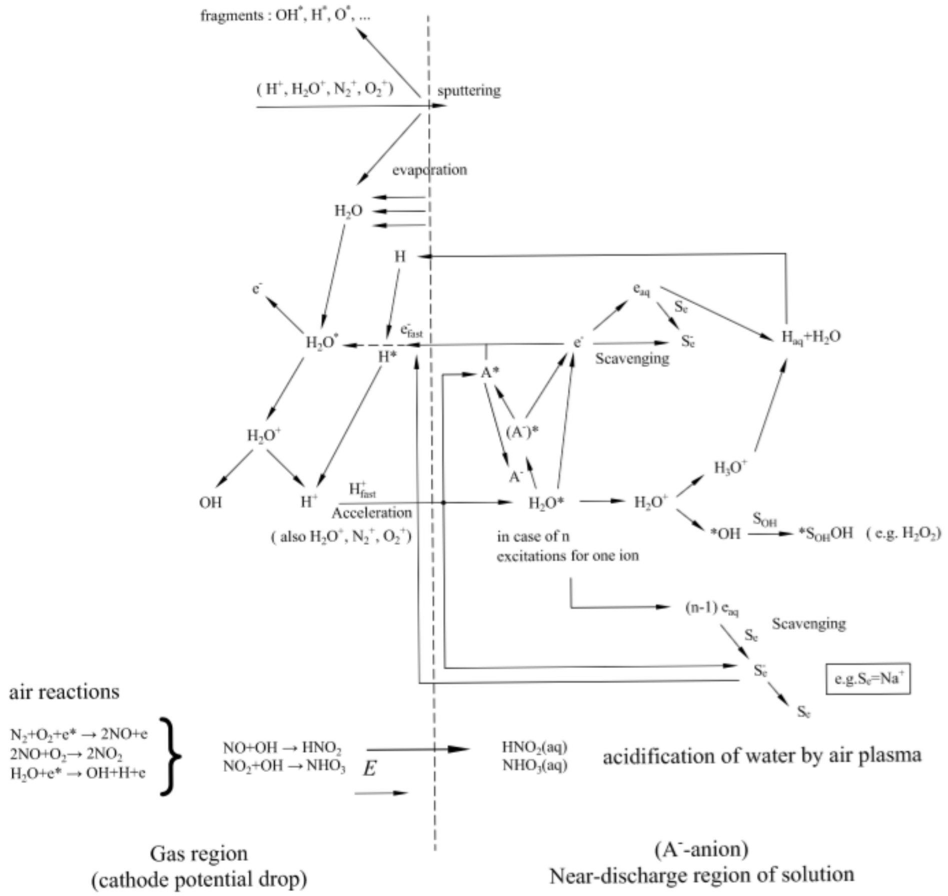

Figure 6: Overview of important reactions in air plasma-water anode interaction.[18]

However, from all these reactants shown in Figure 6, the most ubiquitous are: hydrogen radicals (H*), nitric oxide radicals (NO*), oxygen radicals (O*) and hydroxyl radicals (HO*).[24] These then perform radical propagation reactions with primary reactants/surrounding gas/liquid molecules to yield oxygen and nitrogen based secondary species such as noxes or nitrogen oxides (N_xO_x), hydrogen peroxide (H_2O_2), ozone (O_3), nitrous oxide (HNO_2), nitric oxide (HNO_3), peroxynitrous acid (ONO_2H)[11] and other nitrates.[24] Reactions can then propagate further from both primary and secondary reactants. To sum up, plasma-chemical reactions induced in aqueous solutions by electric discharges in air and in contact with the liquid can be classified into five categories:[24]

1. Oxidation reactions with reactive oxygen species (ROS) and reactive nitrogen species (RNS) that are strong oxidative agents → ozone, hydroxyl radical, peroxynitrite and hydrogen peroxide (produced by plasma).
2. Reduction reactions with strong reductive agents → H* and HO_2* (produced by plasma).
3. Acid-base reactions from the production of acidic species → nitrous and nitric acid.
4. Electrochemical reactions caused by electrons that are supplied by the plasma in the gas phase, reacting with the liquid phase as the anode → electrolysis of water.
5. Photochemical reactions initiated by UV radiation from the plasma → photocatalysis and photolysis of H_2O_2 and O_3.[24]

In a pure oxygen atmosphere, the same reactive species are present except any that contain nitrogen. As a result, the pH of the medium is higher as no nitrogen-based acids are present anymore.[2] The same can be said for a pure argon atmosphere, however, oxygen-based species will not seize to exist as they will originate from evaporated water molecules in contact with the plasma.[2]

A study performed by E. Corella Puertas *et al.*[3] has investigated the effect electrode metal erosion has on three major long-lived RONS: H_2O_2, NO_2^-, and NO_3^-, within four weeks post-discharge. In summary, it was shown that no hydrogen peroxide was detected in PAW after air plasma treatment and almost all nitrite ions were converted into nitrate ions. Furthermore, the use of different electrode materials did not significantly affect the RONS or the conductivity of PAW, insuring that no catalytic reactions are taking place.[3] This tells us that the metallic content does not play a major role in the degradation of RONS over time (with the exception of H_2O_2), meaning that their coexistence in PAW – and thereby the synergy created – is maintained for a long period of time after activation.

2.3.2 Cathode Electrode Erosion in Plasma Systems

One universal consequence of plasma production is the inevitable erosion of the electrodes. Since little is known to date of erosion in a non-thermal multiphase plasma system, it would be of an essence to have an idea of the mechanism of electrode erosion in thermal plasmas. Not only does it help us compare results, but it also aids us in formulating a reasonable hypothesis as to how erosion may occur in a multiphase plasma including an idea in regard to the electron emission process.

In gaseous arc discharges, electrodes play an important role in determining the electric field of the system as well as supplying secondary electrons to the discharge channel through a process called electric erosion.[25] Since cations will naturally migrate towards the cathode, they will eventually bombard its surface and cause sputtering. Sputtering will enhance surface asperities, which will result in channel discharge constriction: arcing.[26] Once arcing is achieved, hot spots are formed, and the resulting localized high temperatures will lead to metallic evaporation: electrode erosion.[25,26] These hot spots thus lead to the activation of either thermionic or thermo-field emission, which are the main origins of electrode erosion in thermal plasmas.[26] Because thermionic and thermo-field emission are an aftereffect of cationic bombardment and sputtering it can be hypothesized that erosion in non-thermal plasmas can indeed be caused by this bombardment. This latter hypothesis is based on an article written by Professor F. Llewellyn-Jones (Department of Physics, University College of Swansea),[25] where one may infer that though hot spots may be the primary cause of erosion, it is not the only one. In the case of thermal plasmas, however, the two main electron emission processes that can lead to erosion are thermionic and thermo-field emissions.

According to several sources, cathode erosion and its leading mechanisms in thermal plasmas are dependent on many different parameters. One major parameter is the electrode material.[25] If erosion is to be avoided/minimal, then refractory metals are used (such as tungsten (W) or hafnium (Hf)), meaning they are metals with high boiling points and resistive to corrosion/wear (also called hot cathodes). On the other hand, if erosion is desired, then logically a non-refractory metal is chosen (sometimes also referred to as a cold cathode). In any case, if the cathode were to experience a substantial or minimal amount of erosion in an arc plasma, then three main mechanisms are expressed: (1) microdroplet ejection as a result of ion pressure release during spot extinction, (2) microdroplet ejection due to thermo-capillary flows or simply (3) atomic rate vaporization of cathode material.[26]

Thermal plasma systems cannot purely exhibit field emissions. The high ion density near the cathode produces a high electric field which enhances thermionic emission. Thus, in general, thermal plasmas operate in a thermo-field mode that involves a high cathode tip temperature and high local electric field due to the presence of a high density of cations in the cathode layer, employing a thermionic-field (T-F) emission.[26] Whether thermo-field or purely thermionic emission is dominant depends on two distinct parameters: (1) cathode surface temperature and (2) electric field strength.[26] At high surface temperatures (> 3500 K → implying the use of hot cathodes) and moderate field strengths, thermionic emission is dominant because the thermal energy is sufficient to eject an electron from the metallic surface. When the surface temperature is lower (< 3000K), field effects become more prevalent.[26] Figure 7 shows a graphical representation of the relationship between surface temperature, field strength and current density, with a quantitative idea of how to achieve either efficient thermo-field or thermionic electron emission. It shows that the only way to achieve pure field emission is by having field strength approximately above 10^7 V.m^{-1} at lower temperatures. Notice that at intermediate temperatures and field strength it is always T-F emission and, hence, stating the generic scenario.

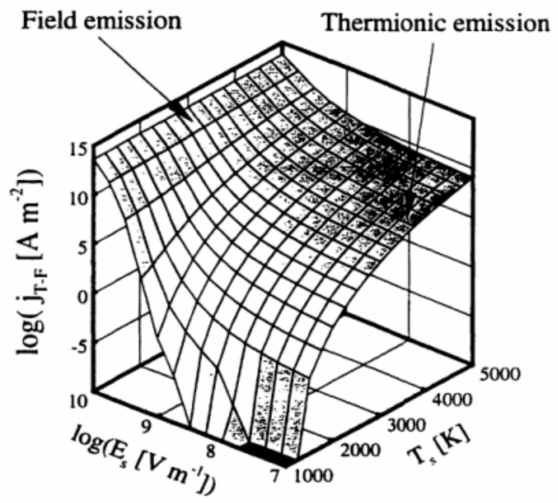

Figure 7: Current density produces from the surface of a metal electrode as a function of surface temperature and field strength.[26]

A final parameter worth mentioning is the work function of a metal (which is dependent on the metallic substance). The current density is always negatively correlated with the work function of the metal electrode, indicating that metals with low work functions yield higher current densities.[27,28] Therefore, periodic logic allows the inference that metals with high work functions will erode less making them potential candidates for refractory metals (since less current density implies less electron ejection and cation formation, meaning less loss of metal particles at the surface).[29] However, in reality, this theory is much more complex and dependent on other unmentioned physical parameters. Nevertheless, with the information given, one may surmise that when high current densities are desired in a plasma system that imposes high temperatures and thus thermionic emission, a metal alloy is used as the cathode, whereby the higher metal percentage is made out of a good refractory metal, such as tungsten (which has a high work function)[29], and the lower metal percentage constitutes of a metal with a low work function, such as thorium[29,27].

This way the refractory properties of the cathode are maintained while simultaneously emitting electrons efficiently in a high temperature medium.[28,27]

Discussing work functions is a great way of transitioning this section into the next, which involves the selection of metal in our non-thermal plasma system for this thesis. Moreover, good background knowledge on electron emission in thermal plasmas will definitely give us a notion of the causes behind the erosion mechanism involved in multiphase non-thermal plasmas.

2.4 Copper: An Excellent Cathode Candidate

In order to select a specific metal electrode to erode during plasma water treatment, we must first consider the benefits this metal has and its potential in contributing to the synergy of PAW. The chemical, biochemical and physical properties of copper are highlighted in this section, as well as its versatility and application in different research fields. This will justify the reasons behind selecting copper over other transition metals to be the cathode in our plasma setup.

2.4.1 The Physical and Chemical Properties of Copper

Copper is a ductile metal (with a relatively low melting point) that is easily degraded. Unlike tungsten, it is a non-refractory metal, however, their several surface planes have comparable work function values (ranging between ~4.5 eV to ~5 eV).[29] Though their work functions are very similar, one cannot deduce similar degradation patterns. As mentioned in the preceding section, erosion rates and mechanisms are dependent on many parameters not just work functions. Conversely, work functions may give an understanding towards the form of erosion (erosion in the form of nanoparticles or ions).[27] This notion will be discussed in more details in the results portion of this thesis, but as a gist, it is important to realise that a current density is also accompanied by a cation current density and work functions can give an idea of how easily cations can be formed from a metallic surface.[27,30] In thermal plasmas, the Schottky equation gives a definitive relation between work functions and electron current density for moderate field strengths and high cathode temperatures.[26] However, no parallel equation exists for non-thermal multiphase plasmas to date. With the work function of copper being relatively high, this then foreshadows that the dominant form of copper erosion into water will be as nanoparticles (physical degradation not chemical).[30,31]

In addition to being non-refractory, copper plays a huge role in chemical redox reactions, cellular growth, development and angiogenesis.[32] In aqueous biological media, copper ions are present in the cuprous (Cu^+) and cupric (Cu^{2+}) oxidized states allowing them to contribute as cofactors in redox reactions to cytochrome c oxidase and superoxide dismutase.[32] The coordination chemistry of copper is dependent on the oxidation state such that Cu^+ shows an affinity to sulfur donor ligands (such as cysteine and methionine) whereas Cu^{2+} has a preference for nitrogen and oxygen donors like histidine and aspartate respectively.[33,34] These preferences are solely based on quantum orbital theory and electron repulsion effects. The cuprous ion has a filled d^{10} electron configuration with no predilection on geometry based on ligand field stabilization energy, and so has variable chelating geometries allowing it to readily coordinately bond with sulfur, knowing that sulfur has the tendency of splitting its electron lone pairs to form complicated geometries.[33] On the other hand, cupric ions have a d^9 electron configuration and will favor a four to six coordination arrangement based on Jahn-Teller distortions.[33] Hence, with more constraints on geometry (including square planar, trigonal bipyramidal and axially distorted octahedron inclinations), cupric ions will favor coordinately bonding with elements that have more stable electron lone pairs like nitrogen and oxygen.[34] Therefore, these distinct fundamental properties of copper ions highlight their potential versatility in bioinorganic interactions. However, one major challenge with the consumption of copper is regulating the uptake and distribution in order to avoid unwanted biomolecular chelates that arise due to this versatility. With an affinity to oxygen and nitrogen, copper electrode erosion products thus have the ability to interact with RONS in PAW, giving leeway to various combinatorial effects that copper infused PAW can have in the medical field.

2.4.2 Overview of Copper and Microbial Biology

Studies from the last two decades have shown that copper plays a huge role in the growth and progression of malignancy. Tumor cells in humans and mice have exhibited increased levels of copper concentration. This was hypothesized to be due to the fact that copper also plays a critical role in angiogenesis, which is crucial for the growth, invasion and metastasis of tumor cells.[32] From *in vitro* experimentation, it was proven that copper acts as an important angiogenic effector by stimulating the propagation/migration of endothelial cells. Thus the concept of antiangiogenic therapy was invented, whereby organometallic copper chelates are produced to create indirect anticancer agents by firstly targeting angiogenesis.[35] To emphasize, copper in such a scenario would in fact act as a tumor selective vector or a tumor selective drug transporter. Another case that exhibited copper-based anticancer agents was with copper nanoparticles. Some studies observed that copper nanoparticles had potential in DNA degradation through the generation of singlet oxygen radicals.[35,36] In addition, they showed cytotoxic effects towards U937 and HeLa cells of human histiocytic lymphoma and human cervical cancer origins respectively by inducing apoptosis. The copper nanoparticles were said to act in an oxygen radical-mediated fashion without the need of external agents such as hydrogen peroxide or ascorbate.[35]

In terms of Cu-induced cytotoxicity, copper ions have potential cytotoxicity since they give capacity for the body to initiate oxidative damage[1] through the generation and propagation of hydroxyl radicals.[37] To clarify, when copper is consumed in doses that exceed physiological demands, an efficient homeostatic mechanism counteracts the intake to safely store or transport Cu ions in the body. Ceruloplasmin, albumin and transcuprein, for example, are major copper-transporting agents in circulating blood plasma.[37] Once Cu ions reach the liver, they are stored by hepatocytes, secreted into blood plasma or excreted in bile. Specifically, when stored in hepatocytes, a copper-metallothionein chelate is formed in the cytoplasm. Metallothionein is naturally selected by the body because of its high reactivity towards hydroxyl radicals and thus plays a protective role against copper induced cytotoxicity.[37] Hence, the natural need by the body to suppress the presence of free Cu ions hints at its potential cytotoxicity.

In addition to antitumor activity, copper ions alone can induce cellular/microbial toxicity. For example, it has been well established that all forms of copper (Cu(0), Cu(I), Cu(II)) are poisonous to algae and other heterotrophic bacteria in aquatic environments.[38] Many copper salts show selective antimicrobial activity such as copper sulfate towards poliovirus and cuprous salts towards *Escherichia coli.* Other counter ions and molecules have proven to reduce toxic effectiveness, such as phosphates ($Cu_3(PO_4)_2$ is insoluble in water and precipitates), hydrous metal oxides and humic acid chelates that reduce concentration uptake by microorganisms, thereby reducing antimicrobial effects. Furthermore, copper carbonate or colloidal copper can inactivate the bronchitis virus, and pure metallic copper can sterilize water. These antimicrobial properties of copper suggest its potential application in agricultural sterilization (effective and non-costly sterilization of food products that are distributed to communities around the world).[38,39,40]

With that being established, it is evident that copper is a very attractive metal to select after assessing its chemical and biochemical properties. Its role as an antitumor and antimicrobial agent compel researchers to break through the biochemical ambiguities and find a reasonable explanation to its formidable activity. With its incorporation into aqueous media via PAW due to its easy degradation, copper cytotoxicity (towards healthy and tumor cells) can be analyzed properly by considering the different parameters that accompany the method of integration; henceforth dictating its potential as an anticancer agent. Furthermore, the use of copper could be very advantageous seeing as the human body has already a natural efficient system to deal with copper metabolism (considering the presence of residual copper after a certain treatment), as previously discussed. Evidence provided by Xudong Su *et al.* has shown the antimicrobial properties of copper infused PAW by studying its effect on the inactivation rate of *Escherichia coli*.[41] They have proven an increase in inactivation rate by using copper infused PAW as a result of a synergistic action between cooper ions and the hydrogen peroxide generated by the plasma.[41] And even though their work involved a direct-in-liquid electrical discharge plasma (which is different to the plasma configuration in this thesis), it remains to be liable proof of the synergy of copper infused PAW induced in the presence of biological organisms.

2.5 Experimental Background

The methodologies in this thesis that are used to characterize the copper content of PAW are both standard (in the case of nanoparticles) and customised (in the case of ions). This section will give an overview on these methodologies along with background information to help understand their theoretical foundations.

2.5.1 Electrochemistry: Metal Ion Concentration Analysis via Anodic Stripping Voltammetry

Electrochemical methodologies have been highly appealing throughout this research investigation of metal content analysis in PAW. The reason is simply due to the very high sensitivity and low detection limits generally provided by electrochemical setups.[42,43] Initially, hypothesizing that copper content will be low, the fact that the ionic:nanoparticle ratio will additionally be very low itself proves that concentration levels may even reach down to fractional parts per billion. Thus, high instrumental sensitivity is necessary as well as selectivity. Even though PAW matrices are very reactive and complex, electrochemistry has the ability of overcoming this obstacle by using its high level of specificity and its ability to distinguish between different traces of metal and oxidizing species in liquid media.[43] To elaborate, when obtaining electrochemical data, almost every type of metal has distinguishable data acquisition patterns with rare/minimal peak overlapping or interference from other reactive species in the medium.[42] Moreover, detection is limited only to constituents in the aqueous phase, thereby ensuring that solid metal nanoparticles in PAW are secluded from the ionic metal analyte.[43] This segregation is crucial to produce an accurate ionic:nanoparticle ratio that is not overestimated. In addition to all the aforementioned, electrochemical instrumentation and tools are relatively cheaper than others and reusable for different types of experiments for a long period of time. All these factors motivate the use of electrochemical analyses over other methodologies. However, in many cases, the main challenge faced in electrochemistry is reproducibility ("many cases" does not imply all cases: for example, in polarography, the use of a mercury electrode can establish a surface state that is well defined and reproducible). This challenge is a consequence of its high sensitivity levels and its close theoretical affiliation with surface chemistry (since the surface of the electrodes cannot be 100% controlled under experimentation that is insufficiently funded, surface chemistry can be correlated to the levels of random errors in the experiment).[43] Reproducibility in this experimental setup is largely dependent on environmental, physical, chemical and geometric consistencies. The disruption of one of these factors can lead inaccurate data processing. This aspect will be discussed more elaborately in the results section.

In this research project, the chosen electrochemical methodology was Anodic Stripping Voltammetry (ASV). ASV usually involves the use of three electrodes: (1) the working electrode, which is itself relatively unreactive, provided that it does not oxidize or reduce in the desired working voltage range; furthermore, it is very important that the working electrode is polarizable (meaning the electrode does not respond with current when potential is changed, i.e. there is a large potential window in which the electrode is completely inactive (excluding the double-layer charging)).[44] Glassy carbon and several inert precious metals such as mercury and gold are excellent examples of commonly selected working electrodes. The reason it is called the working electrode is because its surface is the site where the analyte redox reaction takes place. (2) A reference electrode, which is a non-polarizable and reactive electrode where charge can alternate in and out of the electrode without changing its potential.[44] The reference electrode conducts an identical compartmentalized reaction in every electrochemical system such that the overall voltage production of this reaction is known and set/fixed in order for it to be compared to the main reaction (for example, in the case of a standard hydrogen reference electrode (SHE), that voltage is set at 0 V).[44] When potentials of different electrochemical systems are compared, they must have the same reference electrode, otherwise the difference in voltage between both references must be added or subtracted to one or the other if comparisons are to continue consistently. One of the most common reference electrodes used is the silver/silver chloride electrode, consisting of a silver wire suspended in an aqueous solution of potassium chloride and silver chloride (AgCl).[45] Once a negative charge is removed from the electrode, the oxidation of the silver metal takes place to produce silver ions. Contrariwise, when a negative charge is applied to the electrode, the silver ions from the AgCl concentrate will reduce to silver metal. The voltage stability of this electrode is due to the very low solubility constant of AgCl and the fact that the concentration of the chloride ions in the electrode electrolyte is constant and large, thus not enabling high levels of Ag oxidation to Ag^+.[44] Through constant comparisons to a stable reference electrode, the voltage of the working electrode can be sustained at the desired absolute potential. (3) Voltage shifts are usually the cause of instabilities in an electrochemical system. In order to avoid voltage shifts at the reference electrode, the amount of current passing through it must be limited.[45] Hence, comes the function of the counter electrode, whereby it is used to carry most of the current from the working electrode.[45] The counter electrode is an inert polarizable material with a larger surface area than the working electrode (in order not to limit the current) and does not necessarily take part in the analyte's redox reaction.[44] Examples of common counter electrodes are graphite and platinum electrodes.

In short, ASV can be divided into two fundamental steps: (1) the analyte(s) is(are) reduced and electrodeposited on the working electrode's surface and (2) the analyte(s) is(are) then oxidized or electrolyzed back into the electrolyte solution.[46] For the deposition step to take place for a specific analyte, the reduction potential of that analyte must be applied at the working electrode for an optimized amount of time (reduction voltage estimates can be found through stored literature data).[46] Once a reduction voltage is applied to the system, the (metal) analyte diffuses to the active surface of the working electrode. The migration rate is dependent on many parameters including analyte concentration, diffusion properties of the electrolyte solution, electromigration, convection and surface area of the working electrode's active surface.[46] Conversely, to strip the analyte from the active surface, the voltage is systematically reversed back to induce oxidation and propelling analyte ions back into the electrolyte.[46] Several different analytes may simultaneously deposit and strip off the active surface (depending on the potential ranges and sweeps applied),[42] but only the faradaic current produced from oxidation is recorded at the peak oxidation voltage of each analytical species.[46] The final voltammogram produced is a result of scanning the voltage towards positive potential and then measuring the amount of current flowing through the working electrode during the stripping step.[44] The electrons flowing through the recording instrument at the moment of complete oxidation/stripping yield a distinctive peak on the voltammogram plot of current vs. applied voltage.[44] The current value of this peak is known as the stripping current and is directly proportional to its corresponding analyte concentration in the bulk solution.[43]

2.5.1.1 The Levich and Cottrell Equations

Plating efficiency is optimized by adjusting many variables. For an individual ionic metal species in solution (M^{n+}) being reduced at the active surface, the current at a specific moment in time can be expressed via the Levich equation depicted by equation (1) assuming a rotating disk electrode:[46]

$$i(t)_{dep} = 0.62nFAD^{2/3}\omega^{1/2}\mu^{-1/6}C(t) \tag{1}$$

Where $i(t)_{dep}$ is the measured deposition current with respect to time, n is the charge of the metal cation, F is the Faraday constant, A is the working electrode's active surface area (in m^2), D is the diffusion coefficient of the M^{n+} (in m^2/s), ω is the convection rate (stirring rate of the system or rotation rate of the working electrode) (in s^{-1}), μ is the kinematic viscosity of the solution (in P) and C(t) is the bulk cation concentration of M^{n+} (in M).

However, when the measured current from deposition is completely diffusion controlled (mass-transport controlled) with no stirring of the electrolyte and no alterations in viscosity at a constant electrode potential, then it is more accurately described by the Cottrell equation as follows:[43]

$$i_{dep} = \frac{nFA\sqrt{D}C}{\sqrt{t\pi}} \tag{2}$$

On the other hand, the stripping current is slightly more complicated because it is analyte specific. Fortunately, DeVries *et al.*[46,47] and Osteryoung *et al.*[48] have deduced a generic approximation for the stripping current peak of deposited thin metal films with thicknesses ranging between ~ 2 to ~10,000 Å.[48] Their research was based on mercury thin-film electrodes and yielded the following expressions with a linear ramping of the potential:[46,48]

$$i_p = (1.1157E6)n^2ACLv. \tag{3}$$

Where i_p is the stripping current peak, L is the deposited film thickness and v is the scanning rate. Equation (3) can also be rewritten as:

$$i_p = 11.6n^2vFACL. \tag{4}$$

The reason why an approximation of only the peak current was formulated is probably due to the presence of non-faradaic currents. These non-faradaic currents make a continuous mathematical relation of stripping current with respect to time impossible (notice that the stripping peak current is independent of time).[47] Furthermore, the film thickness is considered to be constant for every ASV system, since the approximation applies to a wide film thickness range and the reproducibility of identical films for every single ASV run is very difficult and almost even impossible to achieve. Hence, thicker deposited films are assumed to exhibit thin-film behaviour.[46]

This section highlighted and proved the direct proportionality demonstrated between current (whether deposited or stripped) and bulk analyte concentration, which dictates the purpose behind utilizing ASV as an optimal technique for determining copper ion concentrations in PAW.

2.5.2 Particle Size Analysis: Metal Nanoparticle Characterization and Control

As electrochemical techniques are used to analyse the ionic form of the copper content in PAW, there must be a means to characterize the solid nanoparticle form too. Studying the nanoparticles and the methods by which they can be controlled in size and shape is very beneficial in the field of nanomaterial design.[4] This thesis focuses less on the control aspect and more on the characterization portion of eroded metal nanoparticles, because the characterization step is the first step towards understanding how and what nanoparticle properties can be controlled. Nevertheless, the future/continued work section will mention some reviews of nanomaterial synthesis as a result of plasma-liquid interactions and how certain multiphase plasma parameters have the potential to alter or control nanoparticle size distributions.

The main instrumental method used in this research to characterize eroded copper nanoparticles is particle size analysis (PSA). Particle size determination of the nanoparticles is important because it is a valued indicator of general performance and quality (in terms of applications of nanomaterials).[4] PSA can also be used to monitor particle size growth due to agglomeration, granulation or crystallization over a long period of time.[49] Although many instrumentational techniques use spherical approximations to average particle size distributions using diameter values only, PSA uses a light scattering device that allows the averaging of several different dimensions simultaneously. This is advantageous in the analysis of particulates with very high aspect ratios (such as needles and fibers).[49] The cylindrical beam of light that engulfs a pool of particles flowing randomly in a suspension will scatter or diffract light and produce a distribution based on sizes in an increasing order of dimensions.[49] Particle size described by multiple values can only be achieved by automated image analysis or microscopy. These multiple values may include long diameters, short diameters, equivalent spherical diameter, projected area and perimeter.[49] Commonly, when a single dimensional value is graphically recorded, the metric value is listed on the abscissa and a percentage is shown on the ordinate.

When dynamic light scattering (DLS) is employed mean values from an intensity distribution (called Z-averages) are outputted with a polydispersity index (PDI) to describe the variability levels or distribution width.[50] Intensity values can then be converted into volume percentages so that the results are recorded on a volume basis. An output of the volume mean is usually presented by the system, however, median values can also be considered or even preferred depending on how symmetric the size distribution is. Because volume distributions are presented in percentage, the volume mean calculated is in fact the geometric mean.[49] This is done by the instrument in order to normalize differently ranged values of sizes, meaning that if a percentage change occurs for one size it will have the same uniform effect on the geometric volume mean without skewing the distribution. Normalization is crucial in such a scenario because it eliminates the dependence of frequency on the volume mean and amplifies the significance of overall uniform contribution from every dimension recorded to the volume of a nanoparticle. This in turn implicates the formation of an output distribution that is most of the time Gaussian and not skewed. The general equation used to calculate the all types of means using our instrument is depicted by equation (5)[49,51]:

$$\overline{D}_{pq}^{(p-q)} = \frac{\sum_{i=1}^{n} D_i^p}{\sum_{i=1}^{n} D_i^q} \tag{5}$$

Where $\overline{D}$ is the overall geometric mean (in percent), D_i is the geometric diameter mean of particle i and n is the total number particles. For volume means, equation (5) is expressed as[49,51]:

$$\overline{D}_{43}^{(4-3)} = \frac{\sum_{i=1}^{n} D_i^4 v_i}{\sum_{i=1}^{n} D_i^3 v_i} \tag{6}$$

Here D_i is the geometric mean of diameter sizes of particle i multiplied by the percentage of i particles v_i in a beam of light. The geometric mean here ensures that the overall contribution of each diameter size is of the same equivalence to the overall volume mean. The theory behind the mathematical exponent deductions is irrelevant to this research.

Hence, whether a volume distribution percentage or intensity percentage is shown, the resulted/converted mean volume tells us what the majority of diameters occupying a cylindrical beam of light volume is. The remainder percentage is distributed equivalently along the Gaussian distribution as errors or standard deviations from the mean. Even though spherical assumptions are indeed made in these calculations, several diameters can be considered for one single particle since light can diffract/scatter at different angles with different light intensities on an amorphous nanoparticle. Numerous runs and data collection compensate the spherical approximations by giving light the opportunity to scatter/diffract from different faces of the same nanoparticle.

2.5.2.1 Laser Diffraction Technique: Origins behind Volume Distributions

The main concept behind laser diffraction technique (LDT) is that particles will scatter light at different angles depending on the particle's size/diameter.[52] Large particles will diffract a monochromatic source of light intensely at more acute angles, and small particles will diffract light weakly at wider angles.[52] Even though LDT is not directly used in this research's experimentation section, it nevertheless explains the theory behind converting DLS intensity results to volume distributions.

Initially, the Fraunhofer Approximation was used in older laser diffraction instruments to simplify calculations. In this approximation, particles were assumed to be spherical and opaque, to scatter light equivalently at wide angles as narrow angles and to interrelate with light in a different manner than the medium.[52] Unfortunately, The Fraunhofer Approximation is inadequate for the analysis of particles at the nanoscale with a detection limit of 20 microns.[52] Thus, the Mie scattering theory was developed to overcome this limitation with a wider range of opacity.[52] This theory was based on Maxwell's electromagnetic equations for scattering from spheres and even accounts for minimal levels of particle transparency i.e. light that refracts through the particle a.k.a secondary scattering.[52] The assumptions made in the Mie theory are that the particles being analyzed are spherical, the particle ensemble is homogeneous and the refractive indices of the particles and medium are known.[52] Figure 8 shows a comparison between the Fraunhofer Approximation and the Mie theory.

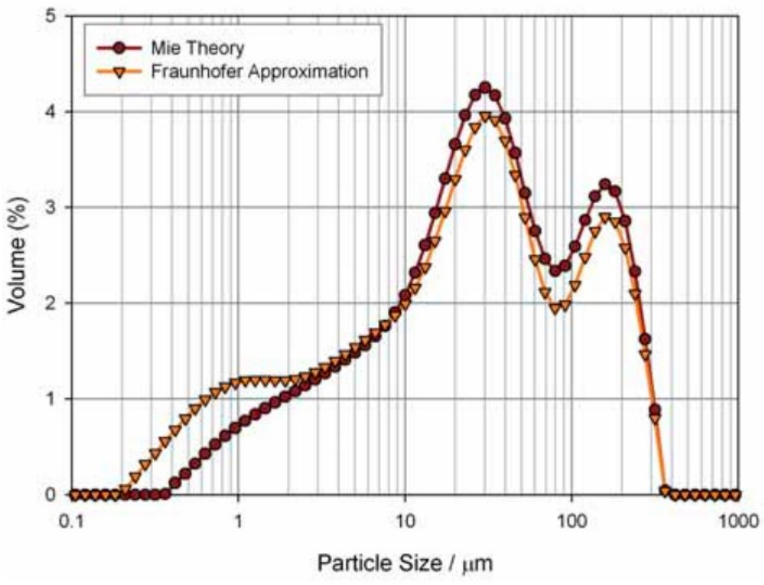

Figure 8: Graphical comparison of the Fraunhofer Approximation and the Mie theory based on the analysis of a single identical sample. (This image was extracted from malvernpanalytical.com)

Differences are pronounced below 10 microns, with the Fraunhofer Approximation having an unacceptable magnitude of error that leads to the over-reporting of small particles. The overestimation is mainly caused by the fact that the Fraunhofer Approximation does not account for light refraction within the particle phase.[52]

The Mie theory explains the premise behind converting DLS intensity values into volume distributions given the refractive indices and absorption coefficients of the particles. However, DLS experimentation is implemented solely to produce raw data in this research.

2.5.2.2 Dynamic Light Scattering: Intensity Distributions

Analogous to volume distributions, intensity distributions simply depict the pool of diameters contributing to the overall intensity of scattered light in a system. In turn, the percentage mean intensity value shows the majority value of diameters contributing to the overall intensity.

DLS allows particle size to be determined by measuring random changes in the intensity of light scattered from a suspension of particles.[53] The Brownian motion of nanoparticles in suspension is measured to calculate particle size.[53] Figure 9 shows a general instrumental schematic layout of the DLS technique.

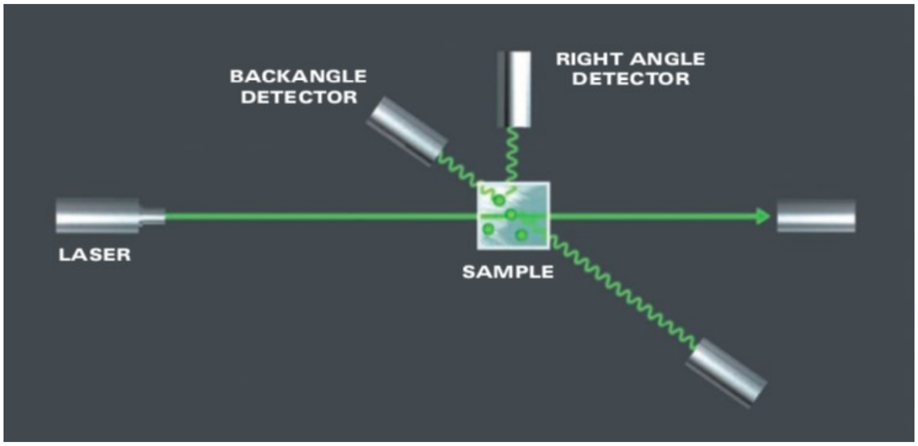

Figure 9: A general instrumental layout of the DLS technique. The laser is used as the light source to illuminate the sample cell. Scattered light is detected by one of two detectors: either a right angle detector or a 173 degree back angle detector.[42]

The acquired optical signal show light scattering fluctuations due to Brownian motion of nanoparticles. These fluctuations can be interpreted using an autocorrelation function that is dependent on delay time.[53] Figure 10 shows how the autocorrelation function can be used to convert light scattering fluctuations as a function of delay time. The bottom graph of Figure 10 is an example of a case where all the particles in the sample have the same size/diameter.[53] Samples that have particles with various sizes will simply group similar light scattering fluctuations together by the instrument.

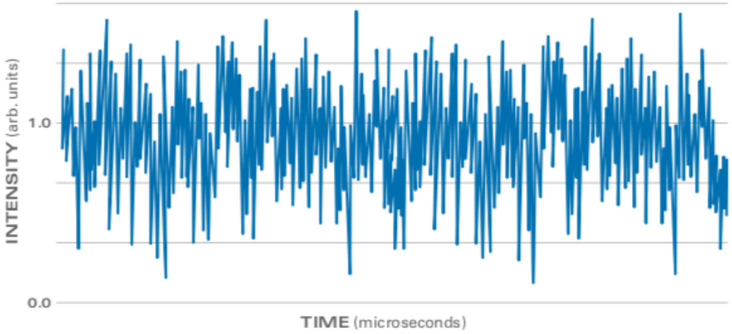

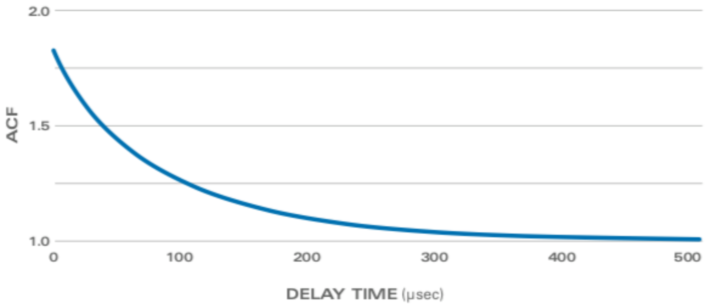

Figure 10: Top graph shows light scattering fluctuations and bottom graph shows how the autocorrelation function converts the top graph as a function of delay time.[53]

The exponential decay exhibited by the autocorrelation function is described by the following equation (incorporating baseline subtraction):[53]

$$C = e^{-2\Gamma\tau} \tag{7}$$

Where C is the autocorrelation function, τ is the delay time and Γ is a constant derived by experimental data via curve fitting. Then, the translational diffusion coefficient (D_t) of the particles is obtained from the following relation, $\Gamma = D_t q^2$,[53] where q is the scattering vector calculated by the instrument from:[53] $q = (4\pi n/\lambda)\sin(\theta/2)$ when given the refractive index n, the wavelength of the laser source λ, and choosing a scattering angle detector θ. With the determination of D_t, finally, the Stokes-Einstein equation solves for the particle diameter using the following equation (8):[53]

$$D_h = \frac{k_B T}{3\pi\eta D_t} \tag{8}$$

Where D_h is the hydrodynamic diameter, k_B is the Boltzmann constant, T is the temperature and η is dynamic viscosity of the liquid (for low-concentration samples) or of the suspension itself (for high concentration samples).

This preceding theoretical explanation demonstrates how particle sizes are calculated via DLS technique. Intensity values are then also recorded in relation to diameter calculations to yield percentage intensity distributions accompanied by specific PDI values to describe distribution widths. Using refractive index values and absorption coefficients of the particles and solvent will allow system automated conversions to volume distributions using the Mie theory applied to LDT.

3 Experimental Methods

3.1 Preface

This chapter will explore the direct experimental methodologies that were implicated for PAW sample preparation and analysis. The pin-to-water nonthermal plasma setup was used for sample preparation and control. The conditions of the PAW samples created are completely dependent on the conditions of the plasma setup.[4] Thus, in order to yield samples that are theoretically identical in chemical constituents, the conditions of the plasma setup must be consistent and monitored at all times.

The copper content analysis of the PAW samples was carried out via ASV and PSA. Other instrumental methods (such as transmission electron microscopy (TEM), scanning electron microscopy (SEM) and inductively coupled plasma – optical emission spectroscopy (ICP-OES)) were also used for characterisation, however, they will not be presented in details as they follow standard operating procedures.

3.2 The Pin-to-Water Nonthermal Plasma Setup: PAW Sample Preparation

3.2.1 Overall Experimental Configuration

As alluded, any minor alterations to the plasma system can lead to inconsistencies when measuring copper concentration of different PAW samples. For that reason, every detail mentioned in this section is crucial to the outcome of the investigation. Figure 11 shows a general semi-labeled schematic of the setup. The zoomed-in section highlights the phenomena that occur at the gas-liquid interface within the plasma reactor.

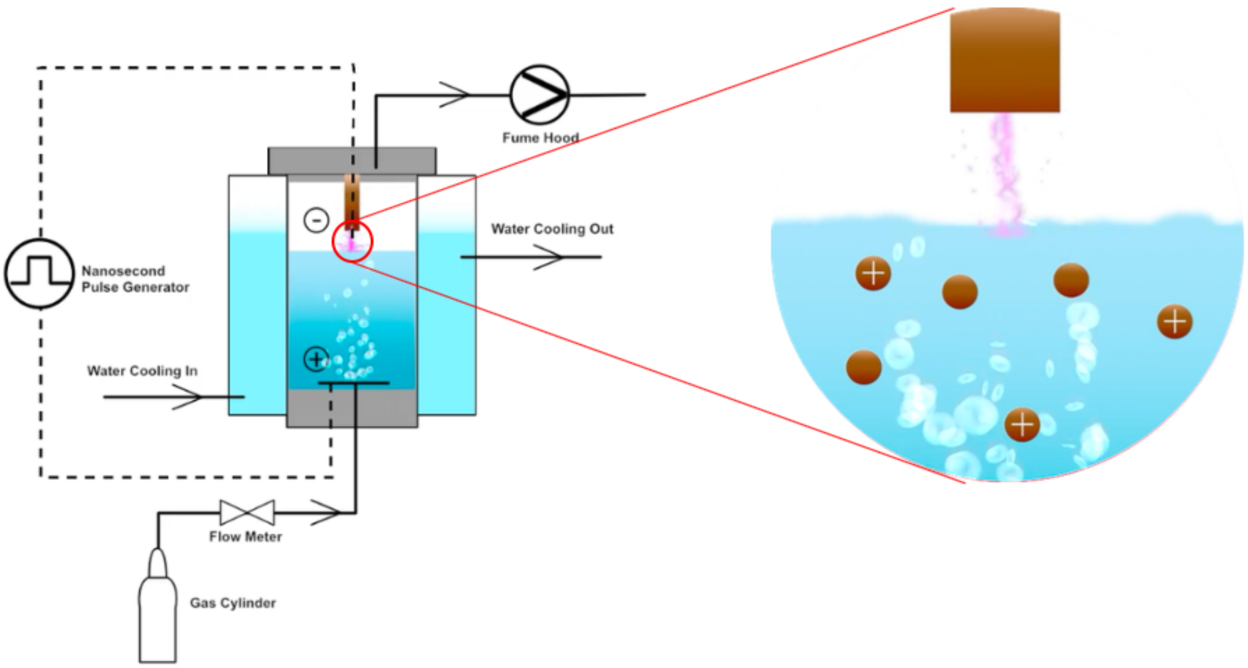

Figure 11: Schematic of the pin-to-water non-thermal plasma system/reactor. The copper pin cathode is designated by the negative polarity and the submerged stainless-steel anode sparger is designated by the positive polarity. The white circles represent the gas bubbles erupting from the sparger and supplied by the gas cylinder. The zoomed-in portion of the figure shows the gas-liquid interface where a violet plasma discharge originates from the cathode and branches on the water surface. The orange-brown circles represent the copper content transferred into the water via mass transfer. Those with positive signs denote cations and those with no signs denote nanoparticles. It is important to note that this entire schematic is not to scale and the bubble density as well as the ion:nanoparticle ratio are not accurate either.

3.2.2 Plasma Reactor Vessel Setup

The reactor seen in Figure 11 is compartmentalized from the sides using a cooling borosilicate glass jacket (*JRV Scientific Glass Montreal*, inner diameter 19.4 mm, height 83.5 mm) with a circulating water bath (similar to a condenser used in a distillation setup) (*Marshall Scientific*, *Thermo Neslab RTE 10 Circulating Chiller)* and from the top and bottom using custom-made electrically insulative Teflon lids that support each respective electrode. The top lid is manufactured with a narrow slit that allows only wires with diameters at the millimeter scale to penetrate. This slit is sealed off using a rubber septum where the wire that is meant to be the pin cathode has been previously threaded through. The bottom lid holds the 316L stainless-steel anode sparger (Custom-made with one single hole, 8.05 mm total diameter, unknown diameter hole size) that has been soldered to another piece of stainless-steel. The anode sparger will always be completely immersed under the column of water that is deemed to be activated by the plasma discharge in order for it to bubble a chosen gas into the atmosphere surrounded by the cathode pin. Since this is a single-hole sparger, the gas is bubbled through one bubble at a time with a flow rate determined by the gas-flow regulator. Not only does gas bubbling allow the injection of a chosen gas into the reactor but it also homogenizes the PAW solutions.

The double-wall cooling jacket allows the circulation of a water-glycerol solution through the annular space of 19.4 mm and maintains the temperature of the reactor at ~ 20 ºC (static room temperature). The glycerol solution is pumped in from the bottom end of the condenser, cools down the system to the set temperature and then pumps the heated water out the vessel from the top end back to the water bath to be cooled down and recycled. This water flow direction is crucial because it prevents/expels bubble accumulation at the mid-annular space of the vessel. Bubbles can form in the annular space due to water evaporation caused by excessive heating from the plasma discharges. If the flow was reversed, bubble cavities or “dead zones” will be formed and trapped within the annular space producing hot spots that can melt the reactor. Furthermore, in addition to preventing fouling/corrosion, glycerol aids in preventing water evaporation by raising the boiling point of water. This in turn minimises the probability of bubble cavity formation.

The copper pin cathode is prepared by cutting a 10 cm wire off a 99.99+ % fine copper wire bundle (*Goodfellow*) that has a diameter of 0.25 mm. In order to create a pin tip surface that is more or less flat, a wire cutter that has a flush cut profile (*McMaster-Carr)* is used. The copper cathode is then inserted into the top Teflon lid with the flat ended tip mounted ~ 2 mm above the water surface. The other end of the cathode is connected to the negative end of the nanosecond pulser via wire-to-wire soldering (the positive end of the nanosecond pulser is connected to the anode). The water placed under the cathode is reverse osmosis (RO) water that has a volume of 7.5 ml and a resistivity of 1.2 MΩ.cm. Because the resistivity was considered relatively too low, the RO water was further filtered via vacuum filtration through 0.22 μm filter paper (*Merk Millipore Type GV*) to achieve higher water purity. The anode sparger submerged under the column of water supplies either air, oxygen or argon (*Praxair*, 99.993% purity) to the system at a 10 ml/min flow rate at atmospheric pressure. The sparger is able to supply gasses to the reactor because the bottom lid to which it is attached to is connected to the flow rate regulator through a gas line. The regulator itself is connected to the gas cylinder through another gas line. In the case of oxygen and argon, the chosen gas must flow through the confined chamber for 3 min prior to any experiment to make sure the reactor chamber is sufficiently purged. Even though the gas cylinder delivery pressure is regulated at 5 psi, the flow meter controls how much gas enters the reactor. The gas leaving the reactor exits through a gas line that is connected to the top lid of the reactor leading to the fume hood.

Figure 12 shows an overall live picture of the plasma reactor vessel with all the components mentioned above.

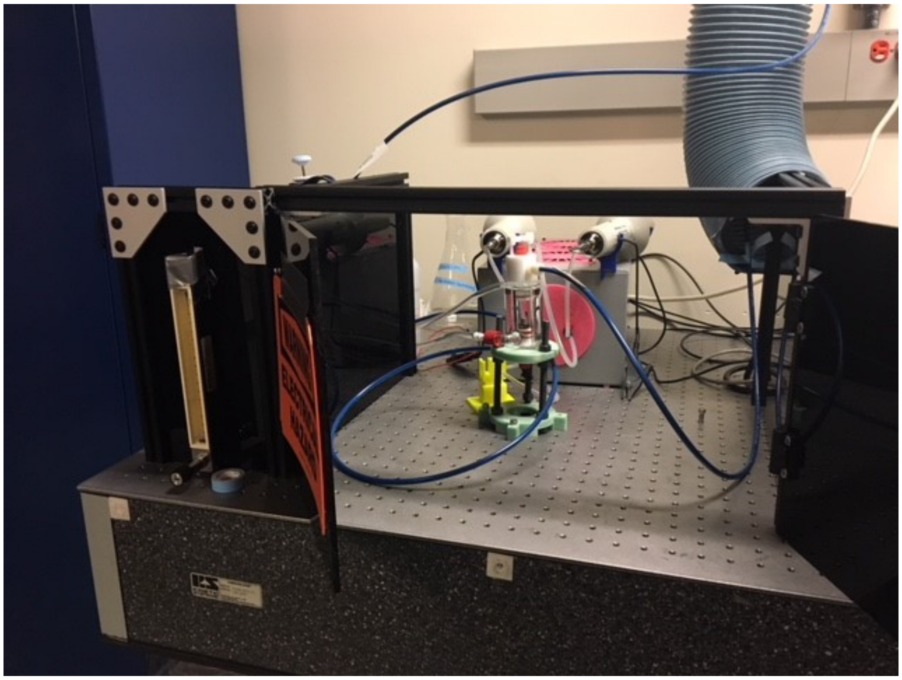

Figure 12: Overall picture of plasma reactor vessel. The column on the far left is the flow meter and the electrical box behind the reaction vessel is the nanosecond pulser with two high voltage probes seated on the top of the box. The elephant trunk (upper right corner) is connected to the fume hood exhaust; this is what the gas line containing exiting gas leads into.

3.2.3 Electrical Mechanism and Conditions

Once the reactor is set and optimized the plasma discharge can be initiated. A diode opening switch generator powers the electrodes, producing two simultaneous pulses. The negative pulse powering the pin electrode; the positive pulse powering the sparger. Nanosecond pulses are produced at a frequency of 3 kHz and a total voltage drop of 12 kV. Two passive high-voltage probes (*Tektronix P6015A*) measure the discharge voltage signals, while a current transformer probe (*Pearson 6585*) measures the current. A digital oscilloscope (*Pico Technology, PicoScope 2207B*) with two channels records the electrical signals simultaneously (meaning only two inputs are recorded simultaneously). Voltage pulses were recorded first to confirm their synchronicity (an estimated 12 ns delay between both inputs) and equal peak amplitude. Then the negative voltage pulse and current were recorded. This latter data acquisition is characteristic and important to keep track of while performing sample preparation (constant variables like temperature). Any distinct changes in this electrical profile can alter copper content results. Figure 13 shows an example of this unique voltage and current profile in the case of a discharge over water with a copper pin electrode in air given the conditions stated above. The yielding full width at half maximum (FWHM) is ~ 40 ns with a peak current of ~ 4 A.

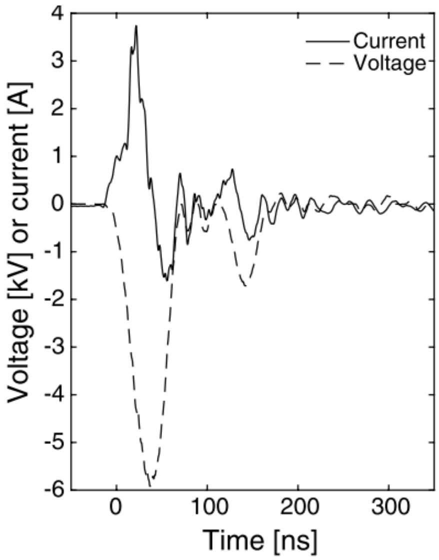

Figure 13: The voltage and current profile of a plasma discharge over water using a copper pin cathode in air. The electrical conditions include nanosecond pulses at 3 kHz and a total peak-to-peak voltage drop of 12 kV.

Figure 14 shows the electrical setup (with all the electrical components previously mentioned) connected to the plasma reactor in Figure 12 through the nanosecond pulser. The power supplies seen in Figure 14 with voltage ranges between 0 – 20 V and 0 – 600 V apply voltages of 18 V and 580 V respectively to the plasma system. However, they are not very relevant because their average power (which is relatively low at 61 W) is converted or manipulated by the nanosecond pulser. In simple terms, the pulser accumulates all the applied voltage into one single pulse with a pulse width on the nanosecond scale. In order to conserve 61 W of average power, the voltage peak of each pulse will rise up to the order of 10^3 V or 1 kV (or possibly higher). This means that the instantaneous power at the peak of each pulse can reach the order of 10^6 W or 1 MW. Therefore, the average power of the system does not represent the actual power being provided to the plasma reactor. In addition to thermodynamic optimization (as mentioned in the literature review), the nanosecond pulser is also economically advantageous because it has the ability to convert low average powers of cheap power supplies to the peak megawatt level.

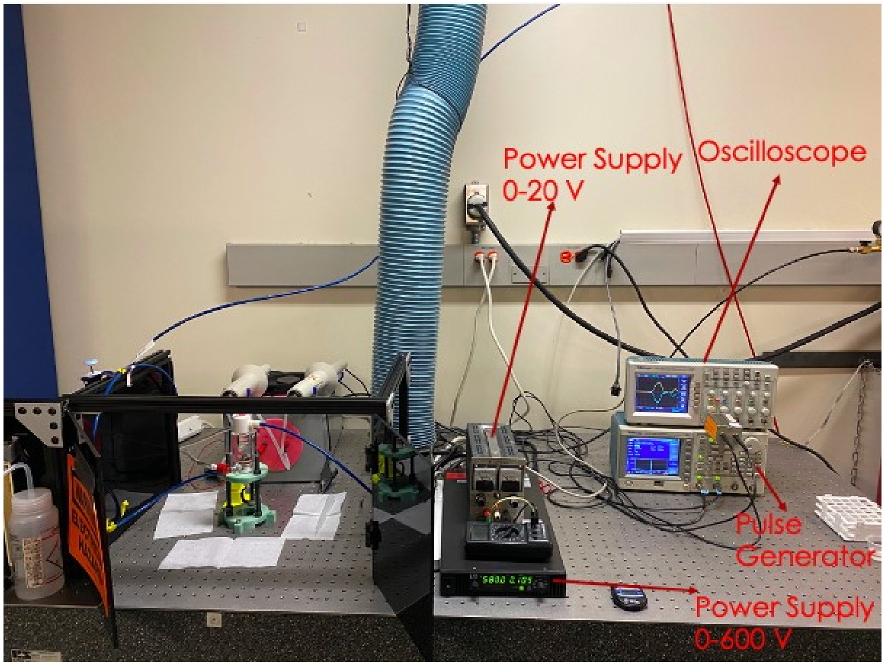

Figure 14: The electrical setup with all the electrical components connected to the plasma reactor vessel through the nanosecond pulser. The oscilloscope reads the electrical signals of the voltage pulses at both polarities of the nanosecond pulser. This was used for constantly monitoring the voltage and making sure that the graphs are identical during every PAW sample preparation (no electrical differences between samples).

The formed plasma channel is in contact with the water for 20 min. Such time was decided to be the optimum plasma treatment time based on the study performed by E. Corella Puertas *et al.*[3]. Then the PAW as well as the copper cathode are removed from the chamber for analysis and characterization. The PAW is stored in glass vials and in the fridge at ~ 4 ºC (if long term experiments on the same samples are required). Figure 15 exhibits the plasma reactor in the middle of a sample preparation process and demonstrates what the plasma discharge channel looks like in an air atmosphere.

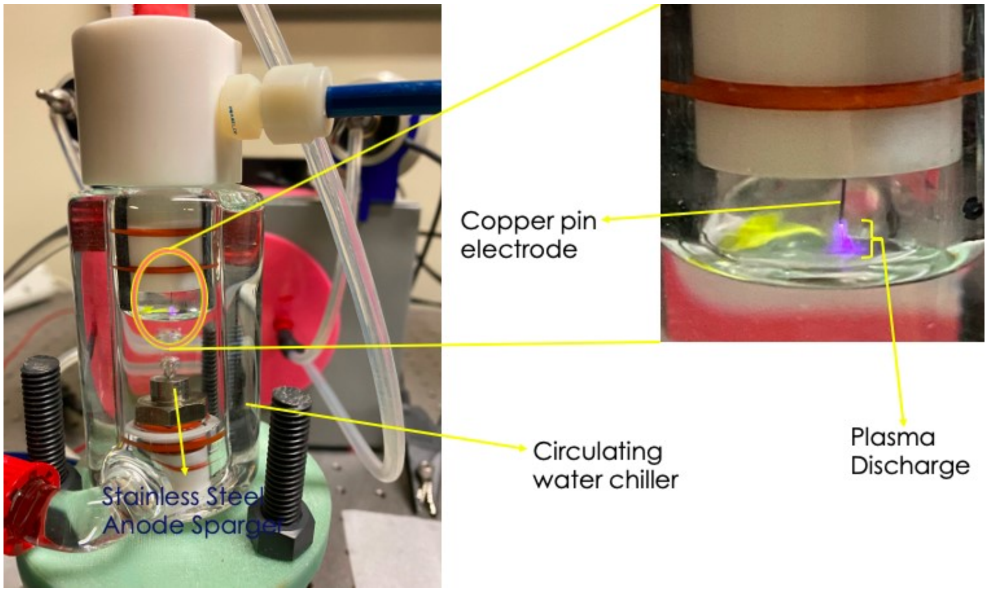

Figure 15: Plasma reactor during a sample preparation in air atmosphere. Violet plasma discharge is seen in the zoomed-in portion of the pin copper cathode millimeters above the RO water surface.

3.3 Differential Pulse Anodic Stripping Voltammetry Setup: Copper Ion Analysis

3.3.1 Overall Experimental Configuration

The ASV analysis for copper ion content involves two main stages. The first is constructing a calibration curve of copper concentrations with respect to measured current peaks for each different concentration. According to the mercury thin film study and equations (3) and (4) (seen in the literature review portion of this thesis), the correlation between bulk analyte concentration and stripping peak current should be linear. The next main stage is simply running an ASV analysis on our PAW sample and then using the calibration curve to determine the unknown concentration of copper ions via interpolation. More details of each of these steps will be discussed later in this section. Figure 16 shows a live general experimental configuration of running an ASV analysis on a PAW sample. As a final note, the model for copper ion analysis was only formulated for air plasma samples. Due to time restrictions, calibration curves for oxygen and argon plasmas were not constructed. However, they can be easily done in the future using the air plasma model described in this section, following all the optimization techniques and requirements necessary.

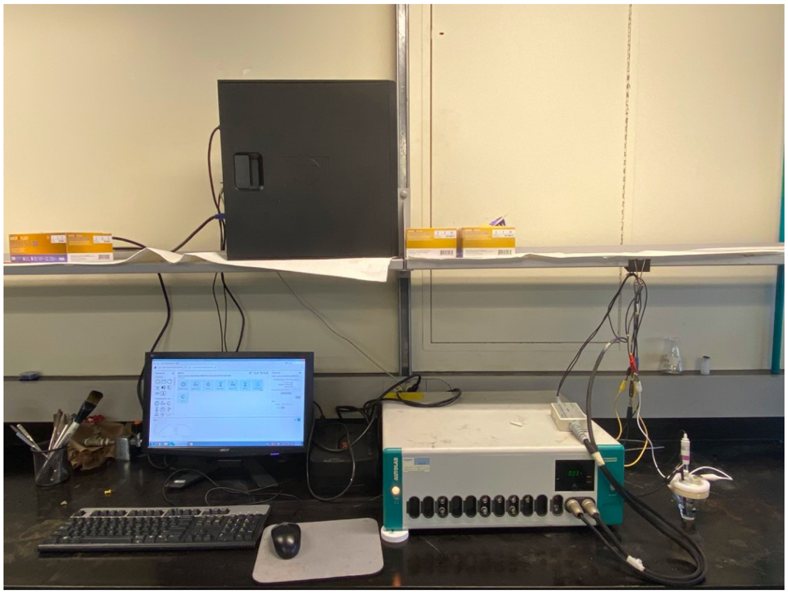

Figure 16: Full ASV setup. The electrical box on the right of the computer screen is the potentiostat (an instrument that applies voltage sweeps across electrodes). The glass funnel shaped beaker holds the PAW sample with the electrodes dipped into it. It is where the electrochemical reactions take place. The computer processes the electrical data and converts it into voltage and current plots based on what is desired. The electrochemical software used is NOVA from Metrohm Autolab.

3.3.2 External Standards Method: Construction of the Calibration Curve

The calibration method chosen for this project was the external standards method. The reason this particular method was chosen over others (such as standard additions method, which is very common for ASV analyses) is because: (1) the samples do not exhibit a matrix effect, (2) multiple analyses of the same type are to be performed throughout this investigation, whereby the same calibration curve could be used to determine copper ion concentrations, (3) approximate matrix matching is easy and (4) the preservation of the sample is crucial for long term analyses; if a standard additions method was performed, the samples would be spoiled due to spiking dilutions.[42] Furthermore, because copper nanoparticles have relatively high solublity compared to other metallic nanoparticles,[54] spiked dilutions may induce or raise the rate solubility. This can lead to overestimating copper ion content and augment the copper ion:nanoparticle ratio, additionally justifying why the standards addition method in this particular scenario is not chemically favorable.

In order to optimize the analysis, it is preferable that the unknown concentration is within the linear dynamic range (LDR). Therefore, to raise those odds, we must make sure that the detection limit (DL) and the limit of quantitation (LOQ) are very low from the lower concentration boundary. On the other hand, the upper concentration boundary should not be exaggerated so that the limit of linearity (LOL) is not too low. Putting all these aforesaid factors into consideration maximizes the LDR in a manner that favors accurate concentration interpretation.

The standard solutions were prepared via semi-serial dilution. A semi-serial dilution was performed instead of a complete serial dilution because maintaining a final volume of 50 ml for all standards was very important. This detail is accented because the depth by which the electrodes are immersed into each standard solution (during ASV) must be constant. To find an appropriate standard solution volume, the capacity of the electrochemical beaker as well as the height of the shortest electrode must be considered. 50 ml of standard solution in a 150 ml flat rimmed beaker was regarded to be the most optimal measurement because the shortest electrode (which is the gold working electrode), is sufficiently immersed into the liquid volume and the longest electrode (which happens to be the graphite counter electrode) does not touch the bottom (or walls) of the beaker.

Electrochemical experiments are very pH-sensitive, so pH matching of the standards to the air-PAW sample is essential to avoid systematic errors and inaccuracy. Using the pH meter (*Thermo Scientific*, Orion Star A211 Benchtop), every air-PAW sample produced had a pH reading of 2.3 – 2.4. This acidic medium is a result of the nitrate species in air-PAW, so nitric acid (HNO_3) was chosen to perform pH matching. The concentrate or stock solution of copper dissolved in 4% nitric acid (*SCP Science*, Plasma Cal, $[Cu^{2+}]$ 1000 μg/ml, 4% HNO_3, density = 1.021 g/ml at 23 ^{o}C) has a measured pH of 1.014. Based on a scientific estimation and on several past failed attempts to determine copper ion content in PAW, the concentration is hypothesized to be on the micromolar scale. To create an adequate upper concentration boundary with proper pH matching, the highest standard copper concentration was selected by default for a pH of 2.3 in a 200 ml solution volume. 200 ml was selected on purpose to ensure a high level of dilution to the micromolar level. From the specifications of the stock solution, the proton concentration was calculated to be 0.651 M. An acidic medium of pH 2.3 must have a proton concentration of 5 mM. Using the basic dilution formula, the aliquot volume taken from the stock was thus determined to be 1.536 ml. To translate this value back to the copper concentration of the final volume, the dilution formula was reversed using the aliquot volume (1.536 ml), the final volume (200 ml) and the stock copper concentration (which is 15.74 μM). The default final concentration of copper in the 1st standard solution (S1) was thus calculated to be 0.121 μM. Below is a summary of the explained calculations above.

Calculation of aliquot volume using dilution formula:

$$[H^+]_{Stock}V_{aliquot} = [H^+]_{pH=2.3}V_{final}$$

$$V_{aliquot} = \frac{0.2\ L \times 5 \times 10^{-3}\ M}{0.651\ M} = 1.536\ ml$$

Calculation of default copper concentration in S1 by reversing the dilution formula:

$$[Cu^{2+}]_{Stock}V_{aliquot} = [Cu^{2+}]_{S1}V_{final}$$

$$[Cu^{2+}]_{S1} = \frac{15.74\ \mu M \times 1.536 \times 10^{-3}\ L}{0.2\ L} = 0.121\ \mu M$$

The semi-serial dilution to produce the next five standards is then performed by only taking aliquots from S1 with a dilution factor of two between each standard. Below is a list of the standards with their copper concentrations and their calculated S1 aliquots. The final volume of each standard (except for S1) is 50 ml, and this final volume is achieved by diluting the aliquots with a prepared nitric acid solution with a pH of 2.3 (this is done to keep the pH constant and only to dilute the copper concentration). The aliquots for each standard are calculated using the dilution formula as shown above.

Table 1: Specifications of the Standard Solutions of Copper

All the aliquots stated in this table were extracted from standard solution S1. The aliquot used to make S1 itself was taken from the stock copper mother solution that has a cupric concentration of 15.74 µM.

Standard Solution	Aliquot Volume (ml)	Final Volume (ml)	Final Copper Concentration (µM)
S1	1.536	200	0.121
S2	33.06	50	0.08
S3	25	50	0.06
S4	16.5	50	0.04
S5	8.28	50	0.02
S6	4.13	50	0.01

Now the copper concentrations of the external standards are ready to be analyzed. Notice that only cupric ions have been considered and not cuprous ions. This is because in aqueous solutions cupric ions are more stable than cuprous ions, since their compounds' distorted tetrahedral geometric configurations in water exhibit Jahn-Teller distortions and a wide range of stereochemistries, which heightens their stability.[55,56] Though some cuprous ions are formed in PAW, they very minimal and hence negligible. This is because when copper ions will form from a metal copper rod/pin, they will readily have a d^9 electronic configuration.[56] This is in fact how the stock copper solution was fabricated: by digesting copper metal with nitric acid. The same type of digestion occurs during erosion and so the majority of copper ions in PAW are assumed to be in the cupric state.

3.3.3 Electrical Optimization and Specifications of the ASV Setup

Generally, when constructing an electrochemical setup, similar literature studies give the experimenter an idea of what settings need to be applied in order to achieve specific expected results. A type of trial and error experiments follows, with a goal of justifying these literature values. A study done by Zhuang *et al.* on trace cupric ion analysis in water samples via ASV[57], defines the important components of an ASV setup: (1) an activation or cleaning step for the active surface of the working electrode, (2) selecting a type of voltage sweep that is to be applied between the working and counter electrodes, (3) the optimization of the voltage required for copper deposition and (4) the optimization of the accumulation time for a copper monolayer deposition.[57] As for the selection of electrodes: a standard gold disc electrode with a teflon body (*BASi*, 99.95% purity, ~ 3.0 mm inner diameter) has been chosen as the working electrode, a graphite rod electrode (*BASi*, 7.5 cm long, 6 mm diameter) as the counter electrode and a saturated calomel electrode (SCE) (*BASi*, ~9.2 cm long, 6 mm outer diameter, + 0.244 V cell potential with respect to the normal hydrogen electrode (NHE)[58]) as the reference electrode. Similar to the Ag/AgCl reference electrode (that has a cell potential of + 0.210 V at 3 M KCl with respect to NHE[58]), the redox reaction that takes place within the SCE is between elemental mercury and mercurous chloride (also known as calomel), Hg_2Cl_2.[58] It has a cell notation of Cl^-(4 M)/Hg_2Cl_2(s)/Hg(l)/Pt, which tells us that the mercury and the calomel are in contact with a saturated solution of potassium chloride (KCl).[58] Though, the SCE and the Ag/AgCl reference electrode both have a porous frit that acts as the salt bridge and links the electrode to the analyte solution, the reason the SCE was chosen over the Ag/AgCl reference electrode is because the former is more robust. [58]

3.3.3.1 Gold Working Electrode Polishing

The gold working electrode must be handled very carefully, especially its active surface area (that has a diameter of 3 mm). Before beginning a set of experiments, the surface chemistry of the gold electrode must be well controlled. One common way of controlling the surface in electrochemical methods is via polishing. The polishing procedure is performed only once during this entire investigation, because re-polishing between standard and sample trials alters the surface drastically and this will in turn affect the electrical readings. If different types of grooves are created on the active surface after each polishing step, then different types of monolayers will form for each analysis. This results in inconsistent electrical readings between each trial for the same sample, which is undesirable. Thus, polishing is exclusively executed once before starting a specific set of experiments with the same objective. The polishing procedure in this analysis is implemented by using polishing paper/pad (*Anamet*, Abrasive Discs, Grain 1200, Grit 8 inches, plain back, Silicon carbide 100 pcs) mounted on a polishing machine spinner with running cold water to wet the paper. Alumina paste (*Anamet*, High Purity Alumina Suspension, Deagglomerated, 1 μm) is smeared on the pad prior to mounting, and the spinner rotates at a high speed gradually increasing from low rotations per second. When the spinner is slowly rotating the active surface of the gold electrode is pressed onto the polishing pad with both hands at a constant applied pressure. The rotator speed is then gradually increased within an interval of 5 to 10 min. Polishing is paused several times during the process so that the surface can be continually monitored – using a magnifying glass – and to ensure that it has not been severely disrupted. Once a clean flat/smooth gold surface is achieved, the electrode can be sonicated in RO water (with a resistivity of 18.2 MΩ.cm) for 15 min to clean it. Finally, the gold active surface is now set and preserved for the entirety of this investigation.

3.3.3.2 Gold Surface Activation or Cleaning via Cyclic Voltammetry (CV)

The next step is activating or "cleaning" the polished working surface of the gold electrode. Activation is the most important step because it removes accumulated residues or impurities present on the working surface prior to analysis. This procedure is done before every single ASV run/trial. If avoided, there is a risk of creating multilayers of analyte that increase the analyte film thickness and thus augment the recorded stripping current peak value according to equation (4). The cyclic voltammogram of gold gives the experimenter a very good idea about the status of the working surface: whether the surface is clean or contaminated. Looking initially at a gold electrode that is contaminated helps us discern how to properly decontaminate it and achieve a clean gold electrode with its characteristic cyclic voltammogram. Unlike bare gold, a nanoporous gold surface has different low-index crystal surface planes/faces including the 100, 110, and 111 planes.[59] Each plane oxidizes (to form gold oxide) at a slightly different potential value, however, the most distinct anodic peak is commonly observed at ~ 1.2 V and refers to the oxidation of the 100 plane (Au(100)).[59] Trailing, the 110 and 111 planes get oxidized between 1.2 and 1.4 V. These subsequent oxidations cause the anodic side of the voltammogram to develop fluctuations of peaks after 1.2 V.[59] So far, any signals on the anodic side of the voltammogram before 1.2 V are deemed to be contaminants on the gold surface. Usually in acidic media, at the start of a CV scan for a bare polycrystalline amorphous gold electrode with one type of plane, only one distinct anodic peak is observed at ~ 1.34 V.[59,60] After several repetitive CV scans though, the three oxidation peaks begin to emerge for the low-index crystal planes of Au(100), Au(110) and Au(111), which is due to the formation of gold oxides, surface roughness and defects in crystal structure respectively.[59,60]

Even though the different planes of gold oxidize at slightly different voltages, contrarywise, they all get reduced back to elemental gold at the same potential.[61] Thus, the cathodic side of the voltammogram has one strong distinct signal with the cathodic peak at ~ 0.9 V. All other observed peaks are contaminants so far. The signature cathodic peak is identical for both bare and nanoporous gold electrodes, but usually the signal strength for the latter is higher (which makes intuitive sense since all the reduction currents from all plane types are being superimposed).[59,61]

Figure 17 shows examples of constructed cyclic voltammograms for a contaminated gold working electrode. Both Figures 17A and 17B were obtained by running 20 non-optimized CV scans on previously contaminated gold working electrodes (contamination is induced by simply running an ASV copper analysis). The well-known redox peaks at 1.2 and 0.9 V are properly observed in both cases. However, a strong intruding anodic peak is seen at ~ 1 V, and this peak has a corresponding cathodic peak at ~ 0.75 V (for both graphs, but more heightened in 17A). This is clear evidence of an impurity present on the active surface. The identity of this impurity was unknown and was thought to range from being due to residues or graphite electrode leaching from a previous ASV experiment such as the leaching of nitrates, copper ions or even copper oxides, which can react with sulfuric acid to produce a new reducing agent.[62] However, work done by L. D. Burke *et al.*[61] has shown that this impurity arises from the redox reaction of hydrous gold oxide species formed on the gold surface. The study does not refer to this phenomenon as an "impurity" so to speak, but rather as a normal characteristic attributed to the cyclic voltammogram of polycrystalline gold in acid. Nevertheless, we have observed height/intensity inconsistencies with this peak and have classified it as an impurity that must be eliminated or minimized. Furthermore, this peak in literature reviews always appeared at very low currents, ~ 1 μA, justifying that its presence at much higher current intensities is not optimal for gold.[61]

Continuing, by comparing both graphs, one can deduce that by raising the molar concentration of sulfuric acid in which the gold electrode is being activated, then the amount of impurities decreases – Figure 17B has an additional contamination with an anodic peak at ~0.68 V (unknown identity, surmised to be caused by copper aggregates in H_2SO_4 with a shift in anodic peak position due to changes in pH between exchanged media).[62] Even though the intensity of the anodic peak at 1 V with 1 M sulfuric acid (pH ~ 1.073) is higher than at 0.5 M sulfuric acid, it is much easier to deal with one type of impurity than two different types. It is important to note that Figure 17 is merely a sample taken from several CV runs (~ 100 different runs) of the gold electrode used in this project. The graphs show what is usually observed with CV after an ASV analysis takes place. Hence, in order to commence the next trial, a CV command/setting must be developed such that a clean gold electrode is always achieved after ASV.

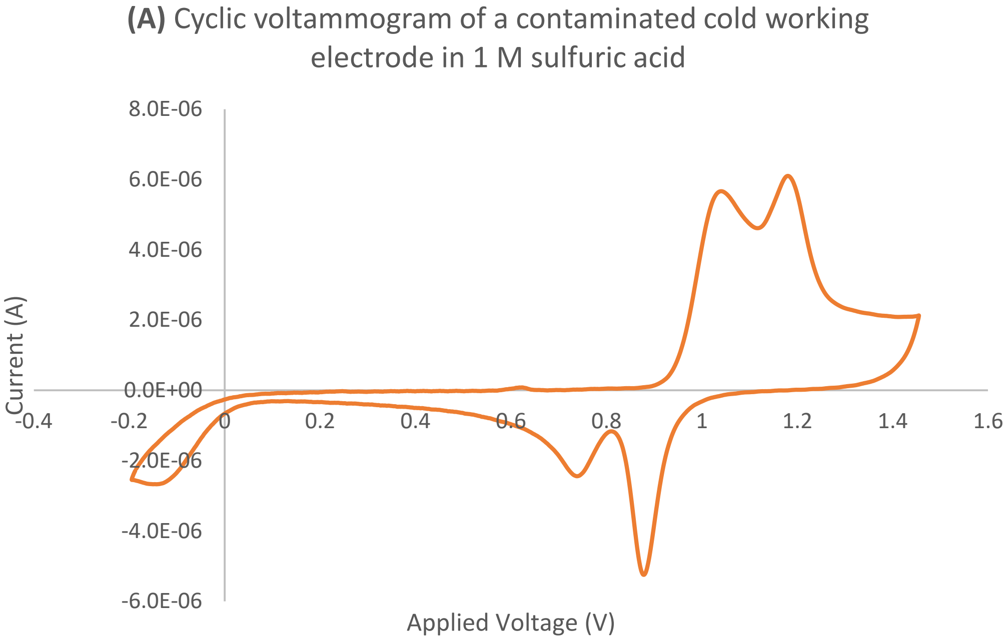
(A) Cyclic voltammogram of a contaminated cold working electrode in 1 M sulfuric acid

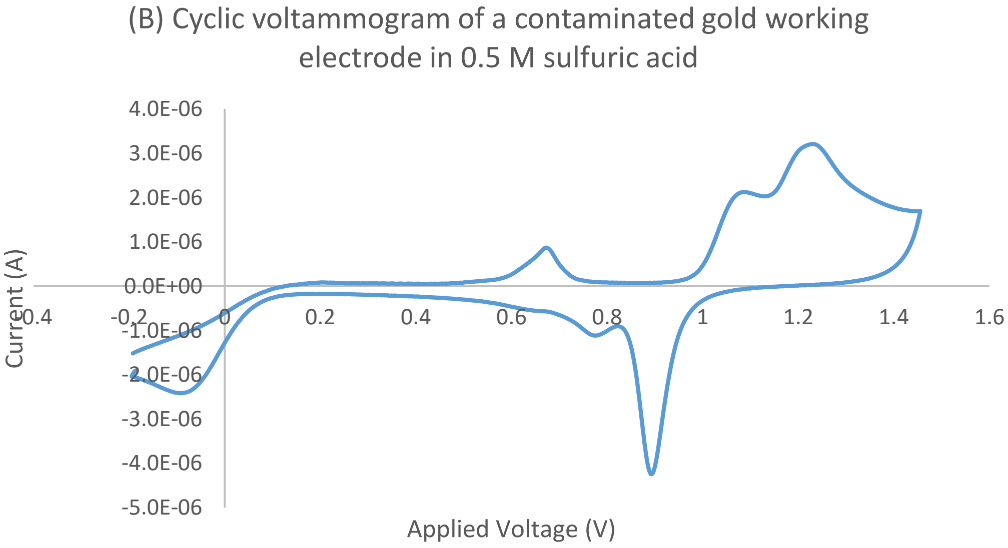
(B) Cyclic voltammogram of a contaminated gold working electrode in 0.5 M sulfuric acid

Figure 17: (A) Exhibits contamination peaks in a gold working electrode cyclic voltammogram with a sulfuric acid solution of 1 M, and (B) exhibits the same as (A) but in a sulfuric acid solution of 0.5 M. Note that only the last CV scan of 20 is graphed in both cases. Both CVs had a scan rate of 0.1 V/s.

Experimentation has shown that if this contamination is left unresolved, the impurity peaks will steadily keep augmenting in intensity (reaching over 1 x 10^{-5} A) with every following trial (since the impurity layer becomes thicker with every trial), indicating inconsistencies in the surface chemistry and topology of the active surface, which will eventually lead to huge error bars or low precision between trials as well as inaccurate results. So, in a way, activation via CV allows the experimenter to monitor and control the gold working surface in addition to surface polishing.

Using a modular line low current potentiostat/galvanostat instrument (*Metrohm Autolab*, AUT71771) and a software called NOVA 2.1.4 (*Metrohm Autolab*, 2018), a setting can be designed to run a customised CV staircase run with additional linear potential sweeps if needed. The potentiostat is connected to the electrochemical vessel via banana clips that are attached to the electrodes. It is the instrument that conducts different types of voltage sweeps across the electrodes of the setup with NOVA acting as the instructor. After several attempts, the most optimal CV staircase command protocol found to yield a consistent clean enough gold working electrode CV profile has the following properties: (1) a start potential of – 0.455 V, (2) an upper vertex potential of 1.455 V, (3) a lower vertex potential of – 0.455 V, (4) a stop potential at – 0.45 V, (5) a scan number of 20, (6) a scan rate of 0.1 V/s and (7) a step of 0.00244 V. Moreover, in order to further eliminate or reduce the pronounced hydrous gold oxide impurity at 1 V a constant potential sweep is applied at 0.75 V for a duration of 200 s prior to the CV staircase command. The current with respect to time is recorded and monitored, in order to ensure that it eventually tends to 0 A as time tends to infinity (a clear indication of impurity expulsion or reduction back to pure gold on the gold active surface). Figure 18C depicts an example of the majority of current vs. time profiles observed, for this profile was almost seen to be identical for every CV analysis that was performed hereon. As a final note, the same solution of sulfuric acid was never used twice for activation, in order to avoid the redeposition of any impurity aggregates within the solution from previous CV runs onto the surface. Figure 18 shows examples of the majority of CV recordings for a clean gold surface obtained with consistent final CV profiles. Only the first and last scans are graphed.

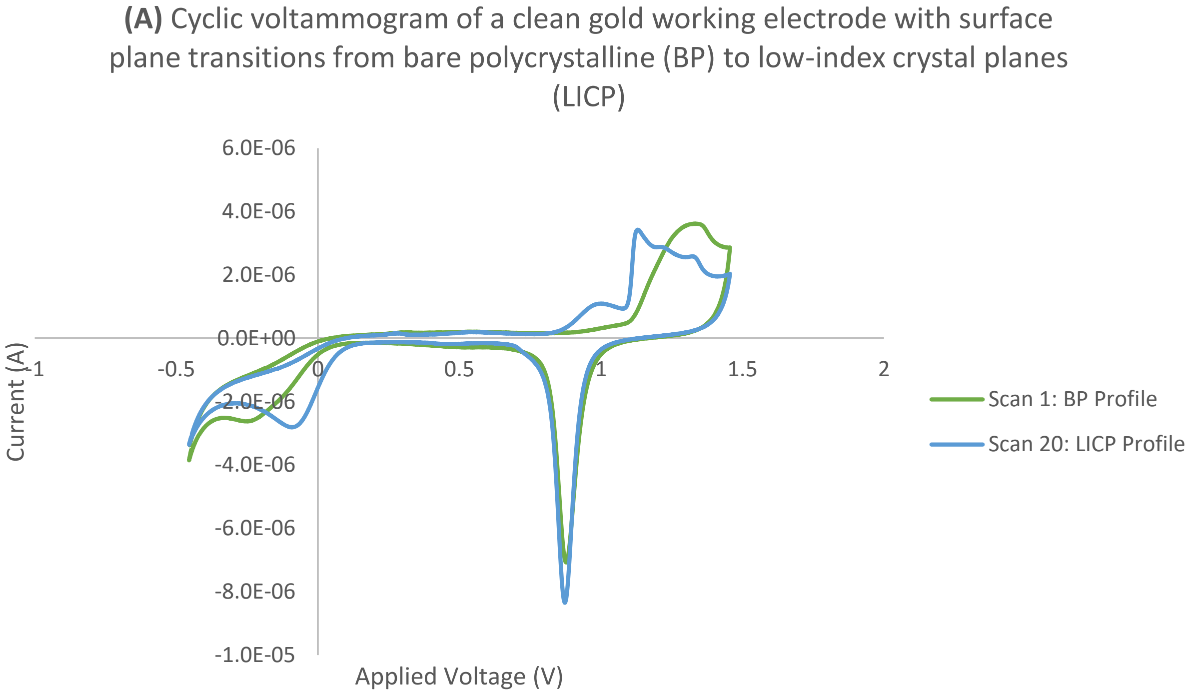
(A) Cyclic voltammogram of a clean gold working electrode with surface plane transitions from bare polycrystalline (BP) to low-index crystal planes (LICP)

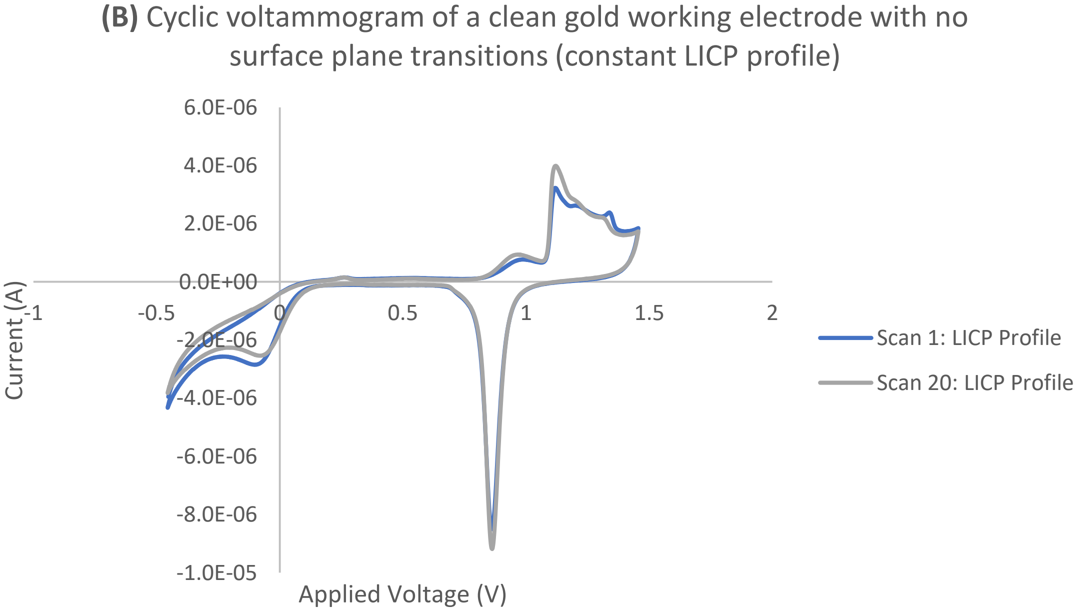
(B) Cyclic voltammogram of a clean gold working electrode with no surface plane transitions (constant LICP profile)

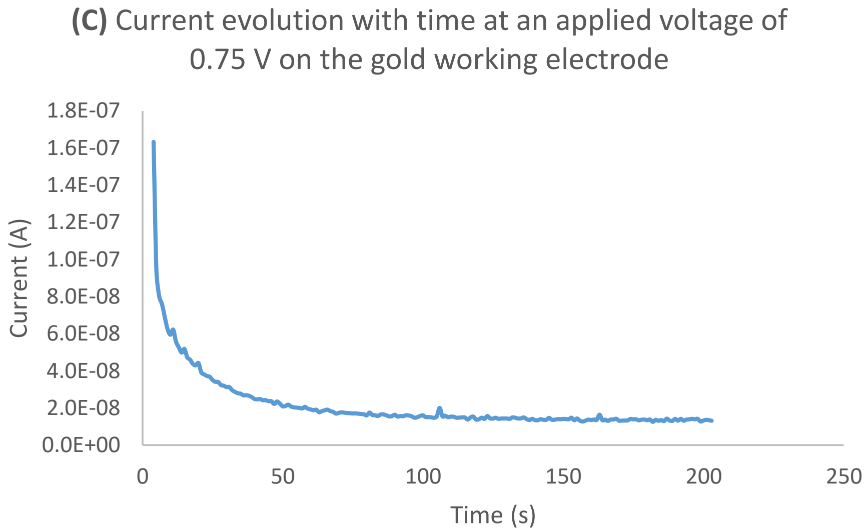

Figure 18: (A) Demonstrates how the cyclic voltammogram of the gold working electrode evolves from a bare polycrystalline profile (scan 1) to one with low-index crystal planes (scan 20). It is experimentally seen that the transition is usually complete by the 10th scan with all the scans from 10 to 20 overlapping (completely identical). (B) Demonstrated a cyclic voltammogram of the working electrode starting and ending with an LICP profile. (C) Demonstrates the evolution of current with time at an applied voltage. Used to reduce the hydrous gold oxide layer back to gold. The tendency of current to 0 A is a crucial characteristic telling us that no new phenomenon is being oxidized and reduction processes are halting (in this case).

The last scans of the CV runs are the most important, since they depict the final status of the gold surface, and it is this final scan that must be maintained or identical for every CV analysis. Even though the hydrous gold oxide anodic peak is still observed at lower magnitude at the last scan for both graphs at ~ 0.98 V, the importance is that it remains consistent throughout all trails and does not inflate with time. Furthermore, making it as minimal as possible with a current of ~ 1 x 10^{-6} A such that the cathodic peak is barely even observed, reduces the amount of systematic error drastically. If we compare Figures 18A and 18B, we see that 18A shows a transition from a bare gold polycrystalline surface with no hydrous gold oxide anode peak to the formation of low-index gold crystal planes Au(100), Au(110) and Au(111) with anodic peaks of ~ 1.17, ~ 1.25 and ~ 1.34 V, respectively. The reason behind this transition is due to the evolution of surface roughness and defects of the gold surface that originate from the imperfect reduction of the initial gold oxide monolayer.[59] Regardless, the formation of these different facets is very advantageous on the long term because it increases the surface area of the active gold surface, allowing more contact and easier adsorption with the analyte.[59] On the other hand, Figure 18B shows that this transition is not always present or necessary, and that gold oxides with different crystal planes can emerge from the beginning. A slight increase in current is seen between scans 1 and 20 in 18B, which is due to the incomplete reduction of the gold oxide layer from the previous scan resulting in a slight increase in overall oxide layer thickness. At the end, what is essential is that the final CV scans of Figures 18A and 18B have comparable global extrema at ~ 4 x 10^{-6} A and at ~ – 1 x 10^{-5} A and almost identical cyclic voltammemetric features.

One feature that has not been mentioned is the peak seen on the cathodic side at the far left of the voltammograms in Figures 17 and 18. This peak has been ignored in this analysis because it is consistent in a clean or contaminated gold working electrode at ~ – 2 x 10^{-6} A. Though this peak had minor voltage shifts, it has not fluctuated drastically in current throughout the entire investigation and so was not classified as an impurity. However, according to all literature reviews studied, it is not abundantly seen in classic cyclic voltammograms of gold and so cannot be classified as a normality. Therefore, because its further study is non-influential to this research, it has been disregarded.

In the end, the objective of this methodology is to monitor and control the surface/surface chemistry of the active surface of the gold working electrode. This was indeed achieved at the end by obtaining consistent identical cyclic voltammemetric analyses for every single run performed. All features of the voltammogram have been considered, identified and classified as known features or irregularities, with the latter compensated for appropriately.

3.3.3.3 Differential Pulse Voltammetry vs. Linear Sweep Voltammetry

After the gold working surface is activated, only one ASV trial for one specific standard can be recorded. Before the next trial can begin, the working electrode must be reactivated with a fresh sulfuric acid solution. This means that the reaction vessels of sulfuric acid and standards/samples are constantly alternating. When the electrodes are dipped into the electrolyte, it is essential that they are not touching one another or the walls of the beaker. Moreover, in order to minimize the ohmic drop, the electrodes are positioned accordingly on the holder with their tips converging (the parafilm aids in fixating slanted electrode positions).

When standard analyses are performed, the first sub-objective is graphically locating the stripping current peak of copper. As a reference point, our expected voltage values were based on the study conducted by Zhuang *et al.*, where the oxidation peak for copper was found to be at ~ 0.35 V with a deposition voltage or an accumulation voltage of – 0.4 V (their reference electrode was an Ag/AgCl electrode, but conversions to SCE were definitely accounted for).[57] Since there are different types of potential-time waveforms used for stripping, the simplest and most common option is the linear sweep voltammetry or a linear ramping of the potential (also known as staircase voltammetry). However, a major concern with linear sweeping is that this potential-time waveform does not minimize non-faradaic (also known as capacitive) current readings, because the current at the gold electrode is constantly being measured at every moment while the voltage between the reference electrode and the working electrode is swept linearly with time from low to high potentials.[46] Staircase voltammetry is a derivative of linear sweep voltammetry that compensates for the presence of capacitive current readings by adopting potential sweeps in a series of ascending or descending stair steps.[44] The minimization is achieved because the current is only measured at the end of each voltage change (exactly before the next potential step), whereby the non-faradaic current is low.[44] As hinted previously, a CV staircase command was employed for the gold working electrode activation procedure, which is basically a staircase voltammetry run in a continuous cycle. The new challenge is now to decide whether or not this setting is also optimal for ASV analysis. Figure 19 illustrates the difference between linear sweep voltammetry and staircase voltammetry.

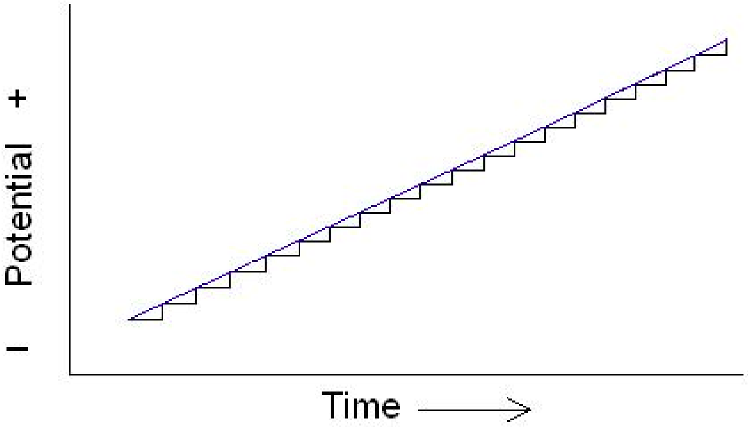

Figure 19: Shows how staircase voltammetry is derived from linear sweep voltammetry. While linear sweep voltammetry measures current at every point in time, staircase voltammetry gives time for non-faradaic currents to sufficiently recede before recording a current measurement (Figure extracted from Wikimedia).

Another potential-time waveform candidate called differential pulse voltammetry (DPV) has the ability of not only reducing non-faradaic readings but also enhancing the sensitivity and lowering the background signals that can be problematic in linear scans (depicted in Figure 20).[46] It is constructed by periodically superimposing relatively large amplitude (50-100 mV) pulses on a shallow linear staircase voltage (~ 5 mV/s) for short periods.[46] The produced pulse train is characterized by a pulse height in mV and a pulse width in ms.[43] The main advantage of this method is the fact that the current is sampled twice during each cycle, once prior to the pulse application and once at the end of the pulse life, each with the same recording time interval.[43] The difference between these two currents yields ΔI, which is the value that is amplified and read out.[44] It was hinted previously that non-faradaic currents decay faster than faradaic currents, so manipulating the recording time interval controls the levels of capacitive current measured since the current at the end of a pulse life is predominantly faradaic.[46] This thus gives the experimenter the freedom to eliminate capacitive current readings almost completely. Figure 20 explains graphically how DPV enhances the minimization of capacitive current readings.

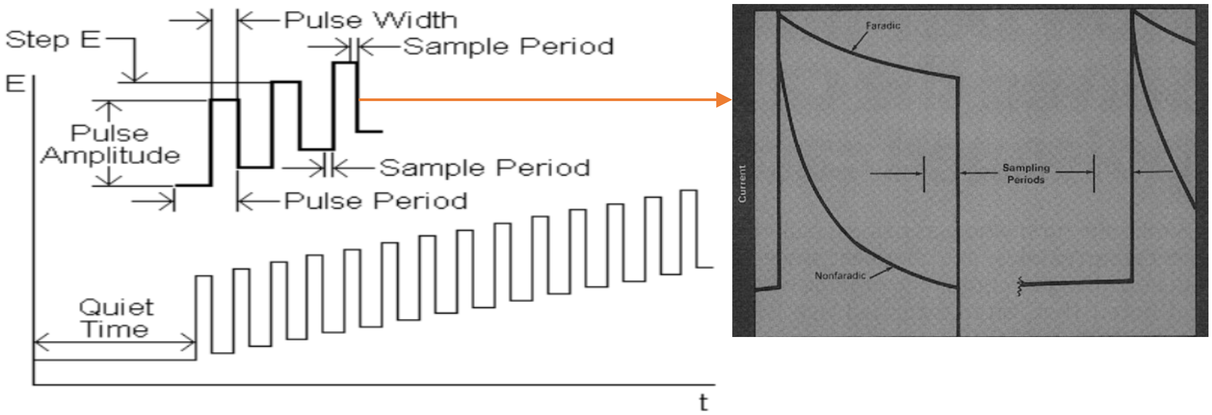

Figure 20: Shows the construction of DPV from linear and staircase voltammetry where E denotes the potential. The side image on the right shows what is happening in parallel to the voltage pulse in terms of current with respect to time. It explains how non-faradaic readings are minimized based on the sampling periods' positionings in time.[46]

Another advantageous aspect of DPV is that during the stripping process, the oxidized analyte does not have enough time to diffuse far away from the active surface of the working electrode before the pulse ends.[46] When the pulse falls (the rest period between pulses), the voltage reaches back to the reduction potential range and redeposits a significant amount of analyte onto the active surface.[47] This results to multiple readings from the same analyte to occur (repetitive contributions of the same analyte to the measured current), whereas the same analyte can contribute only once to the measured current in linear sweeping voltammetry.[46] In turn, repetitive contributions lead to an enhancement in sensitivity and signal-to-noise ratio (SNR).

As a final note, it is important to mention that the theoretical linear correlation (direct proportionality) between bulk analyte concentration and stripping peak current described by Osteryoung *et al*. in equations (3) and (4) still applies to differential pulse anodic stripping voltammetry (DPASV) with an added dependence on the pulse width (t).[48] Equation 9 describes the final expression for the stripping peak current when performing a DPASV analysis (proving the conservation of direct proportionality between C and i_p):[48]

$$i_p = 0.138nFACLt^{-1} \tag{9}$$

In the end, because of the enhanced sensitivity and SNR along with the minimisation of capacitive current readings, DPASV has been selected as the optimal method for copper ion analysis of PAW. To locate the stripping peak at ~ 0.3 V a DPASV run was performed on a standard (S2) with an applied deposition voltage of – 0.3 V and an accumulation time of 150 s (both values randomly chosen and based on literature reviews). Figure 21A and 21B exhibit the evolution of the resulting current during the deposition period and the acquired stripping peak at ~ 0.23 V (it is overlaid with a blank reading), respectively.

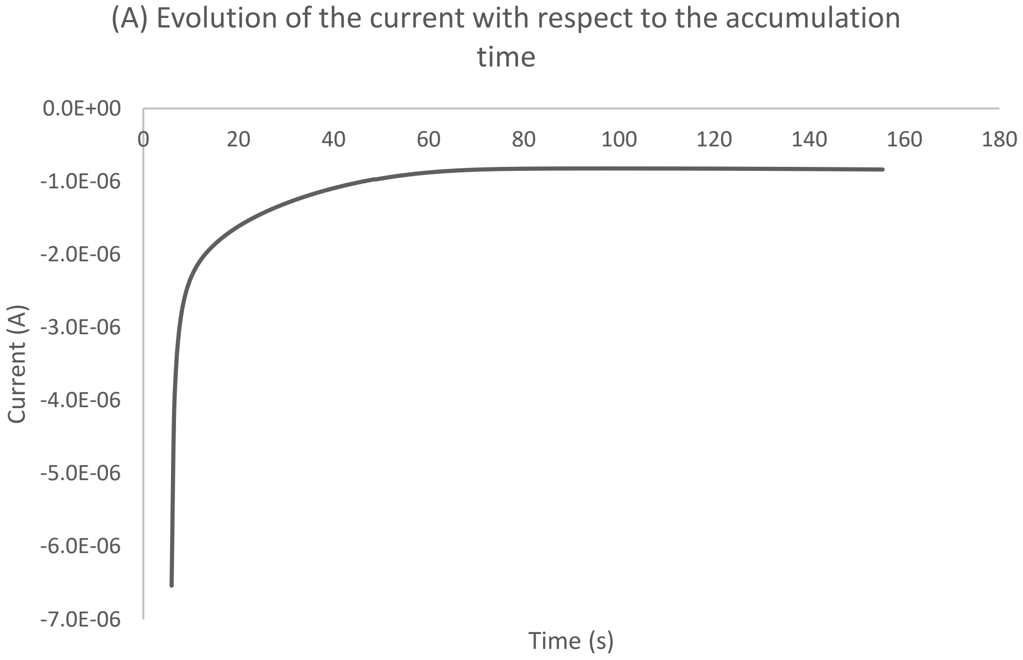

(A) Evolution of the current with respect to the accumulation time

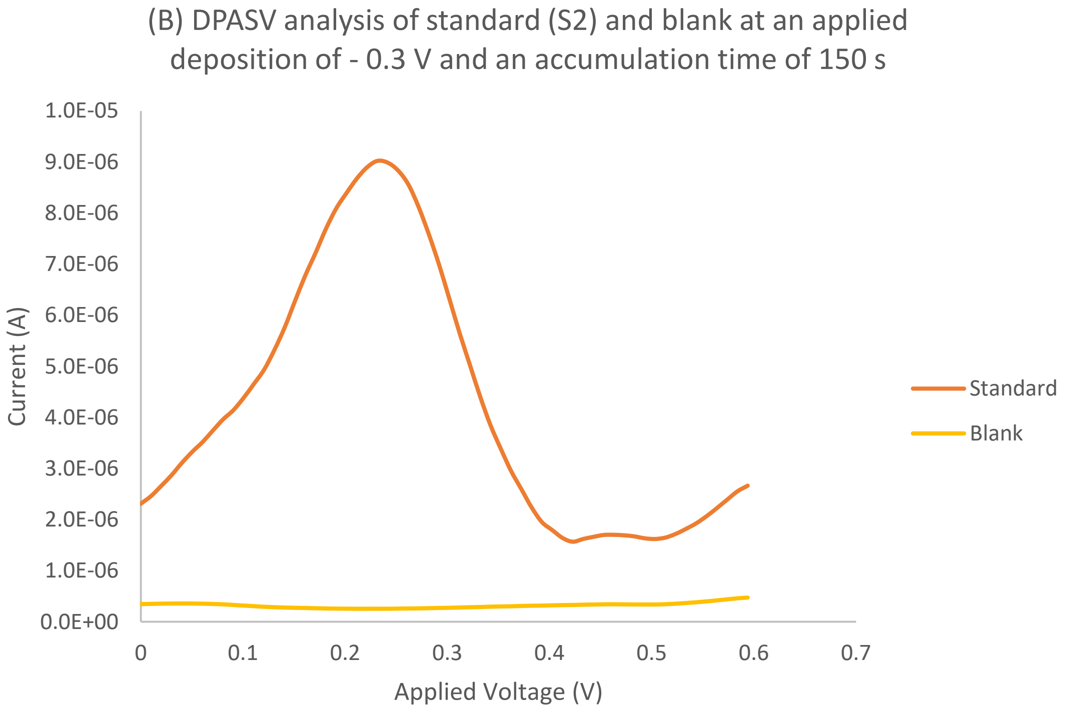

Figure 21: (A) Shows the change in current during the deposition process. (B) Observation of the stripping peak after running a DPASV on standard (S2) and a blank with a deposition voltage of – 0.3 V and an accumulation time of 150 s.

The DPV command setting that resulted in Figure 21B has the following properties: (1) a start potential of 0 V, (2) a stop potential of 0.6 V, (3) a step of 0.01 V, (4) a modulation amplitude of 0.05 V, (5) a modulation time of 0.1 s, (6) an interval time of 0.1 s and (7) a scan rate of 0.10071 V/s. From Figure 21B one can see that the oxidation voltage is at ~ 0.23 V, which is inconsistent with previous literature findings. However, the blank reading (which is simply the solvent solution of pH = 2.3 used to dilute all the standards) shows no peak at all, proving that the observed peak does indeed represent the copper ions in the standard solution. Furthermore, it justifies that no other constituent of the solution (nitrates, oxygen, carbon dioxide, etc.) exhibit any interfering redox reactions within the applied DPV voltage sweep range. Hence, there are no superimposed interfering peaks with that of copper ions. Figure 21A can be said to be a chronoamperometric analysis of copper deposition based on the Cottrell equation (equation (2)) since the current is diffusion controlled. Electromigration dependence has been eliminated due to the large presence of nitric acid in solution with pH = 2.3, which will dominate in carrying the bulk of the current through the solution; convection dependence is partially eliminated since electrolyte stirring and/or electrode rotation have been avoided in these experimentations. After circa 10 s, natural convection kicks in due to the difference in density of the electrolyte at the electrode surface and in the bulk (as a result of different Cu^{2+} ion concentrations). This implies that the Cottrell equation applies only for the first circa 10 s of the experiment excluding the first milliseconds since, initially, the current is electron-transfer controlled and there is the double-layer charging current.[42] It shows us and further justifies the presence of cupric ions in solution being reduced onto the active surface of the gold electrode. The evolution of current from non-faradaic (at the highest current of ~ – 6.45 x 10^{-6} A) to faradaic current (between 10 s to 40 s) to an exponential decay tending to 0 A, justifies the depletion of cupric ions in the bulk solution.[42] The Cottrell equation predicts that the deposition current is proportional to the inverse square root of time and describes a theoretical behaviour that is only observed at times greater than at least a few milliseconds (faradaic current region).[42] However, concentration calculations in this investigation are not performed based on chronoamperometry recordings. The chronoamperometrogram is solely used for a second visual verification of copper ion redox processes taking place, but the properties of this chronoamperometric run – meaning the applied reduction voltage and the accumulation time – are indeed what determine the final interpreted concentration value.

In the end, because the peak position of copper was significantly shifted based on Figure 21A, this means that the stripping current peak value may be equally misinterpreted too. An optimization for the reduction voltage as well as the accumulation time must henceforth be performed, as these parameters affect the final interpretation of the stripping current peak and thus copper concentration.

3.3.3.4 Deposition Voltage and Accumulation Time Optimization

The deposition or reduction voltage as well as the accumulation time are both optimized in the same fashion. The procedure basically entails running many different DPASV analyses with several different values of reduction voltages while keeping the accumulation time constant and then vice versa. Only the peak current values are recorded every time and then plotted against their corresponding applied reduction voltage or accumulation time value (depending on what is being optimized). When the peak current change tends to 0 A (meaning the graph plateaus), then the value at the edge/beginning of the plateau corresponds to the optimal value.

Figures 22A and 22B show the optimization graphs for the reduction voltage and the accumulation time, respectively. For the optimization of the reduction voltage (Figure 22A), the domain ran from – 0.1 to – 0.7 V with an increment of – 0.1 V per run and at an accumulation time of 160 s (arbitrarily chosen based on Zhuang *et al.*[57]). The current begins to plateau at ~ – 0.5 V, and so – 0.5 V is deemed to be the optimum reduction voltage for cupric ions at a pH = 2.3. Now that the optimal reduction voltage is established, it is kept constant at – 0.5 V while varying the accumulation time from 100 s to 220 s with an increment of 20 s per run. Doing this yields Figure 22B, which exemplifies that the optimum accumulation time for deposition is at ~ 150 s.

This thus concludes the optimization steps with an optimum reduction voltage and accumulation time of – 0.5 V and 150 s, respectively. Now the standards can deposit copper metal at these specified values and strip the formed layer via DPASV with an activation of the gold electrode prior to every single trial.

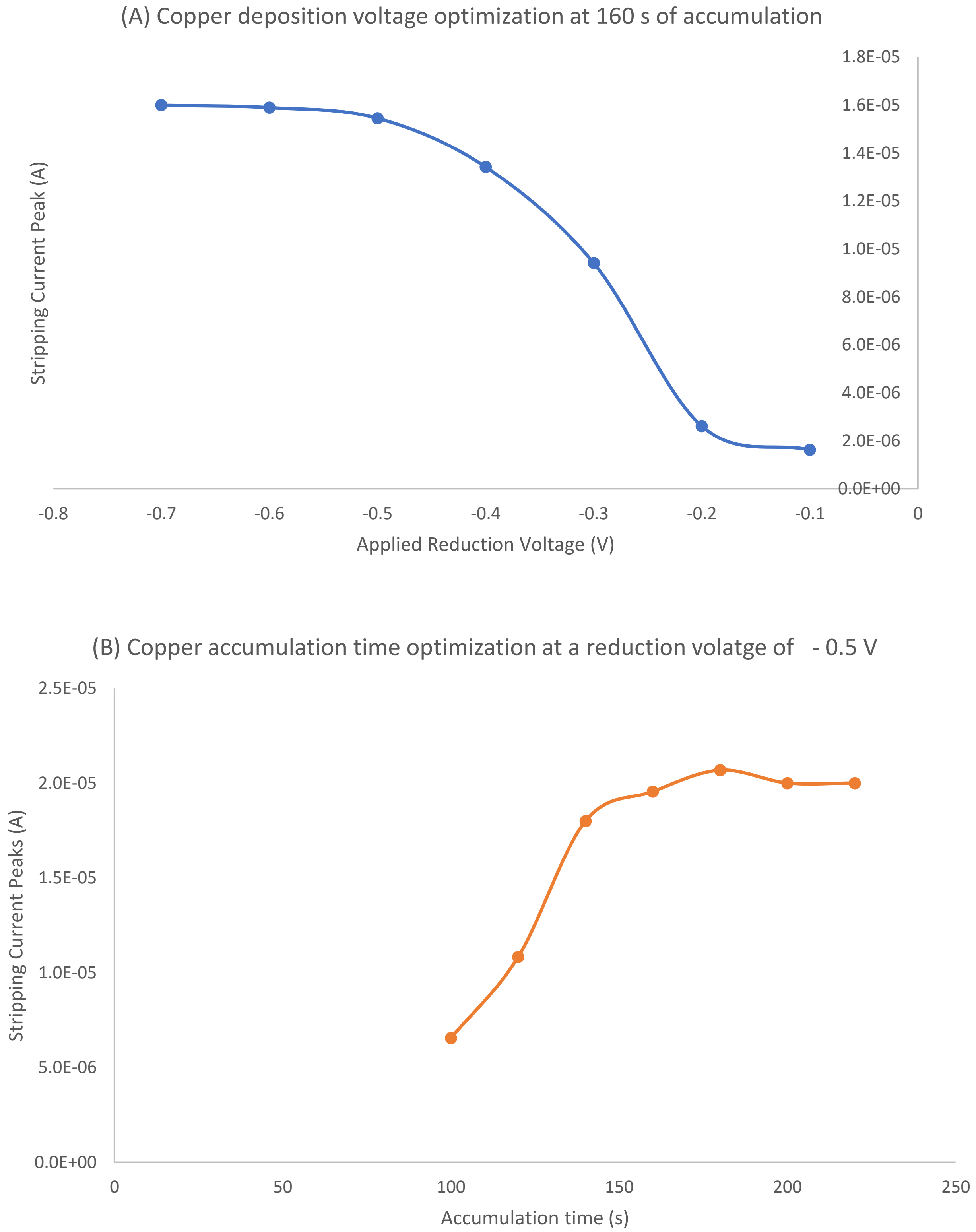

Figure 22: (A) Shows the output of the optimization procedure for the reduction voltage of copper on the gold electrode. (B) Shows the output of the optimization procedure for the accumulation time of copper on the gold electrode.

Figure 23 shows a schematic that summarizes the setup that has been thoroughly described in this section. It illustrates the induced redox reaction of cupric ions in the standard solutions. It is important to note that Figure 23 is not to scale and that the electrode configuration as well as the depth at which they are immersed in the standard solution are inaccurate. This figure is only used to visualize the redox reaction process.

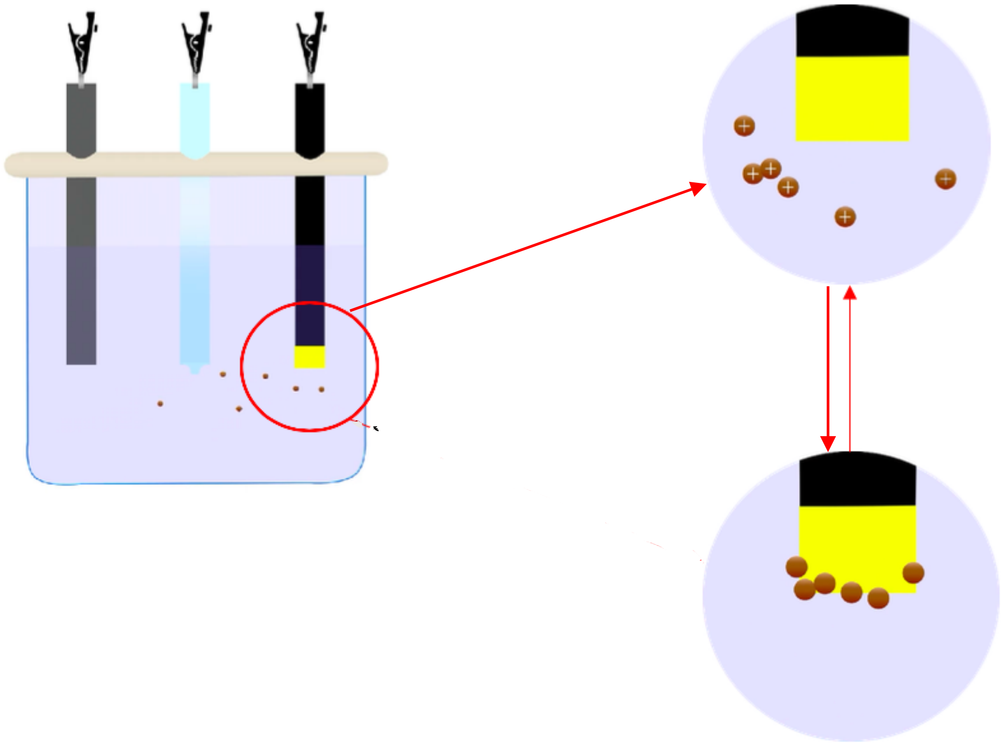

Figure 23: Schematic of the DPASV experimental setup. The whole figure on the left represents a standard solution being analyzed. The three stick-like figures are the electrodes: right = gold working electrode, center = SCE, left = graphite counter electrode. The orange-brown dots depict the cupric ions in solution diffusing. When the reduction voltage is applied for the duration of the accumulation time, the cupric ions will diffuse towards the active surface area of the gold electrode (yellow region) (top right zoomed in portion). The zoomed in portion of the active surface area on the bottom right demonstrates the deposition of the cupric ions onto the surface and being reduced into copper metal to form a metal layer (orange dots do not have + signs). The first version of the zoomed in portion (top right) simultaneously demonstrates the stripping/oxidation step (which follows the deposition step) of the metal copper layer back to cupric ions that will diffuse back into the bulk of the solution (orange dots get back their + signs) once DPASV is run.

Finally, after all the standard solutions have been analyzed and the calibration curve constructed, the PAW samples can be analyzed, and the obtained date interpolated into the calibration curve to determine the unknown concentration of cupric ions. Figure 24 shows a labeled picture during the DPASV analysis of a random PAW sample. Notice how the electrode tips are converging towards one another but not touching each other or the walls of the funnel shaped beaker. Moreover, the shape of the beaker invokes electrode tip constriction.

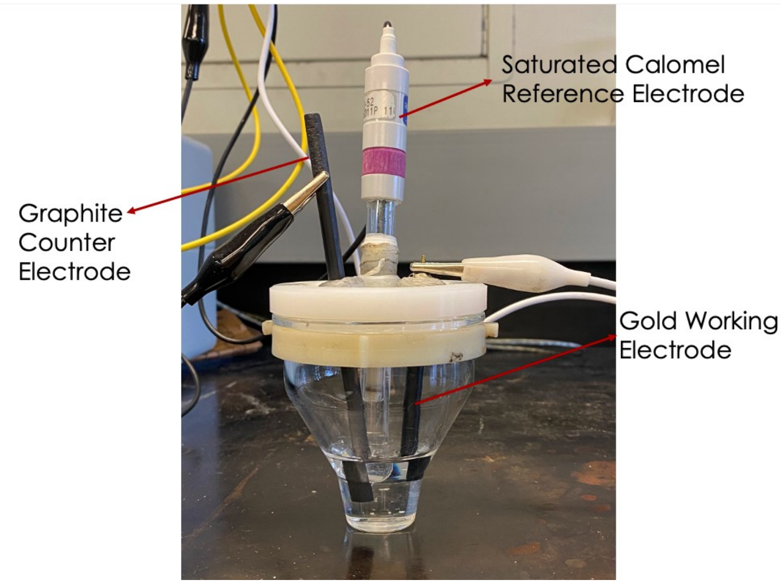

Figure 24: Live picture during the DPASV analysis of a random PAW sample. This funnel shaped beaker is purposely used for the analysis of liquid samples that are of small volumes. The electrode holder is custom made teflon.

3.4 Malvern Zetasizer Nano ZS: Copper Nanoparticle Size Analysis

3.4.1 General Experimental Configuration

Now that the copper ion content analysis has been disclosed, we may move on to developing a method of analyzing the copper nanoparticle content.

One method of characterizing the copper nanoparticles formed from electrode erosion is by determining their average size. As discussed in the literature review section, this particle size analysis is achieved via DLS. An instrument called the Malvern Zetasizer Nano ZS (*Malvern Panalytical*, 0.3 nm – 10.0 µm diameter measurement range, 0.1 mg/ml sensitivity) applies the

DLS technique on samples introduced into the instrument through the use of disposable low volume polystyrene cuvettes (*Malvern Panalytical*, capacity ~ 1 ml, minimum sample volume ~ 40 µl, ZEN0040). Since the solvent is water, then these aforementioned cuvettes are the best cell choice as the sample scatters a decent amount of light. Figure 25 shows a general schematic of a Zetasizer's inside DLS setup and mechanism. The Zetasizer instrument that we are working with measures light scattering information close to 180°. This is known as backscatter detection.

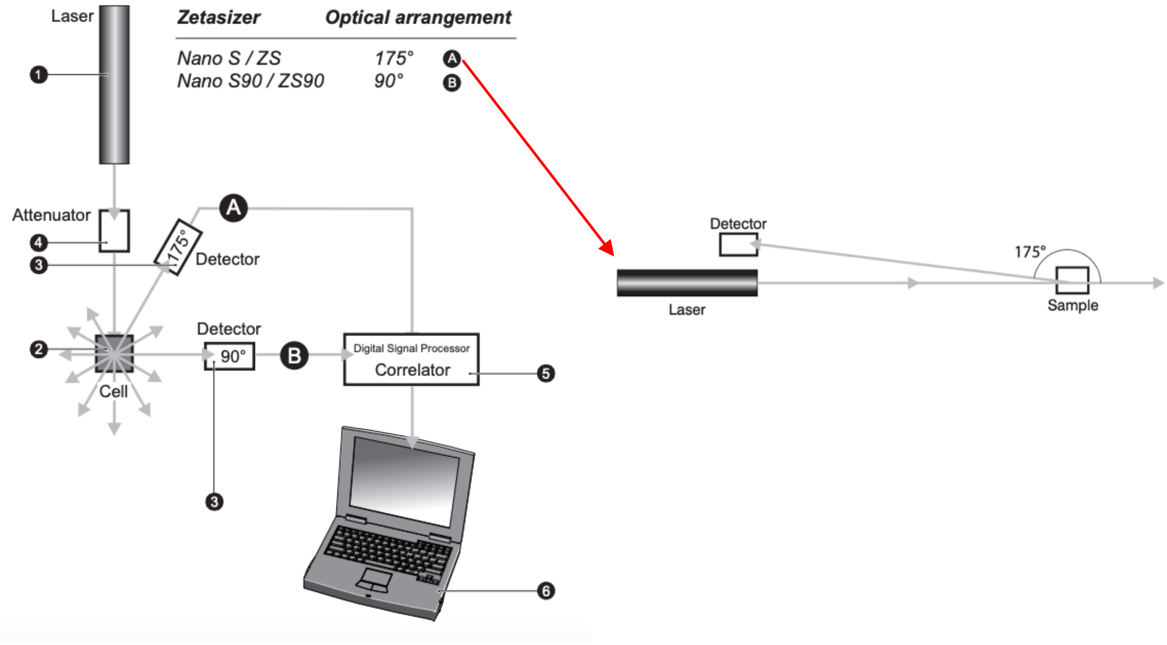

Figure 25: A schematic of the DLS setup within the Malvern Zetasizer Nano ZS/S and Nano S90/ZS90. Configuration (A) represents the DLS setup we are interested in with a 175° detection optic (also known as backscatter detection).[63]

1 ml of each PAW sample that has been treated for 20 min is transferred into the disposable cuvettes for analysis. Since three different trials are required for every type of gaseous atmosphere considered (argon, air and oxygen) to produce PAW, then a total of 9 PAW samples are analyzed. Each of these 9 samples are themselves run through three different DLS analyses, so there is a total of 27 recordings at the end. For every DLS run, the intensity and volume size distributions are tabulated as well as the Z-average diameters (Z-avgs) and the polydispersity indices (PDIs).

3.4.2 PAW Sample Interpretation, Preparation and Insertion

Except in extreme circumstances, the Zetasizer will always be able to scatter light sufficiently even at very low concentrations of analyte.[63] Thus, the detection limit of the instrument is of no concern to us. As for the upper limit of concentration, in order to avoid multiple scattering and interparticle interactions (which inhibit random/free diffusion of the analyte), the general maximum concentration of analyte is not recommended to exceed 5% by mass assuming a solvent density of 1 g/cm^3.[63] Since the total copper content resulting from erosion is on the order of micromolars in a water volume of ~ 7.5 ml (interpreted from preliminary experimentations), then the upper concentration limit does not surpass 5% by mass. With that, it is clear that the upper concentration boundary does not limit our experimentation and does not create instrumental analysis complications; however, the minimum concentration boundary may cause a few problems, since as we approach the DL (micromolar concentrations in a 7.5 ml water volume is considered to be minimal), the collection of scattered light becomes minimal. Therefore, some considerations must be accounted for during PSA via DLS: (1) for detected particle sizes less than 10 nm, the concentration should generate a minimum count rate of 10,000 counts per second (10 kcps) in excess of the scattering from the water dispersant/solvent, and (2) for detected particles in the diameter size range of 100 nm to 1 μm, Figure 26 shows an estimate plot that describes the lower limit of particle number required to avoid the effect of "number fluctuations" for different overall concentrations ("number fluctuations" arise due to severe fluctuations of small momentary number of particles in the scattering volume).[63] These two considerations must be and are respected/monitored throughout PSA; only then are the DLS recordings deemed to be very reliable.

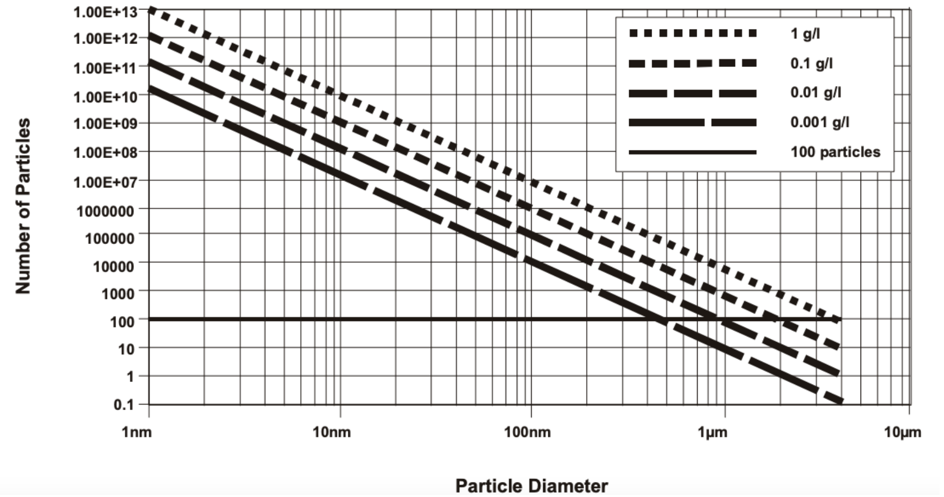

Figure 26: Estimate plot determining the minimum amount of particle number for different analyte concentrations required with respect to the particle diameter detected. The density of the solvent/dispersant for this plot is assumed to be 1g/cm^3.[63]

After the PAW sample preparation is complete, 1 ml is slowly transferred to the disposable cuvette from the bottom up in a tilted manner in order to avoid the formation of air bubbles on the walls. The depth of the sample must be a minimum of 10 mm from the bottom of the cell. Next, the cuvette walls that will be exposed to the laser beam must be cleaned/polished with laboratory Kimwipes to ensure that minimal light is scattered due to debris on the cell walls. The polished optical surface is usually marked with a triangle at the top front face. This surface must be facing the front of the instrument (where the lid button is located) when inserted properly into the cuvette holder. After insertion, the constructed/customised standard operating procedure measurement is run on the sample for data analysis and processing.

3.4.3 Standard Operating Procedure (SOP) Measurement

Since we are performing repeated size measurements on the same type of samples (9 PAW samples: 3 sets of 3), it would be very tedious to set the parameters needed for every run every single time (especially if those parameters are identical for all samples). Furthermore, doing so raises the risk of introducing errors into the settings. Therefore, in order to avoid these errors and keep all measurements consistent between one another, SOP measurements are used with pre-set parameters.

The measurement type selected is called *Size* with a default instrument configuration, since the Zetasizer ZS is already connected during the SOP creation. Then, the selected material chosen will describe the analyte (dispersed particles) through its refractive index and absorption coefficient. As discussed previously the refractive index is necessary for the conversion of intensity distributions to volume distributions. Because we suspect that the majority of formed copper nanoparticles have been oxidized, then the refractive index and absorption coefficient of copper oxide nanoparticles have been considered. Essentially, the absorption coefficients of copper nanoparticles and copper oxide nanoparticles are identical (0.1), however, their refractive indices are ~ 0.210 and ~ 1.6, respectively[64]. On the other hand, the refractive index of copper oxide nanoparticles was deduced using the correlation developed by Dhineshbabu *et al.*[64] assuming a standard HeNe gas laser wavelength of 632.8 nm and a beam diameter of 0.63 mm at room temperature. (The Malvern Zetasizer ZS has the option of two monochromatic lasers: the first being the HeNe laser and the second a green frequency doubled DPSS with a wavelength of 532 nm; only the former is used during PSA.)) Thus, 0.1 and 1.6 have been selected as the absorption coefficient and refractive index, respectively. The effect of altering the refractive index is assessed in the next section. Next, the sample dispersant is identified as water at 25 ^oC with a viscosity of 0.8872 cP and a refractive index of 1.330. It is important to note that the instrument considers that the sample viscosity is identical to that of the dispersant by default, unless manually prompted otherwise. Altering this assumption is futile in our case since we have very low concentrations of copper oxide nanoparticles to begin with, so the assumption is valid.[63] In addition to viscosity, the sample temperature is also assumed to be identical to that of the dispersant set at 25 ^oC with an equilibrium time of 2 min. The equilibrium time adds a delay before the start of each measurement to ensure that the sample temperature is equal to the cell area temperature. Allowing temperature equilibrium guarantees that Brownian motion is measured and not convective motion due to temperature gradients.[63] Confirming the sufficiency of the equilibrium time specified is constantly monitored throughout the entire experimentation process by comparing the first result of a series of repeated measurements to the rest. If this result is different, then the equilibrium time is increased accordingly.

After selecting the correct cell type (ZEN0040), the measurement specifications are to be identified. The measurement angle is set to a 173° backscatter with a manually chosen measurement duration of 30 runs set at 10 s per run. The number of measurements is set to 3 with a delay of 10 s between measurements. In order to avoid confusion between individual recordings and final average recordings, only the final reports of the instrument after the final measurement are printed out. Those final reports include: the actual intensity distribution (M), the intensity peak statistics (M), the intensity peak PSD (M), the number PSD (M), the number statistics table (M), a size quality report (M), a size trend (M), a volume PSD (M), a volume statistics table (M), a Z-Ave trend (M), and lastly a Z-Avg trend (M). At the end, the results are exported with a frequency distribution template.

This sums up all the settings that need to be adjusted for this customized SOP measurement. All other parameters that have not been mentioned in this section are left at their default settings (such as general options, data processing, advanced and instructions tabs).

3.5 Other Characterization Techniques

In addition to all the analytical techniques used in this investigation, the ICP-OES was also used as a method of analyzing the total copper content of PAW. TEM was then used to characterize and study the different sizes of the copper/copper oxide nanoparticles. And finally, SEM was employed to justify and convey the presence of erosion at the electrode pin surface. Energy-Dispersive X-ray Spectroscopy (EDS) was also used to characterize electrode surfaces before and after plasma treatment, in order to track the significant changes and possibly the material origin of eroded nanoparticles.

It is noted that these characterization techniques are not methodologically discussed because they follow standard operating procedures that are generally applied in every analytical scenario. Processing the data obtained from all these techniques is discussed in the next section.

4 Results and Discussion

4.1 Preface

In this section, we will observe, interpret and discuss the processed results/aftermath of activating water through the use of plasma. The transfer of metallic content via erosion is firstly validated using SEM imaging. Then the copper ion analysis is interpreted and compared to the total copper content founded through ICP-OES. Once a ratio of ion:nanoparticle is established, then the nanoparticles are discussed from PSA-DLS and TEM data.

4.2 Copper Cathode Imaging: Visualizing Electrode Erosion and Morphology

Observing cathodic erosion justifies the origins of metal deposition in PAW. Figure 27 captures SEM images of the copper pin cathode before and after plasma treatment for all three types of gases. Evidently, the cathode tip imaged pre and post plasma treatment is the end which has been cut by the wire cutter with a flush cut profile, and that which is placed above the water surface to ignite the plasma discharge. As flat as the wire cutter's profile may be, it is almost impossible to cut a cathode pin tip to yield a perfectly flat surface, especially if the pin is made out of pure copper (since copper is very malleable). The pre-treatment images seen in Figure 27 clearly exemplify this fact showing copper pin surfaces that have an irregular triangular prism-like shape. Nevertheless, the flush cut profile of the cutter used permits the surfaces to be as flat as possible, thus they are pondered to be mostly flat, in the end, rather than completely rough or amorphous. However, the surfaces for all gases (air, oxygen and argon) drastically change during plasma treatment.

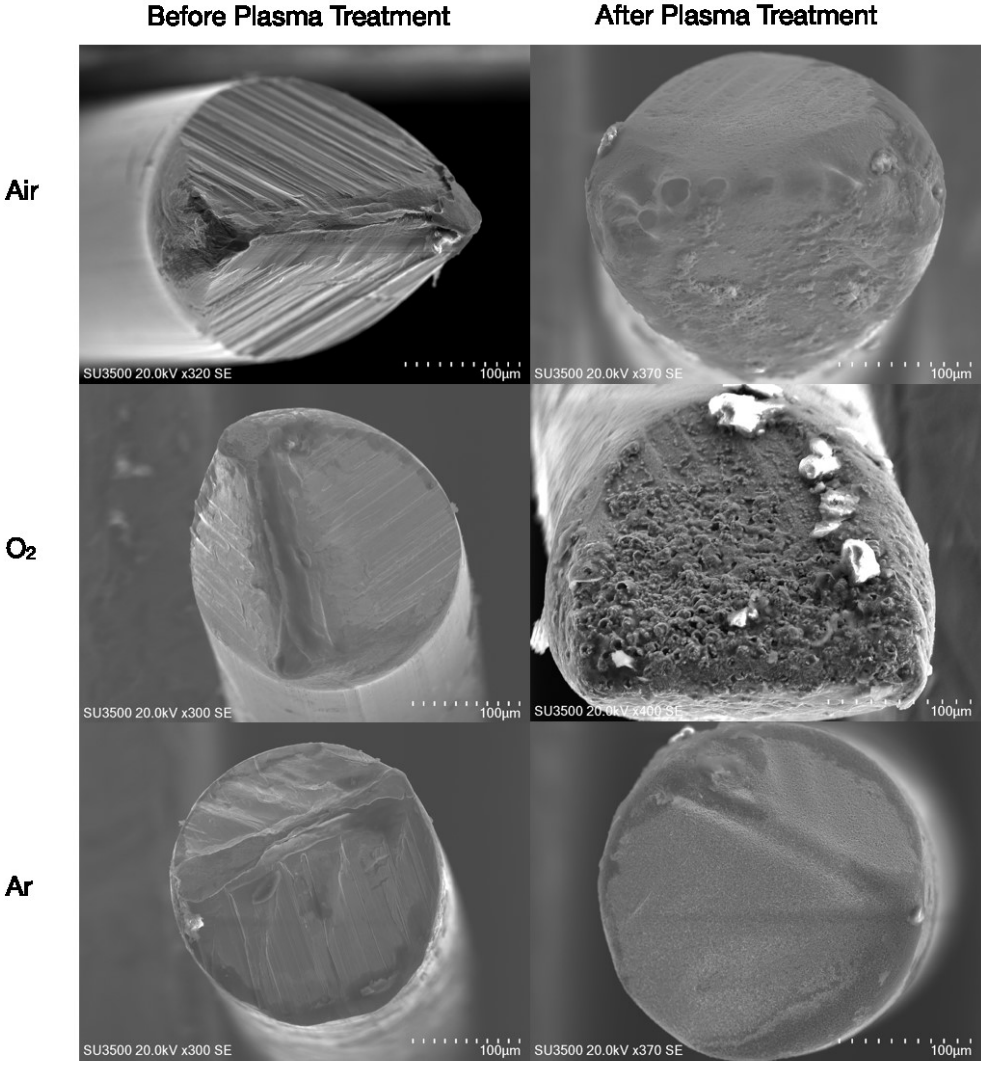

Figure 27: SEM images of the copper pin cathode tips pre and post plasma treatment for each type of gaseous atmosphere: air, oxygen and argon.

Figure 28 shows zoomed-in versions of the SEM images of the copper pin cathodes post-treatment for the three types of gaseous atmospheres along with an overall respective EDS analysis. It is important to note that the SEM images for Figure 28 are samples of many zoomed-in versions captured, and their EDS analyses represent what the majority of recordings look like. The selected images seen were considered the best-fit.

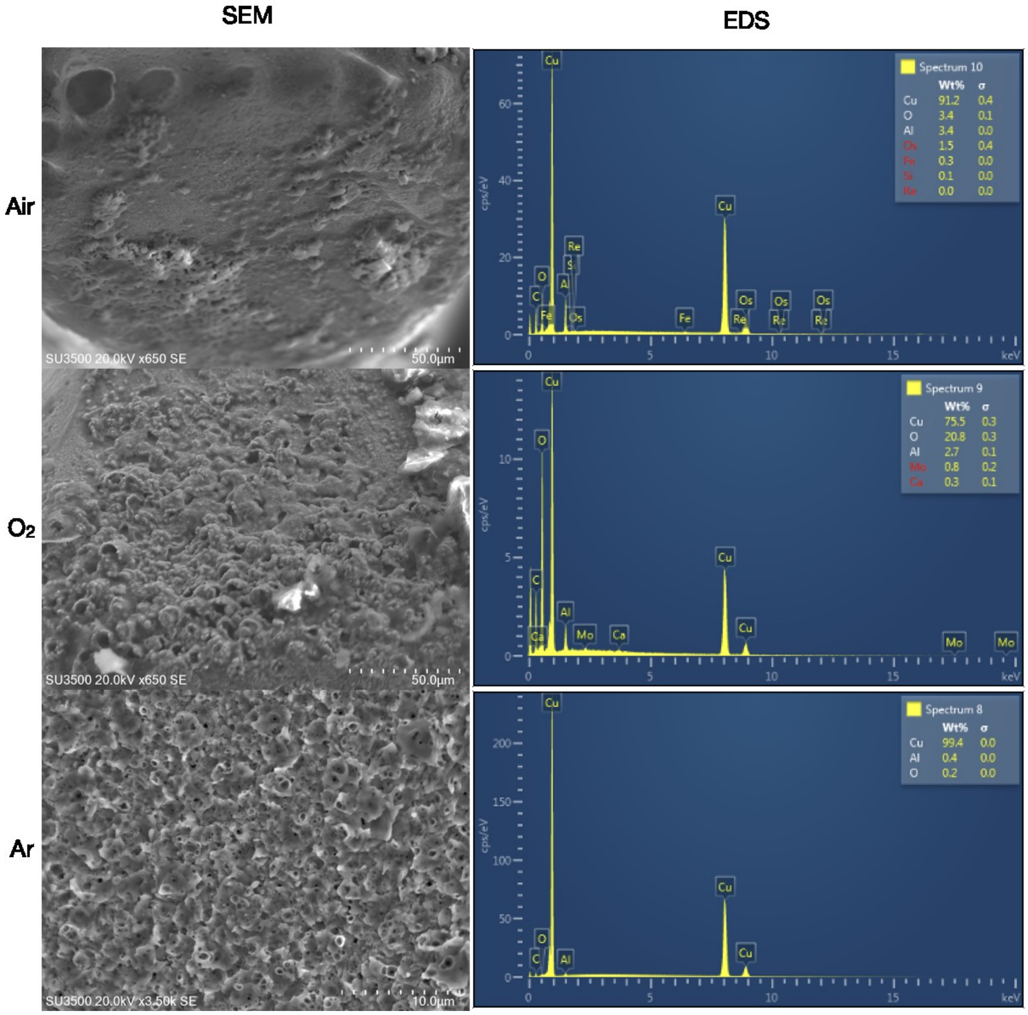

Figure 28: Zoomed-in versions of the SEM images captured in Figure 27 of the copper cathode pin post plasma treatment in air, oxygen and argon, along with an overall respective EDS analysis.

From both Figures 27 and 28, a crater-like morphology is deduced for all three gas types. In the case of air, relatively large craters with diameters between 10 to 20 µm are seen at the edges of the pin. Conversely, some areas are smooth with no craters and some show the formation of edged crystal structures. Thus, the surface is said to be largely heterogeneous. Its corresponding EDS analysis confirms an overall 91.2 % of copper and a low 3.4 % of oxygen. Unlike air, the post-plasma treatment with oxygen shows a less heterogenous surface with more evenly distributed small sized craters between 1 and 7 μm. Large bright crystal aggregates can be seen in the midst of the craters but mostly at the edges of the pin. Compared to air, the EDS analysis with oxygen exhibits lower levels of copper at 75.5 % and much higher levels of oxygen at 20.8 %. Finally, argon is deemed to lead to the most homogenous surface with relatively small perfectly distributed craters on the order of 1 μm or less. No smooth or crystallized areas are seen, and the EDS analysis shows 99.4 % of copper with a minimal 0.2 % of oxygen. [As a side note, the detected aluminum peaks seen in all the EDS analyses in Figure 28 are ignored and classified as either instrumental misinterpretations or impurities originating from alumina located in aerosol dust particles found in the laboratory atmosphere and caused by other non-related experiments.]

In general (for all three gas atmospheres), the formed craters seen are indeed due to erosion. As mentioned in the literature review, the cause and mechanism of erosion in non-thermal plasmas has been scarcely studied, however, the erosion of copper in this scenario can be hypothesized to be caused predominantly as a result of copper's non-refractory properties. Assuming thermionic and thermo-field emissions are not present in this plasma system, secondary electrons and copper cations can still arise from the bombardment of primary cations onto the cathode (even if copper has a relatively high work function). On the other hand, if we assume that the full amount of current flows through each crater, then we have cathode spot formation that, in fact, creates these craters as a result of thermo-field emission. In any case, it safe to conclude that erosion and metal deposition into PAW is primarily in the form of solid particles and not ions. Interestingly, prior to nanoparticle formation, liquid metal volumes are initially formed under the cathode and expelled as solids while the spot dies.[26] Hence, the copper ion:nanoparticle ratio is predicted to be less than 1. Shifts in ion concentration between different gaseous environments will thus be dependent on the activated chemistry taking place (produced RONS), and depending on how well the activated species can dissolve copper nanoparticles.

Plasma treatment with air has resulted in the most heterogeneously morphed copper pin surface because the cathode simply cannot withstand the combination of high electrical and chemical environments it is subjected to. From the high acidic medium generated as a result of the formed nitrates combined with the high voltage discharges, relatively large chunks of the copper pin erode or fall off into the water leaving areas where craters may have been present, to become smooth. The small crystal aggregates (~ 10 μm) formed can be surmised to be copper oxide crystals for two main reasons: (1) the selective EDS analysis on each individual crystal show strong equivalent spike signals for copper and oxygen, and (2) the zoomed-in crystal images are not well visualized due to the high level of brightness generated, which indicates the presence of non-conductive areas, for copper oxides are known to be poor conductors. In the case of oxygen, the electrode is able to tolerate the plasma discharge environment more than in air, probably because there is a lower diversity of chemically activated species (only reactive oxygen species (ROS) are present) and so the acidity level is decreased (pH levels of PAW in air and oxygen are approximately 2.3 and 4.5 respectively). Nevertheless, a significant amount of erosion is observed due to the electrical and thermal properties induced in the system (as previously discussed). As with air, the large formed crystals are classified as copper oxides, however, higher levels of oxygen are recorded by EDS, which makes intuitive sense. The levels of oxygen in air are lower than those in pure oxygen gas, so the formation of nanosized or microsized copper oxide crystals on the cathode surface is abundant, increasing the overall levels of oxygen recorded by EDS as seen in Figure 28 as well as the size of crystals (which are between 30 and 40 μm). Furthermore, the non-conductive intense brightness emitted from these crystals further justifies their existence as copper oxides (selective EDS analyses of these crystals were performed as proof similar to those performed for air). Finally, in the case of argon the smallest craters are seen with no smooth or crystal edged surfaces and an EDS recording of 99.4 % pure copper. This makes sense because almost no RONS are present to accompany the electrical settings applied on the cathode (pH of PAW in argon is ~ 5.5). Thus, the copper cathode can withstand plasma discharges and remain most stable with the highest electrode lifetime in an argon atmosphere. Moreover, it can be said that the use of argon may depict the levels of erosion due to electrical and thermal properties of the plasma solely, without the interference of RONS. However, that would not be entirely true since some ROS can originate from the evaporation of water and its propagation into the plasma atmosphere/channel.

Therefore, in terms of plasma atmosphere, one can infer that the levels of copper erosion during the production of PAW in decreasing order is: air > oxygen > argon. In turn, this means that the total copper content in PAW abides by the same trend. Since the electrical configuration is the same for all three gasses, this means that this trend is dependent on the reactive species generated and the resulting pH. Because a decrease in pH causes an increase in ion content, one may predict and conclude that the ion:nanoparticle ratio also follows this aforementioned trend. The results in the next section for total copper content obtained from ICP-OES validate this conclusion.

4.3 Copper Content Results in PAW

4.3.1 Copper Ion Content in PAW in an Air Atmosphere

Using the external standards method, a calibration curve is constructed by taking the average stripping current peak values of three trials of DPASV analysis per standard and plotting them against their corresponding concentrations. The list of standards is mentioned previously in the experimentation chapter. Primarily though, for the average stripping current peak to be located and determined accurately, the average stripping current recordings were plotted individually against the applied potential. Figure 29 shows an overlaid plot of all the average stripping currents vs. applied potential graphs for each copper standard as a result of DPASV analysis.

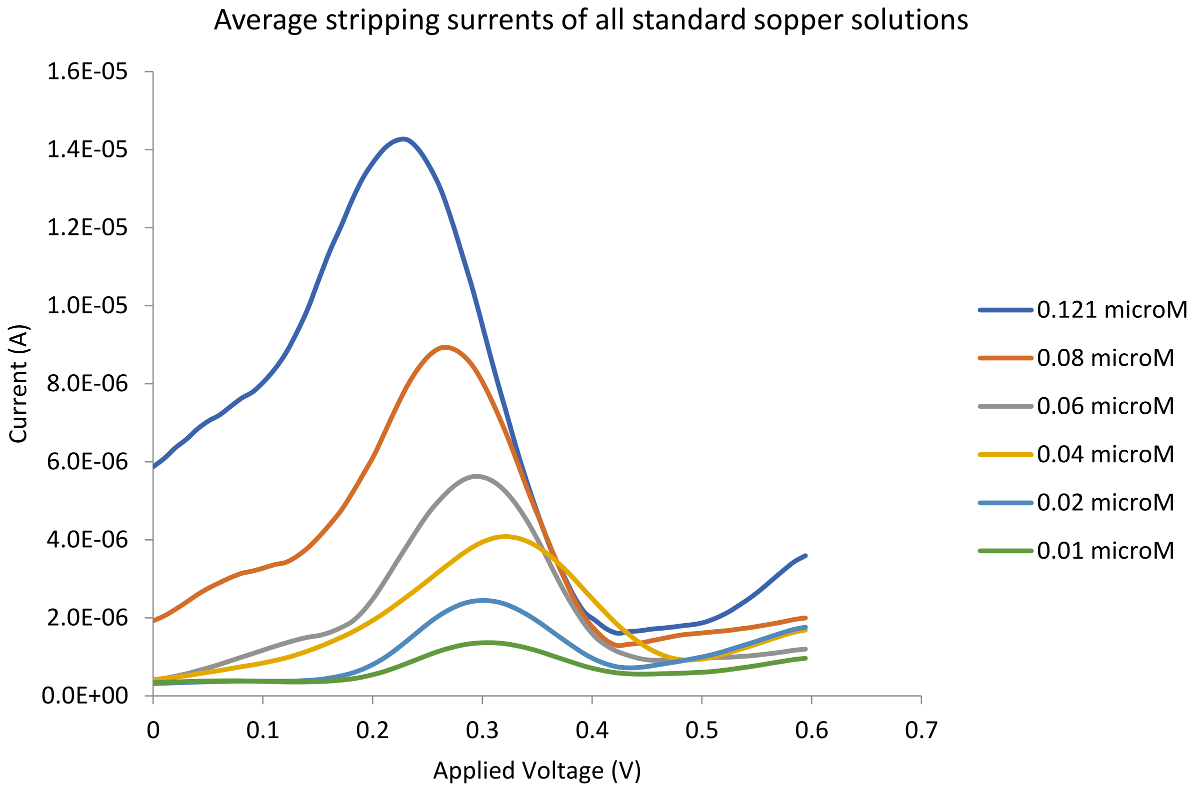

Figure 29: The overlaid plots of all the average stripping currents of the copper standards; obtained from DPASV analysis.

As seen, the oxidation/stripping voltage seems to vary, gradually increasing from ~ 0.25 to ~ 0.30 V as the concentration decreases from 0.121 to 0.01 µM with the exception of 0.04 µM. The reason for this trend is unclear, but according to a study performed by Huangxian Ju *et al.*[65], one can surmise that the slight increase in potential is due to the low mobility of cupric ions in a very dilute medium. The principle behind it is explained using electric forces based on the Debye-Hückel theory (as referred to in the article)[65]. Therefore, one can hypothesize that in order to compensate for this voltage shift phenomenon, the cupric ions must be given more mobility to diffuse more properly towards and away from the gold electrode. Examples of attaining greater mobility would include either stirring the solution or rotating the electrode. Perhaps this modification can be applied into the future work concerning this project as will be discussed in the next chapter. Regardless, this systematic error can also be considered to be trivial as we are not very interested at the end about the oxidation voltage as much as the stripping current peak. If voltage shifts do not affect the height of the current peaks, then this error may as well be ignored. Nevertheless, this suspected correlation between voltage shifts and stripping current peaks must be investigated in the future to prove that it does not exist and justify its neglection in error propagation.

From the differences in peak heights between different standard concentrations, Figure 29 can allow the experimenter to visualize the linearity between the stripping current and concentration, as described by equation (9). The calibration curve constructed in Figure 30 from Figure 29 asserts their direct proportionality (linear correlation) qualitatively and quantitatively with a correlation coefficient (R^2) of 0.994.

Even though the calibration curve's best fit line does not pass through every single data point, it is within the range of each point's standard deviation (error bars). Moreover, the range of standard deviations for each point is relatively small, especially towards lower concentrations, which indicates overall high levels of precision. One probable reason behind larger error bars at higher concentrations is due to the higher probability of forming multilayers of copper at the active surface rather than just a monolayer. Multilayers will increase the layer thickness, which will increase the value of the peak stripping current according to equation (9) and decrease precision.

With the calibration curve attained, now the air-PAW samples can be analyzed as well and interpolated into the calibration plot. For proper reliable analysis, three different air-PAW samples were prepared and analyzed each three times via DPASV. It is important to note that sample preparation and analysis take place within the same day with no long hiatus between repetitions

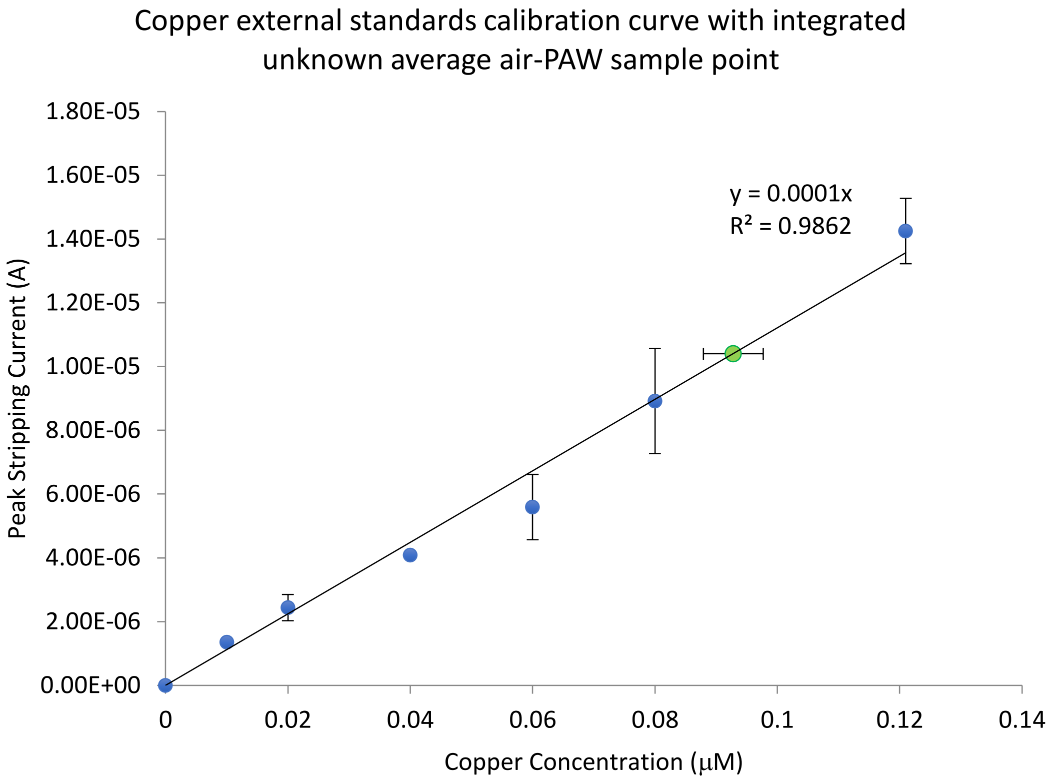

Figure 30: Calibration Curve based on the results from Figure 29. Showing the best fit linear trend line correlation between stripping current peaks and concentration (Error bars are included). The blue dots represent standard solutions and the green dot represents the average value of all analyzed air-PAW samples with horizontal error bars. It is important to note that the green dot does not contribute to the trend line.

such that sample storage is required. The reason this is done is to avoid cupric ion concentrations from inflating with time due to copper nanoparticle dissolution. However, this is only a presumption, as air-PAW samples have shown consistent DPASV recordings in the duration of a week for the same sample (PAW samples were stored in a fridge at 4 ºC). Figure 31 shows the average DPASV overlaid results for all three air-PAW samples as well as the average of all three different averages. This latter result's stripping current peak is the final peak result that is integrated into the calibration plot in order to determine the unknown cupric concentration of air-PAW.

From the total average stripping current graphed in Figure 31, the current peak was determined to be ~ 1.04 x 10^{-5} A with a standard deviation of 3.45 x 10^{-7} A. When this value is interpolated into the calibration curve in Figure 30, the unknown concentration for air-PAW is determined to be 0.0928 µM with the following statistical survey: an error of 0.0098 µM (which represents the horizontal error bar seen in Figure 30), a SNR of 19.2810, a coefficient of variance (CoV) equal to 5.19 %, a limit of detection (LOD) or DL equal to 2.5 nM, an LOQ of 8.2 nM, a slope or calibration sensitivity of 10^{-4} A/µM, a slope error of ~ 0 A/µM, an intercept of 0 A with an intercept error of 0 A and a correlation coefficient of ~ 0.9863. This statistical survey was run using the MATLAB code found in the Appendix chapter.

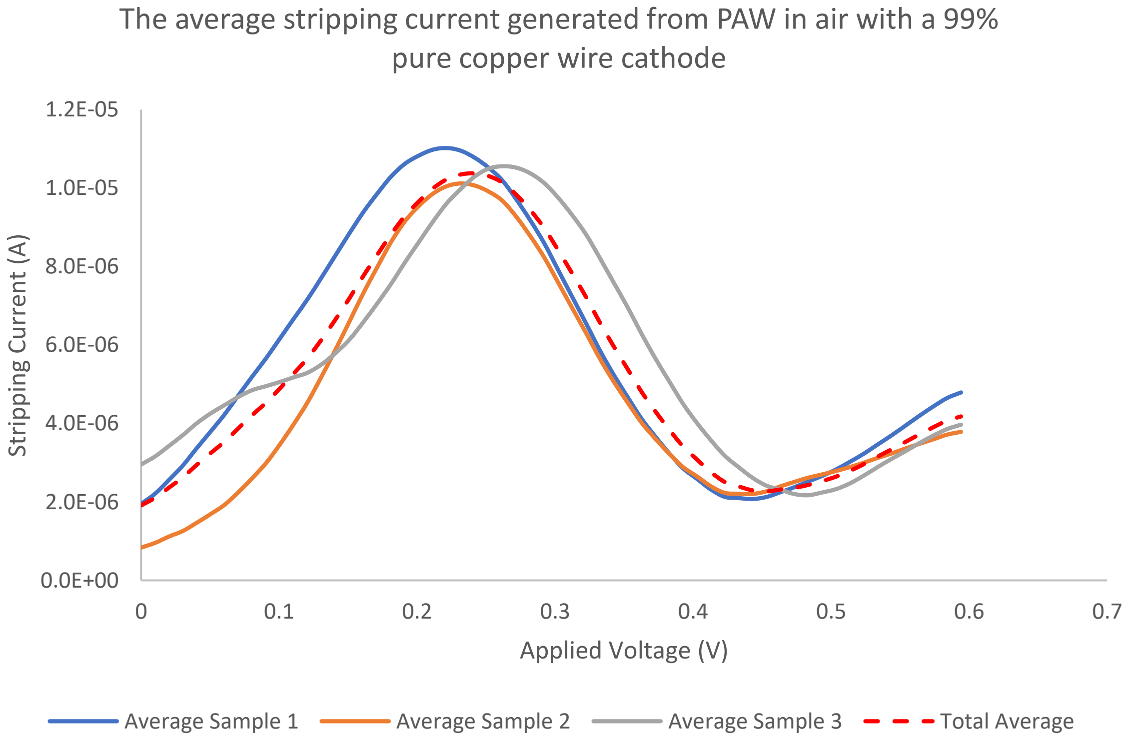

Figure 31: This is an overlaid plot of the average stripping currents of all three air-PAW samples as a result of DPASV analyses.

The statistical survey indicates a high level of precision for this analytical method since the SNR is relatively high and the CoV is low. In addition, the relative uncertainty is low at ~ 10.6 % due to a low value of horizontal error, which further proves excellent levels of precision. The DL and LOQ are at the nanomolar level, which validates the high level of sensitivity and low levels of background noise provided by DPASV analysis (relatively high SNR also implies low levels of background noise). Moreover, high sensitivity is justified since the slope is 10 times larger in magnitude than the LOL. An analytical sensitivity (γ) can also be tabulated by dividing the calibration sensitivity with the lowest vertical error possibly recorded from the pool of standard solutions (which is 2.39×10^{-8} μM at a standard concentration of 0.01 μM). That value is ~ 4184 μM, which indicates great specific sensitivity. γ is not affected by small changes to the instrumental settings but varies with concentration. This means that it gives a value of sensitivity to a specific concentration. Since the highest standard deviation of the standard solutions is 1.65×10^{-6} μM at 0.08 μM then the range of γ for this DPASV analysis is between 60.6 to 4184 μM, which is very high and desirable. In conclusion, this statistical survey shows us how reliable the obtained copper concentration value in air-PAW is, as well as how adequate the methodology can be.

4.3.2 Comparisons to Total Copper Content Results obtained via ICP-OES

In order to deduce the copper ion:nanoparticle ratio in air-PAW we must compare the electrochemical results with those obtained from ICP analyses. Figure 32 shows the results of total copper content analysis via ICP-OES for PAW in air and oxygen only at different plasma treatment times (due to time constraints and instrumental complications, the analyses for argon were not performed). Two versions of the same plot are observed: one that shows the result of each trial at every plasma treatment interval (4 trials/PAW samples per plasma treatment interval) and the other shows the average values of all samples at each specific treatment time with added error bars.

Different plasma treatment times were considered for these analyses to ensure that the error bars overlap. Overlapping error bars indicate that the total copper content is not heavily dependent on plasma treatment time. Of course minimally and maximally exaggerated plasma treatment times, such as 1 and 60 min respectively, will intuitively have significantly different total copper content values as the former will allow almost no time for sufficient copper erosion while the latter would have almost completely deteriorated and deposited a large section of the electrode into the PAW. However, copper contents between 10 and 30 min of plasma treatment time does not lead to sufficient evidence to justify significant differences in values. All these stated assumptions are based on studies performed by E. Corella Puertas *et al.*[3].

From Figure 32, one can approximate that the total copper contents in air-PAW and oxygen-PAW both treated for 20 min are ~ 1.00 and ~ 0.12 mg/L, respectively. These results are consistent with the conclusion and trend made in the erosion and morphology section. Overall copper content is indeed much higher in an air plasma than in an oxygen plasma at a treatment time of 20 min. Argon can be inferred to be even lower than oxygen since the trend has been validated.

Now, to compare the total copper content to the copper ion content in air-PAW, a quick conversion of units must be done. A cupric concentration of 1.00 mg/L is equivalent to a concentration of 15.736 μM. Because the total copper content is much larger than the ionic content, then the copper nanoparticle content can be said to be approximately represented by the total copper content (as it is evidently more dominant than ionic content). Therefore, the copper ion:nanoparticle ratio is ~ 0.00590 (0.0928 μM/15.736 μM) validating our hypothesis that the ratio is much less than 1 (nanoparticle content dominates over ionic content). Furthermore, with future work on the construction of the calibration curves for oxygen-PAW and argon-PAW, the ion:nanoparticle ratio trend can also be validated. Its validation is hypothesized only on the premise that the trend for total copper content was proven.

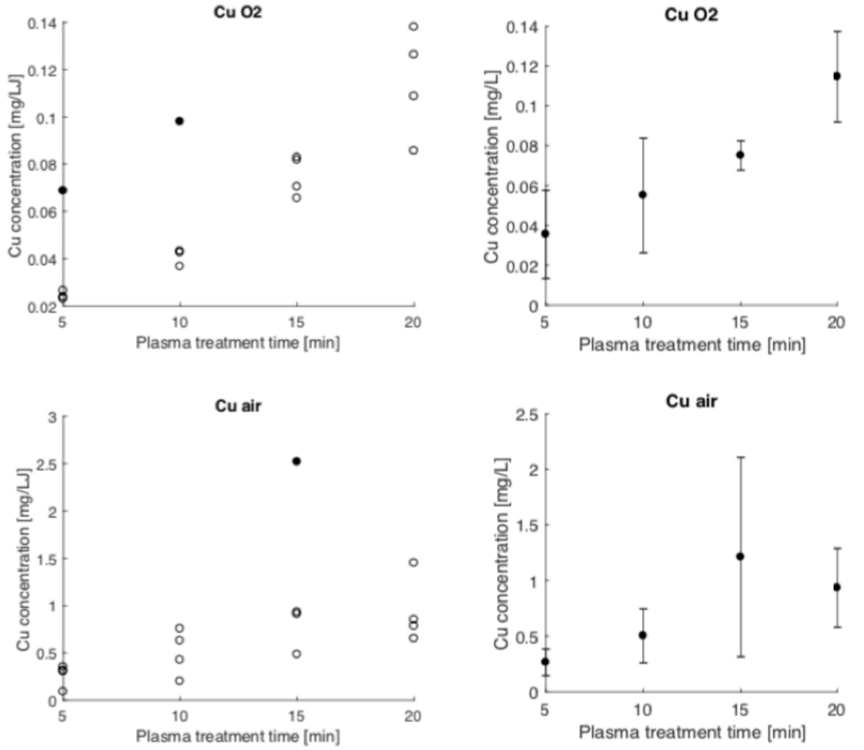

Figure 32: Results of the total copper content in air-PAW and oxygen-PAW obtained via ICP-OES. The top row represents oxygen and the bottom air. The left column shows the results for every PAW sample at each respective treatment time (4 different samples per treatment time); black circles represent outliers and white circles represent valid trials. The right column shows the average results of all valid samples for each treatment time, with added error bars.

4.4 Copper Nanoparticle Analysis Results

4.4.1 PSA-DLS Data Results: Size Distribution Analysis of Copper Nanoparticles in PAW

Particle size distributions measured by DLS of copper nanoparticles present in PAW as a result of plasma treatment in a Cu-Ar environment are all shown in Figure 33 for both volume-based (left column) and intensity-based (right column) distributions. As mentioned previously, the measurements were done on three different samples and were repeated three times for each sample.

When comparing both types of distributions for all trials, run 3 is almost identical for every trial with a peak that is always seen at ~ 900 nm.

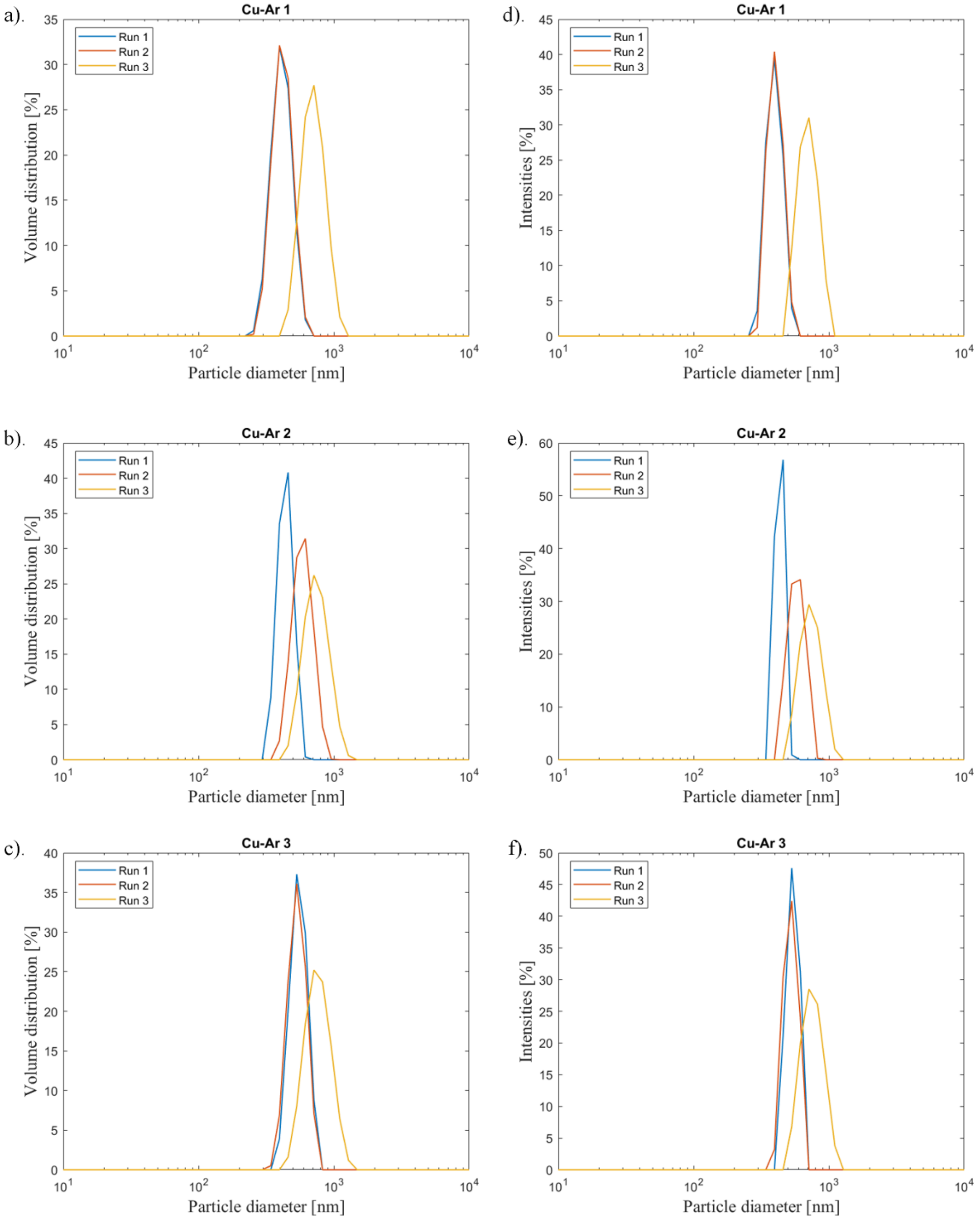

Figure 33: Particle size distribution of copper nanoparticles in 3 different argon-PAW samples based on percentage volume (a-c) and percentage intensity (d-f).

This peak also always has the smallest mean percentage volume/intensity distribution, the highest mean particle diameter and the broadest FWHM out of the three runs for each trial. This replicable/reoccurring observation is probably due to copper nanoparticle agglomeration with time (from run 1 to 3). The mean particle diameter increases over time, because the smaller nanoparticles agglomerate to form larger nanoparticles with a wider range of diameters. This wide range causes the polydispersity to increase with time, which broadens the FWHM and thus logically decreases the mean percentage volume/intensity (since a wide range of diameters are now distributed within the light column volume). With that, we can infer that runs 1 and 2 generally have a larger mean percentage volume/intensity with a narrower FWHM and a smaller mean particle diameter because the majority of nanoparticles are more monodisperse and have not agglomerated yet. The averages of the mean particle diameters are tabulated to be approximately 669, 652 and 681 nm for samples 1, 2 and 3, respectively. They are indeed very similar.

Figure 34 shows analogous results to Figure 33 but rather for air-PAW. Unlike argon-PAW, the distribution data in air-PAW is inconsistent between different samples. Furthermore, all nanoparticle suspension signals observed below 10 nm did not scatter light at 10 kcps in excess to the light scattered by the water dispersant. Thus, the DL of the instrument is breached, and these signals are deemed unreliable and hence ignored (as discussed in the previous chapter). The inconsistencies in readings between samples is due to the fact that air-PAW is a very reactive medium with much higher levels of acidity and a high concentration of RONS compared to argon-PAW. With high reactivity, the type of erosion of nanoparticles will thus be very variable between one sample and the other. It is important to note that the level of erosion/metal deposition is overall consistent according to ICP-OES measurements. Here, rather, we imply that the pieces of eroded cathode are variable, meaning that the nanoparticle deposition in particular (**not the ionic deposition**) will vary in nanoparticle size distributions for every treatment, but the overall particle mass is the same. This inference complements the SEM morphology analyses, since the erosion in air seems to be random with random chunks of the cathode falling off, whereas the erosion in argon is very uniform and structured with an organized array of craters; indicating that distribution of nanoparticles in air-PAW is expected to be random for every trial as well, while that of argon should be very consistent between samples (as proven in Figure 33). The averages of mean particle diameters were found to be 101, 309 and 187 nm for samples 1, 2 and 3, respectively.

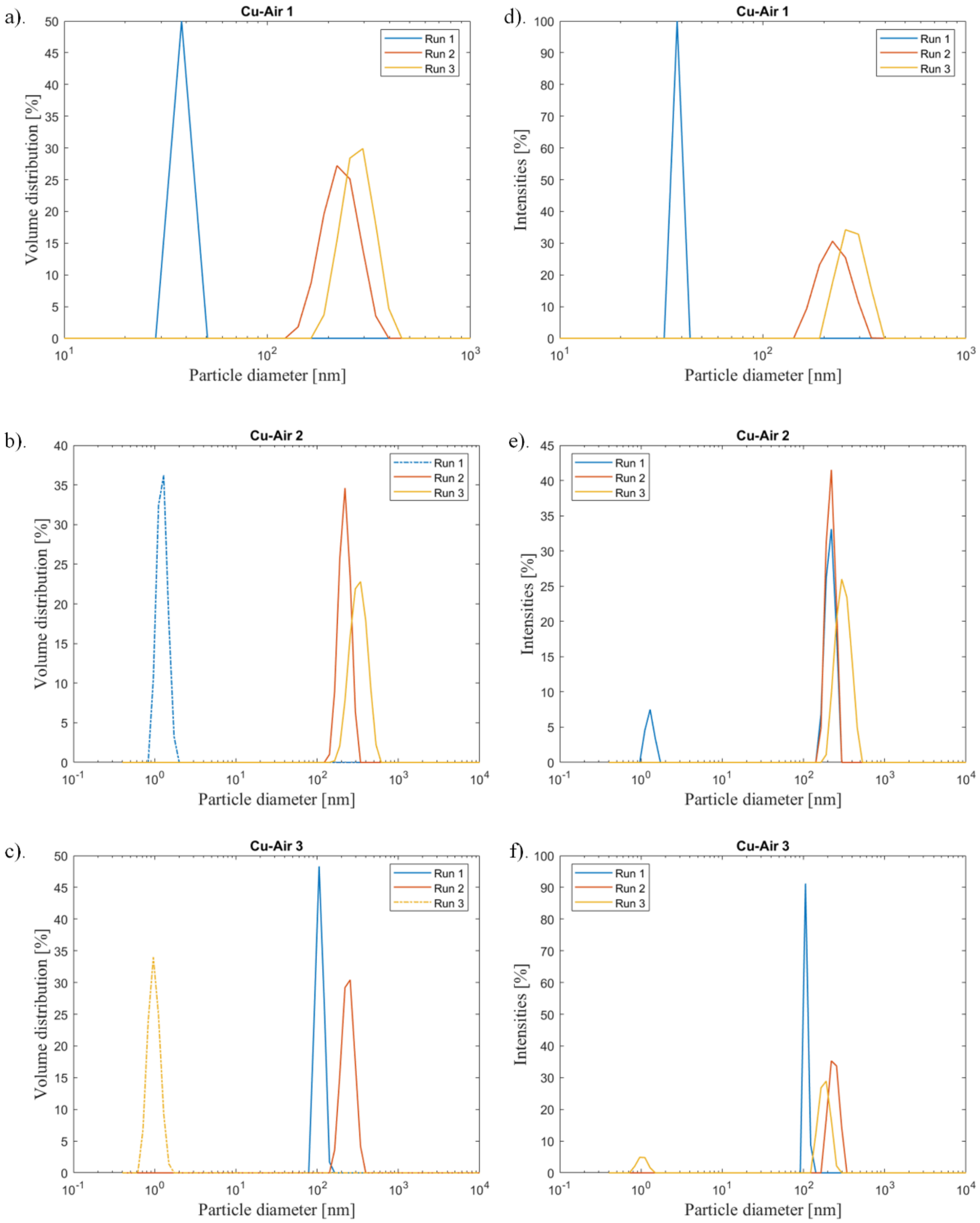

Figure 34: Particle size distribution of copper nanoparticles in 3 different air-PAW samples based on percentage volume (a-c) and percentage intensity (d-f). Signals below 10 nm were ignored.

Agglomeration in air-PAW can also be interpreted since the mean particle diameter increases gradually from run 1 to run 3 in samples 1 and 2. Sample 3, however, does not abide by this gradual increase for either type of distribution. This can be due to high sedimentation kinetics of sample 3's air-PAW suspension. High sedimentation kinetics leads to large agglomerates settling at the bottom of the cuvette, leaving only small sized nanoparticles (in the case of % intensity of sample 3) or even no nanoparticles (in the case of % volume of sample 3) in the DLS detection zone of the cuvette. This explains why the 3rd run of sample 3 for both distributions violate the increasing mean particle diameter agglomeration trend. Moreover, one may notice that the volume and intensity distributions in sample 2 run 1 are inconsistent. This is because the intensity distribution is showing bimodal behaviour which reduced into one peak in the volume distribution that is deemed unreliable. The inaccuracy would not have been detected in the intensity distribution, which highlights one of the many advantages of converting intensity distributions to volume ones. To clarify, sample scattering intensity is proportional to the square of the nanoparticle's radius.[63] As a consequence, a small number of large particles can appear to dominate the DLS measured intensity distribution. The derived volume distributions, however, are skewed towards smaller sizes, taking into account the mass compositions of the sample.[63]

Lastly, Figure 35 shows the analogous PSA-DLS data for oxygen-PAW. Like argon-PAW, the data for oxygen-PAW is very consistent between samples. From an erosion point of view this makes a lot of sense as the reactive medium of oxygen-PAW is not as hostile as air-PAW (only ROS are present with a pH of 4.5) and so the erosion has a lower level of randomness and a higher level of structure compared to erosion during the production of air-PAW. The discussed agglomeration trend is also demonstrated consistently for all samples and is identical to the trend seen with argon-PAW. The explanation is thus exactly the same. The only main difference between the argon-PAW data and the oxygen-PAW data is that the third run for every sample in argon-PAW are almost perfectly identical, which indicated universal uniformity and is heavily implied from its respective argon-PAW cathode erosion SEM image. With oxygen-PAW, run 3 of sample 2 is much broader than the third runs of samples 1 and 3.

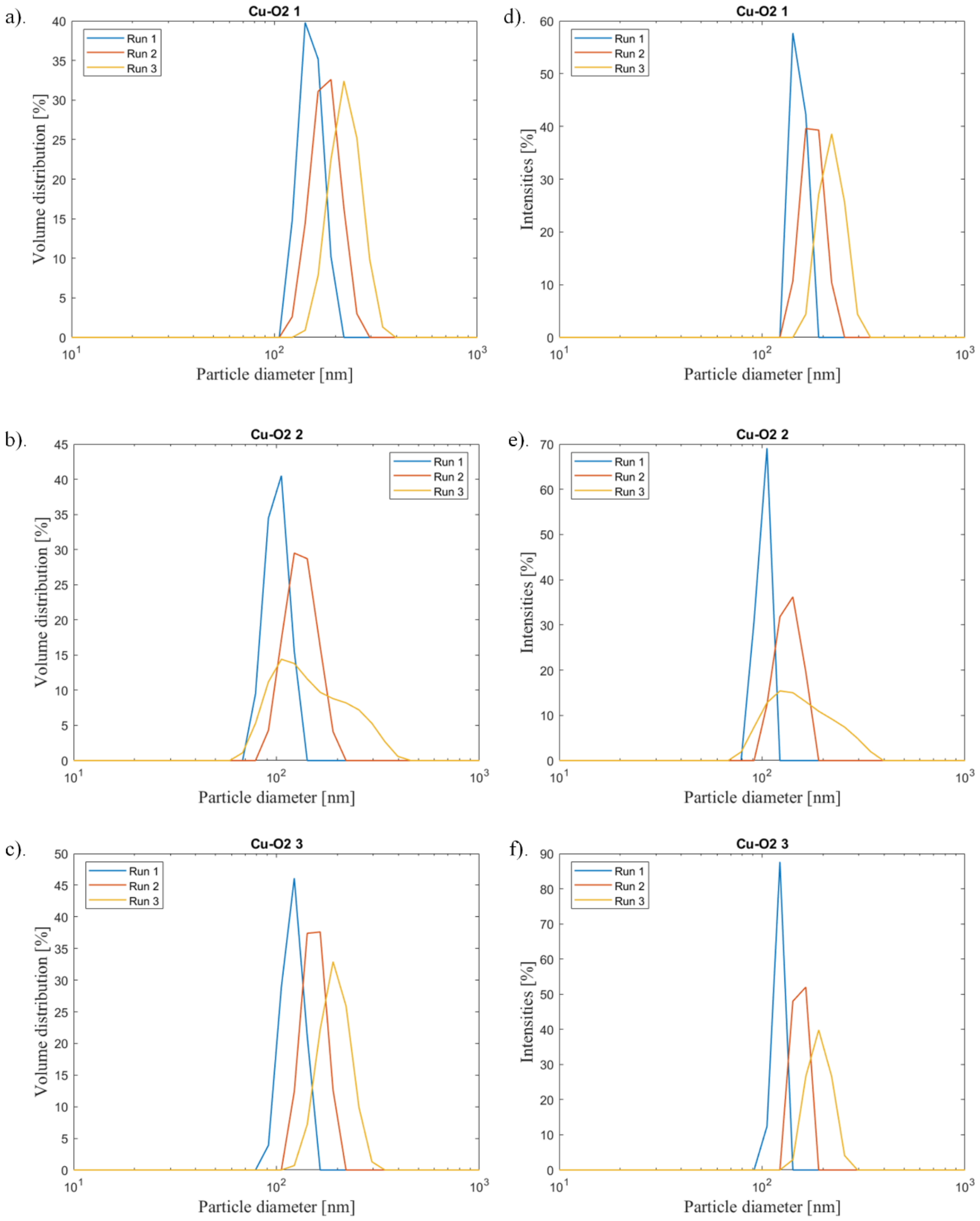

Figure 35: Particle size distribution of copper nanoparticles in 3 different oxygen-PAW samples based on percentage volume (a-c) and percentage intensity (d-f).

This difference in polydispersity is due to the low levels of randomness in erosion when making oxygen-PAW that, nevertheless, still have an effect on the randomness of nanoparticle sizes but not at the same magnitude as with air-PAW. The average mean particle diameters are 200, 168 and 167 nm for samples 1, 2 and 3, respectively, and are indeed similar.

In conclusion, it seems that argon-PAW samples have the largest nanoparticle diameter sizes followed by oxygen-PAW and air-PAW being inconclusive. Figure 36 summarizes this conclusion by graphing the average Z-average diameters obtained for each type of gas. The Z-average is simply the mean diameter value from the intensity distributions derived from cumulant analysis.[63] The large error bar seen for air justifies why its analysis has been deemed inconclusive.

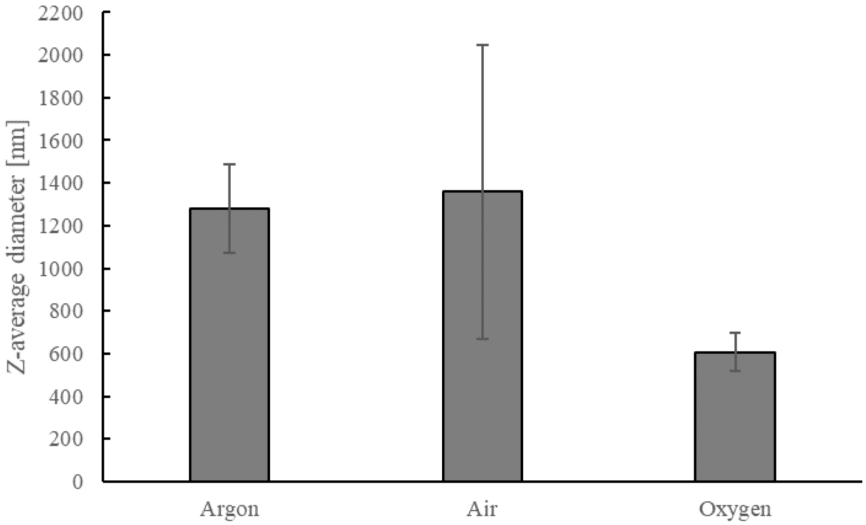

Figure 36: The averages of Z-average diameters of copper nanoparticles found in PAW for all three gases. The error bars are the standard deviation of the three Z-average diameters of each sample.

PDI average values will not be discussed further because they are insignificant to interpretations in this investigation. The PDI of copper nanoparticles in not dependent on the type of gaseous atmosphere used in plasma treatment but rather on agglomeration and perhaps on the type of metal being agglomerated. Since we are only using copper cathodes then further discussions on PDI is futile. The average PDI values for each gas can still be found in the Appendix chapter.

It is also beneficial to mention that the effect of suspension agitation and agglomeration over time on the nanoparticle sizes was also investigated by sonicating and storing these same samples in the fridge for one week and then running a PSA-DLS analysis on all of them once more. However, the results proved to be unfruitful since they were identical to the samples run immediately after plasma treatment. Regardless, this tells us that the nanoparticles are very stable and have a long life-time, as medium agitation and incubation time do not affect the magnitude or rate of nanoparticle agglomeration. Finally, as a reminder, all the PSA-DLS readings that were classified as reliable in this section (did not breach the DL of the instrument), respect the correlation depicted by Figure 26.

4.4.2 TEM Imaging of the Copper Nanoparticles

For TEM analysis, gold grids (*Ted Pella*, Ultrathin Carbon Film on Lacey Carbon Support Film, 300 mesh, Gold, 01824G) were used. Copper grids cannot be used in this scenario because the analyte is composed of copper, meaning that the copper mesh will interfere with the analysis. The grids were gently held using special EMS tweezers and locked using rubber o-rings. Then, four droplets of the PAW sample are dropped over the grids. The four droplets are not dropped all at once, as the grids are allowed to dry between each added droplet. This method ensures optimal retention of the copper nanoparticles by the mesh.

Figures 37 and 38 show TEM images of a copper nanoparticle found in argon-PAW and air-PAW respectively. Due to time constraints, TEM imaging for oxygen-PAW samples was not possible. In Figure 37, the top left TEM image captures the entirety of the nanoparticle (which is referred to as the final nanoparticle), while the rest focus on the agglomeration interfaces. The very bottom graph is an EDS analysis of the final nanoparticle. The presence of agglomeration interfaces justifies that the nanoparticle viewed was in fact the product of smaller nanoparticles agglomerating with one another. Whether agglomeration was interrupted or not is based on the size value obtained. According to the image scaling, the observed nanoparticle is ~ 260 nm.

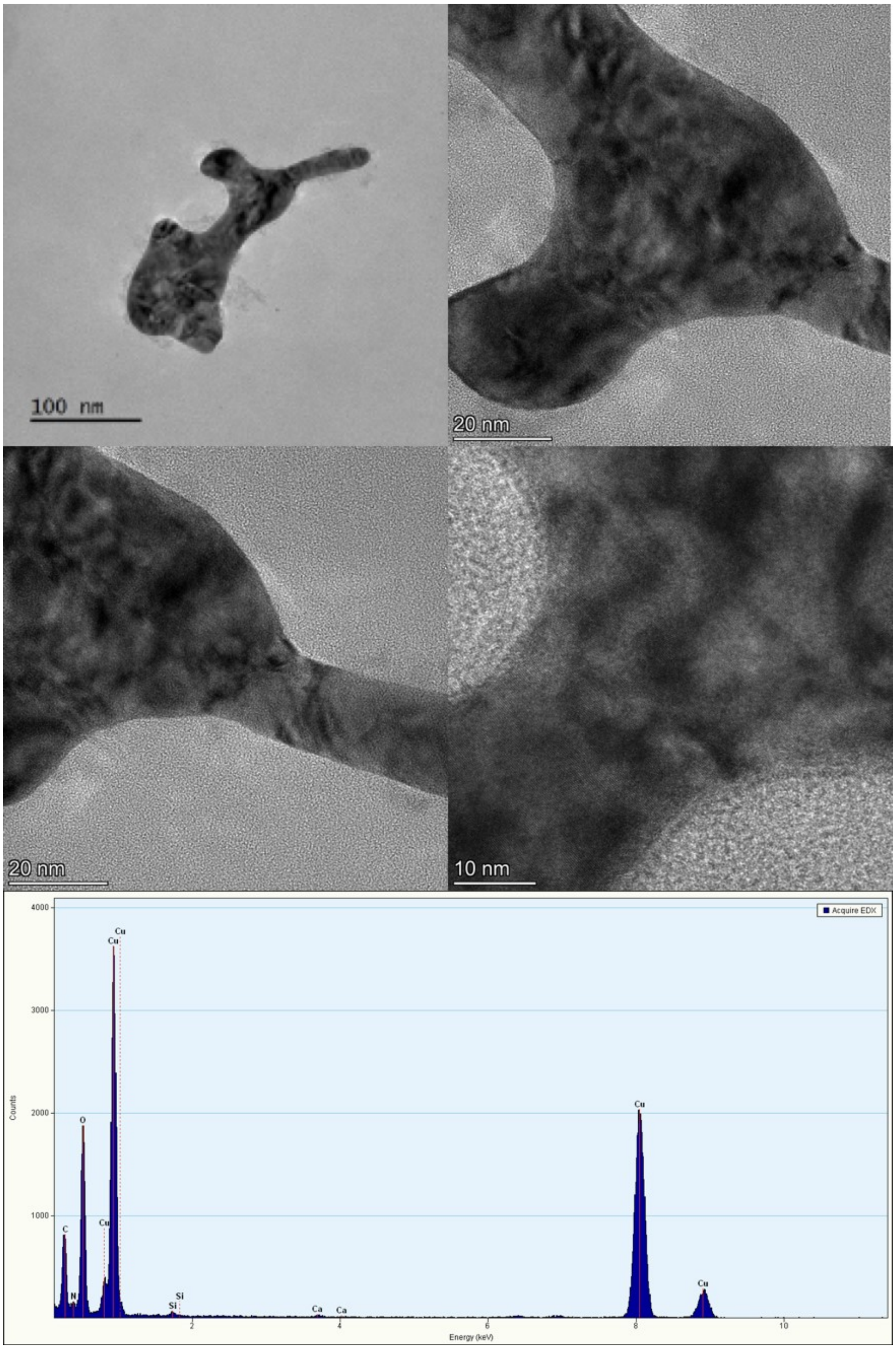

Figure 37: TEM images of the copper nanoparticles in an argon-PAW sample. Overall EDS analysis at the bottom.

Compared to the mean particle diameter values determined from PSA-DLS, this value lies towards the lower region of the diameter range found for argon-PAW. Therefore, one can infer that the agglomeration of this final nanoparticle is most probably incomplete. From the EDS analysis, one confirms high levels of copper at ~ 3800 counts and lower levels of oxygen at ~ 2000 counts. One can thus deduce that the final copper nanoparticle may be composed of either pure copper and/or copper oxide monomers. The copper oxide nanoparticle monomers simply originate from the oxidation of the pure copper nanoparticle monomers, which takes place during their flight from the tip of the cathode to the water interface. The oxidation is induced from the ROS in water and/or from the natural oxygen levels of RO water. Even though the levels of produced ROS in an argon plasma system are very minimal, this does not imply the inhibition/minimization of pure copper nanoparticle oxidation. However, since the copper levels are almost double the oxygen levels, this may mean that some pure copper nanoparticle monomers remain unoxidized within the final nanoparticle.

Compared to an argon-PAW copper nanoparticle, air-PAW copper nanoparticles are inferred to have higher level of copper oxide nanoparticle monomers, tending to the complete oxidation of pure copper. Indeed, this is the case as seen in Figure 38. As in Figure 37, the top left TEM image represents the final nanoparticle. The other images capture the crystal edges of the final nanoparticle. Agglomeration interfaces are not observed in these captures, but the crystal lattice structure is at much higher resolution than in Figure 37. The size of the particle is ~ 2850 nm or 2.85 μm, making the final nanoparticle in fact a final microparticle. This value is very inconsistent with PSA-DLS analysis of copper particles in air-PAW, which proves the inconclusive result previously reached. With particles at this size, sedimentation kinetics are bound to increase drastically within the PSA-DLS cell of an air-PAW sample and so particles of smaller sizes are detected instead (also previously discussed). The Z-average diameter graph in Figure 36 compliments this notion as the error bars for air reach ~ 2000 nm.

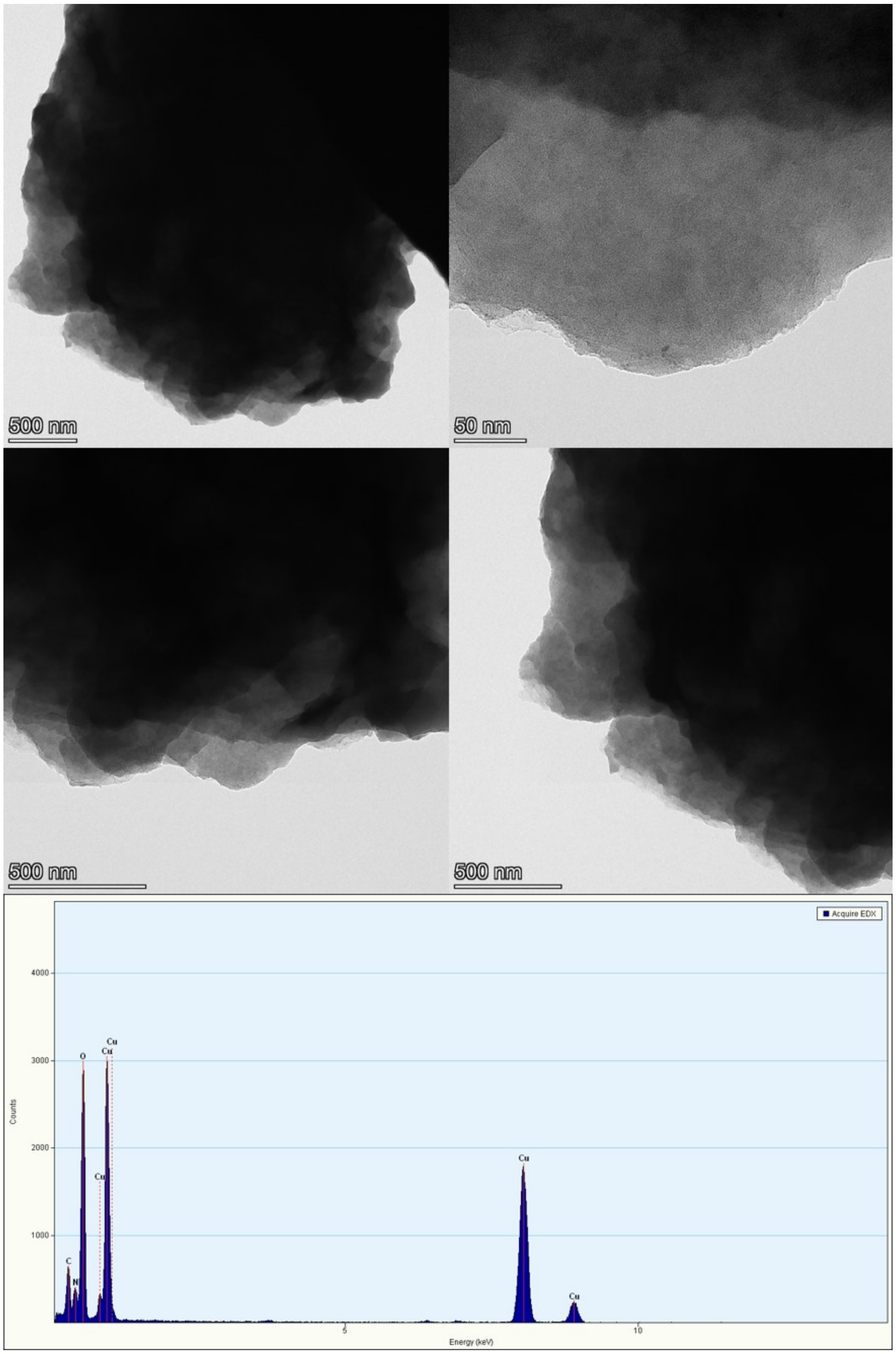

Figure 38: TEM images of the copper nanoparticles in an argon-PAW sample. Overall EDS analysis at the bottom.

Moving on, the EDS analysis shows almost equal/stoichiometric levels of oxygen and copper, which implies that the entire final particle has been completely oxidized, with the copper nanoparticle monomers entirely converted to copper oxide nanoparticle monomers.

As a final note, the carbon signals seen in both EDS analyses in Figures 37 and 38 come from the lacey carbon support film found on the gold grids and so are ignored. Furthermore, crystal lattice analysis is not performed in this investigation as it is considered irrelevant. However, crystal lattice diffractograms can be found in the Appendix chapter, and crystal lattice analysis using them is encouraged for a more complete characterization of the particles viewed.

5 Conclusion and Future Work

5.1 Conclusion and Ongoing Work

The study focused on the activation of water via plasma in air, oxygen and argon atmospheres has allowed us to solve some of the ambiguities involving erosion in non-thermal plasmas. The deposition of copper into PAW has determined that the integration of metal is of an ionic and nanoparticle form with an ion:nanoparticle ratio of 0.00590 in air-PAW. Using a properly optimized DPASV method, the cupric concentration in air-PAW is determined to be 0.0928 μM from the constructed calibration curve in Figure 30 (which includes all the processing conditions). The ratio with air is then determined to be $0.00590 < 1$, which proves that the copper deposition is predominantly in the form of nanoparticles. The level of erosion strongly depends on the chemical composition of plasma atmosphere, meaning the RONS or ROS produced. Clearly, this makes sense since the electrical settings are consistent between gas types. From the SEM images in Figures 27 and 28 of the different copper pin erosions, it is interpreted that the highest level of erosion is achieved with an air atmosphere while the lowest is with argon. ICP-OES analyses support this inference by yielding total copper contents of 1.00 and 0.12 mg/L for air and oxygen, respectively, as seen in Figure 32. In terms of the nanoparticles, PSA-DLS and TEM analyses show that there is a wide range of mean particle diameter for each gas (Figures 33, 34 and 35). This range is a consequence of agglomeration taking place after erosion. DLS gives an estimate on how long agglomeration takes place but is not sufficient enough to reach a conclusion. TEM imaging in Figures 37 and 38 fills in the gaps and asserts that particles produced in air-PAW are the largest with mean diameters rising above 2 microns. Particle sizes are maintained at the nanoscale with oxygen-PAW and argon-PAW having a consistent agglomeration process. Argon-PAW nanoparticles are viewed to structurally agglomerate creating well-organized crystal planes and reaching ~ 500 nm in diameter, while finally oxygen-PAW nanoparticles are the smallest at ~ 200 nm according to PSA-DLS (as consistently interpreted from Figure 36).

From this further study of cathodic erosion in a pin-to-water discharge system, the concept of erosion is better understood in non-thermal plasmas and the synergy of PAW is more properly defined. The combined attribution of both RONS/ROS and metallic content to the application of PAW in several different fields of research is one step closer to being revealed. In the medical field, for example, as a long-term extension to Xudong Su *et al.*'s work on the antimicrobial activity of copper infused PAW[41] from a eukaryotic cellular perspective, a collaborative on-going research with biologists at the Research Center of CHUM in Montreal, Quebec is investigating the cytotoxic activity of air and oxygen-PAW with a copper pin-to-water/phosphate buffered saline (PBS) configuration (PAW samples provided by the PPL at McGill University). The PAW sample is mixed with a cancer/normal cell culture medium for 24 hours. Dead cells can then be counted using a propidium iodide probe or by dying them with methylene blue. Propidium iodide can only penetrate in dead cells to then fluoresce a far-red light. Images will be taken of the cells during the 24-hour period. The selected cells are MCA-205 (a sarcoma cell line), MDA-MB-231 and MCF-

7 (breast cancer cell lines). These cell lines are grown on 96 well plates with the appropriate media for each cell line: RPMI 1% glutamine for MCA and DMEM for the breast cancer cells (both media also include Fetal Bovine Serum and pen/strep). Since the acidity varies as the plasma gas is altered from air to oxygen, the pH of the media must be monitored and buffered accordingly. It is important to note that at a pH ~ 3 the iodide probe is unstable, so assessments of cells must be made based on appearances only. So far, preliminary results have been very promising, showing high cytotoxic efficiency that can be used to counter the development of tumor cells. This thesis can help understand the role each component of PAW plays to create its cytotoxic properties. With RONS already characterized by other researchers, this research gives the momentum needed to completely close the case from the metallic perspective of PAW.

5.2 Future Work and Recommendations

Due to time constraints and the pandemic of 2020, many experimentations were left with missing parts. In the electrochemical section, respective DPASV methods and calibration curves should be constructed for oxygen-PAW and argon-PAW in order to determine all ion:nanoparticle ratios. It is recommended to adapt and readjust the external standards method used to accommodate for the new presented pH's of 4.5 and 5.5, respectively. Another major recommendation is adding rotation to the electrochemical cell where redox reactions take place. This will remove voltage shifts from the calibration curve construction as well as study the effects they have on the stripping peak current. Furthermore, in order to make the interpretations presented in the results chapter more complete, the ICP-OES measurement and TEM imaging for argon and oxygen respectively should be performed in the future. These will complement and verify the trend deduced in SEM-EDS analysis as well as its correlation to particle size. Completing all this missing data will surely result in a publishable scientific article, since there is almost nothing published concerning cathodic erosion in a pin-to-liquid non-thermal plasma discharge system.

After this work is complete, studying nanoparticle size control of copper is highly recommended. Nanoparticle size can be manipulated by altering many aspects of the plasma system, such as reaction chamber temperature, exposure to UV radiation, alteration of electrode polarities, placing precursors of metallic content into the water prior to plasma treatment, replacing aqueous media with pure ionic liquid media and other variables described by Chen *et al*.[66] After a method of nanoparticle design and synthesis is established for copper, a new type of metal cathode can be chosen to be investigated (analogously to this thesis) based on the potency of its properties. Many cathode candidates include silver, stainless steel and hafnium, as they have exhibited healing properties (in the case of silver only)[67] or have been generally unexplored in this field.

6 Appendix

6.1 MATLAB code for the External Standards Methods used in cupric ion analysis

```
Data = [0.000   0000    1.12e-5 3.43e-7
0.010   1.35e-6 1.01e-5 3.54e-7
0.020   2.44e-6 1.02e-5 2.67e-7
0.040   4.04e-6 1.12e-5 1.23e-7
0.060   5.59e-6 1.01e-5 3.44e-7
0.080   8.91e-6 1.02e-5 2.97e-7
0.121   1.43e-5 1.01e-5 1.55e-7];

x = Data(:,1);
y = Data(:,2);
y_unk = Data(:,3);
bl = Data(:,4);
x_exst = x;
y_exst = y;
y_unk_exst = y_unk;
bl_exst = bl;
uncorrected = y;
blank = bl;
err = [0 2.39e-8 4.11e-7 8.08e-8 1.03e-6 1.65e-6 1.02e-6];

[ External_Standards ] = ext_stds_fn( x_exst,y_exst,y_unk_exst,bl_exst )
```

```
function [ External_Standards ] = ext_stds_fn(
x_exst,y_exst,y_unk_exst,bl_exst )
% Function of external standards


% Where  x is the concentration of the standard, y is the signal of the
% standard, y_unk is the signal of replicate measurments of unknown and bl
% is the blank signal.

% N represents the number of standards and M represents the replicate
% unknown measurments.

x = x_exst;
y = y_exst;
y_unk = y_unk_exst;
bl = bl_exst;
err = [0 2.39e-8 4.11e-7 8.08e-8 1.03e-6 1.65e-6 1.02e-6];

% Calculation on N and M

N = length(y);
M = length(y_unk);

% Calculation of average blank signal from blank meansurments

bl_mean = mean(bl);

% Blank correction of the standard and unknown siganls using the average
% blank signal

y = bl_correction_1( y,bl_mean );
y_unk = bl_correction_1( y_unk,bl_mean );

% Calculation of Sxx, Syy, and Sxy

xbar = mean(x);
ybar = mean(y);

i = 1;
Sxx = 0;
Syy = 0;
Sxy = 0;
while i <= length(x)
    Sxx = Sxx + (x(i)-xbar).^2;
    i = i+1;
end
i = 1;
while i <= length(y)
    Syy = Syy + (y(i)-ybar).^2;
    i = i+1;
end
i = 1;
while i <= length(y)
    Sxy = Sxy + (y(i)-ybar).*(x(i)-xbar);
```

```
    i = i+1;
end

% Calculation of slope m and intercept b of the regression line

m = Sxy./Sxx;
b = ybar-m.*xbar;

% Calculation of the errors associated with the regression line: Sy,Sb,Sm

sumxi = 0;
i = 1;
while i<= length(x)
    sumxi = sumxi + x(i);
    i = i+1;
end
sumxi2 = 0;
i = 1;
while i<= length(x)
    sumxi2 = sumxi2 + x(i).^2;
    i = i+1;
end
Sy = ((Syy-(m.^2).*Sxx)./(N-2)).^.5;
Sb = ((Sy.^2)./(N-((sumxi.^2)./sumxi2))).^.5;
Sm = ((Sy.^2)./Sxx).^.5;

% Calculation of the yfit values for the fitted curve using the given
% concentration values x

yfit = m.*x+b;

% Calculation of the regression sum of square SSreg and the total sum of
% squares SStot in order to find the coefficient of determination R2

SSres = 0;
i = 1;
while i<= length(y)
    SSres = SSres + (y(i)-yfit(i)).^2;
    i = i+1;
end
SStot = Syy;
R2 = 1 - (SSres./SStot);

% Calculation of the concentration of the unknown x0

x0 = (mean(y_unk)-b)./m;

% Calculation of the experimental variance Sx0

Sx0 = (Sy./m).*((1./N)+(1./M)+((mean(y_unk)-ybar).^2)./((Sxx.*m.^2))).^.5;

% Calculation of the error of the final concentration at 95% confidence
% interval
```

```
t = tinv(0.975,N-2);
Error = Sx0.*t;

% Creating a single plot to portray results (standrads are points,
% regression line is in red, and the unknown data point is plotted.

figure(1)
plot(x,y, '.b')
errorbar(x,y,err, '.b')
hold on
plot(x,yfit, '-r')
hold on
plot(x0,y_unk, '.g')
hold off

% Label axes using font size 14

xlabel('Concentration(\muM)','FontSize',14)
ylabel('Peak Stripping Current (A)','FontSize',14)

% Plot Title using font size 16

title('Copper External Standards Calibration Curve','FontSize',16)

% Calculation of standard deviation of the blank

stdevbl = std(bl);

% Calculation of the standard deviation of the total signal

stdevts = std(y_unk);

% Calculation of the standard deviation of the analyte signal

stdevas = (stdevbl.^2+stdevts.^2).^.5;

% Calculation of signal to noise ratio

SNR = mean(y_unk)./stdevas;

% Calculation of the precision (CV)

CV = 100./SNR;

% Calculation of the limit of detection (LOD) and limit of quantitation
% (LOQ)

LOD = 3.*stdevbl./m;
LOQ = 10.*stdevbl./m;

% Output check methods sheet

External_Standards = [x0, Error, SNR, CV, LOD, LOQ, m, Sm, b, Sb, Sy, R2];
```

```
end

function [ bl_correction ] = bl_correction_1( uncorrected, blank )

% blank correction of signals general function description

y = uncorrected;
x = blank;
i = 1;

for i=1:length(y)
    y(i) = y(i) - x;
end

bl_correction = y;

end
```

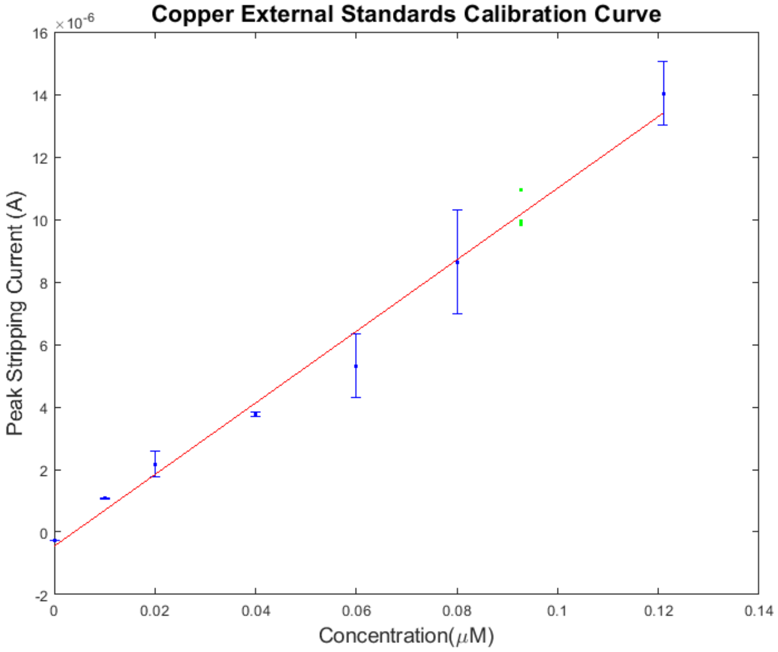

6.2 Average PDIs of the Copper Nanoparticles found with 3 types of gases

Average Polydispersity Index (PDI)	
Cu-Ar	
Sample #1	0.864
Sample #2	0.857
Sample #3	0.737
Cu-Air	
Sample #1	0.720
Sample #2	0.584
Sample #3	0.806
Cu-O2	
Sample #1	0.520
Sample #2	0.555
Sample #3	0.613

6.3 Diffractograms of the TEM Images in Section 4.4.2

For copper nanoparticle found in Argon-PAW

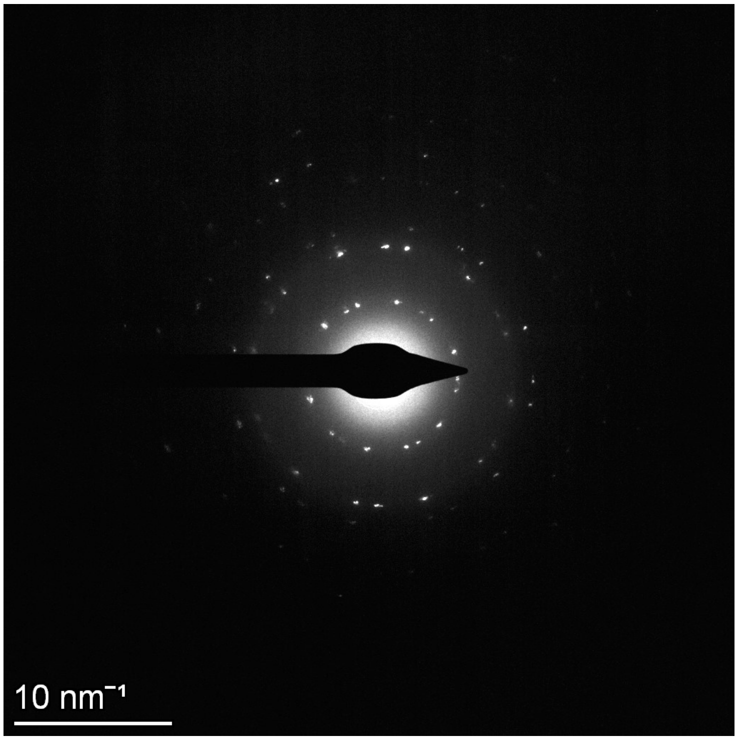

For copper microparticle found in air-PAW

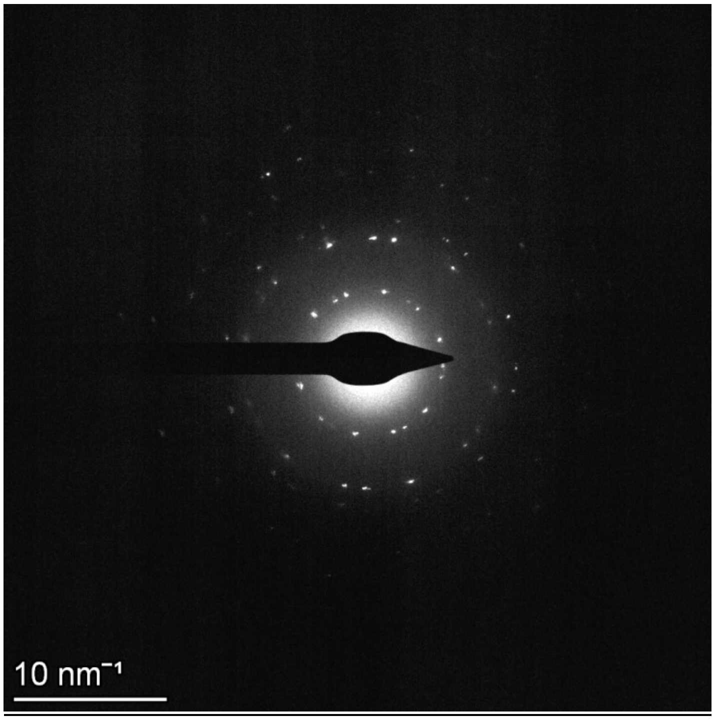

7 References

(1) Gaetke, L. M.; Chow-Johnson, H. S.; Chow, C. K. Copper: Toxicological Relevance and Mechanisms. *Arch. Toxicol.* **2014**, *88* (11), 1929–1938.

(2) Pârvulescu, V. I.; Magureanu, M.; Lukes, P. *Plasma Chemistry and Catalysis in Gases and Liquids*; John Wiley & Sons, 2012.

(3) Puertas, E. C.; Dzafic, A.; Coulombe, S. Investigation of the Electrode Erosion in Pin-to-Liquid Discharges and Its Influence on Reactive Oxygen and Nitrogen Species in Plasma-Activated Water. *Plasma Chem. Plasma Process.* **2020**, *40* (1), 145–167.

(4) Chen, Q.; Li, J.; Li, Y. A Review of Plasma–Liquid Interactions for Nanomaterial Synthesis. *J. Phys. D. Appl. Phys.* **2015**, *48* (42), 424005.

(5) Heyse, P.; Van Hoeck, A.; Roeffaers, M. B. J.; Raffin, J.; Steinbüchel, A.; Stöveken, T.; Lammertyn, J.; Verboven, P.; Jacobs, P. A.; Hofkens, J. Exploration of Atmospheric Pressure Plasma Nanofilm Technology for Straightforward Bio-active Coating Deposition: Enzymes, Plasmas and Polymers, an Elegant Synergy. *Plasma Process. Polym.* **2011**, *8* (10), 965–974.

(6) Zhu, T. VOCs Removal Using the Synergy Technology Basing on Nonthermal Plasma Technology. In *Chemistry, Emission Control, Radioactive Pollution and Indoor Air Quality*; IntechOpen, 2011.

(7) Su, X.; Feng, M.; Rogers, S.; Holsen, T. M.; Thagard, S. M. The Role of High Voltage Electrode Material in the Inactivation of E. Coli by Direct-in-Liquid Electrical Discharge Plasma. *Plasma Chem. Plasma Process.* **2019**, 1–20.

(8) Goldman, M.; Goldman, A.; Sigmond, R. S. The Corona Discharge, Its Properties and Specific Uses. *Pure Appl. Chem.* **1985**, *57* (9), 1353–1362.

(9) Kolikov, V. A.; Kurochkin, V. E.; Panina, L. K.; Rutberg, A. F.; Rutberg, F. G.; Snetov, V. N.; Stogov, A. Y. Prolonged Microbial Resistance of Water Treated by a Pulsed Electrical Discharge. *Tech. Phys.* **2007**, *52* (2), 263–270.

(10) Bruggeman, P. J.; Kushner, M. J.; Locke, B. R.; Gardeniers, J. G. E.; Graham, W. G.; Graves, D. B.; Hofman-Caris, R.; Maric, D.; Reid, J. P.; Ceriani, E. Plasma–Liquid Interactions: A Review and Roadmap. *Plasma sources Sci. Technol.* **2016**, *25* (5), 53002.

(11) Naïtali, M.; Kamgang-Youbi, G.; Herry, J.-M.; Bellon-Fontaine, M.-N.; Brisset, J.-L. Combined Effects of Long-Living Chemical Species during Microbial Inactivation Using Atmospheric Plasma-Treated Water. *Appl. Environ. Microbiol.* **2010**, *76* (22), 7662–7664.

(12) Fridman, A. *Plasma Chemistry*; Cambridge university press, 2008.

(13) Smirnov, B. M. *Fundamentals of Ionized Gases: Basic Topics in Plasma Physics*; John Wiley & Sons, 2012.

(14) Committee, P. S.; Council, N. R. *Plasma Science: From Fundamental Research to Technological Applications*; National Academies Press, 1995.

(15) Radzig, A. A.; Smirnov, B. M. *Reference Data on Atoms, Molecules, and Ions*; Springer Science & Business Media, 2012; Vol. 31.

(16) Neretti, G.; Taglioli, M.; Colonna, G.; Borghi, C. A. Characterization of a Dielectric Barrier Discharge in Contact with Liquid and Producing a Plasma Activated Water. *Plasma sources Sci. Technol.* **2016**, *26* (1), 15013.

(17) Walsh, J. L.; Kong, M. G. Contrasting Characteristics of Linear-Field and Cross-Field Atmospheric Plasma Jets. *Appl. Phys. Lett.* **2008**, *93* (11), 111501.

(18) Bruggeman, P.; Leys, C. Non-Thermal Plasmas in and in Contact with Liquids. *J. Phys. D. Appl. Phys.* **2009**, *42* (5), 53001.

(19) Bruggeman, P.; Guns, P.; Degroote, J.; Vierendeels, J.; Leys, C. Influence of the Water Surface on the Glow-to-Spark Transition in a Metal-Pin-to-Water Electrode System. *Plasma sources Sci. Technol.* **2008**, *17* (4), 45014.

(20) Yamada, T.; Tomaru, N.; Minamitani, Y. The Investigation of the Proceeding Route of the Pulse Streamer Discharge in the Water Treatment by Pulsed Discharge in Air with Droplets of Water. In *2011 IEEE Pulsed Power Conference*; IEEE, 2011; pp 1190–1193.

(21) Van Veldhuizen, E. M.; Rutgers, W. R. Corona Discharges: Fundamentals and Diagnostics. *Invit. Pap. Proc. Front. Low Temp. Plasma Diagn. IV, Rolduc, Netherlands* **2001**, 40–49.

(22) Khalaf, M. K.; Hammadi, O. A.; Kadhim, F. J. Current-Voltage Characteristics of DC Plasma Discharges Employed in Sputtering Techniques. *Iraqi J. Appl. Phys.* **2016**, *12* (3), 11–16.

(23) Zhou, R.; Zhou, R.; Prasad, K.; Fang, Z.; Speight, R.; Bazaka, K.; Ostrikov, K. K. Cold Atmospheric Plasma Activated Water as a Prospective Disinfectant: The Crucial Role of Peroxynitrite. *Green Chem.* **2018**, *20* (23), 5276–5284.

(24) Witzke, M.; Rumbach, P.; Go, D. B.; Sankaran, R. M. Evidence for the Electrolysis of Water by Atmospheric-Pressure Plasmas Formed at the Surface of Aqueous Solutions. *J. Phys. D. Appl. Phys.* **2012**, *45* (44), 442001.

(25) Llewellyn-Jones, F. The Mechanism of Electrode Erosion in Electrical Discharges. *Platin. Met. Rev.* **1963**, *7* (2), 58–65.

(26) Coulombe, S. A Model of the Electric Arc Attachment on Non-Refractory (Cold) Cathodes. McGill University Dissertation 1997.

(27) Kiejna, A.; Wojciechowski, K. F. Work Function of Metals: Relation between Theory and

Experiment. *Prog. Surf. Sci.* **1981**, *11* (4), 293–338.

(28) Smoluchowski, R. Anisotropy of the Electronic Work Function of Metals. *Phys. Rev.* **1941**, *60* (9), 661.

(29) Hölzl, J.; Schulte, F. K. Work Function of Metals. In *Solid surface physics*; Springer, 1979; pp 1–150.

(30) Li, W.; Li, D. Y. Variations of Work Function and Corrosion Behaviors of Deformed Copper Surfaces. *Appl. Surf. Sci.* **2005**, *240* (1–4), 388–395.

(31) Li, W.; Li, D. Y. On the Correlation between Surface Roughness and Work Function in Copper. *J. Chem. Phys.* **2005**, *122* (6), 64708.

(32) Frezza, M.; Hindo, S.; Chen, D.; Davenport, A.; Schmitt, S.; Tomco, D.; Ping Dou, Q. Novel Metals and Metal Complexes as Platforms for Cancer Therapy. *Curr. Pharm. Des.* **2010**, *16* (16), 1813–1825.

(33) Chakhalian, J.; Freeland, J. W.; Habermeier, H.-U.; Cristiani, G.; Khaliullin, G.; Van Veenendaal, M.; Keimer, B. Orbital Reconstruction and Covalent Bonding at an Oxide Interface. *Science (80-.).* **2007**, *318* (5853), 1114–1117.

(34) Cerda, B. A.; Wesdemiotis, C. The Relative Copper (I) Ion Affinities of Amino Acids in the Gas Phase. *J. Am. Chem. Soc.* **1995**, *117* (38), 9734–9739.

(35) Ingle, A. P.; Duran, N.; Rai, M. Bioactivity, Mechanism of Action, and Cytotoxicity of Copper-Based Nanoparticles: A Review. *Appl. Microbiol. Biotechnol.* **2014**, *98* (3), 1001–1009.

(36) Rakhmetova, A. A.; Alekseeva, T. P.; Bogoslovskaya, O. A.; Leipunskii, I. O.; Ol'khovskaya, I. P.; Zhigach, A. N.; Glushchenko, N. N. Wound-Healing Properties of Copper Nanoparticles as a Function of Physicochemical Parameters. *Nanotechnologies*

Russ. **2010**, *5* (3–4), 271–276.

(37) Luza, S. C.; Speisky, H. C. Liver Copper Storage and Transport during Development: Implications for Cytotoxicity. *Am. J. Clin. Nutr.* **1996**, *63* (5), 812S-820S.

(38) Thurman, R. B.; Gerba, C. P.; Bitton, G. The Molecular Mechanisms of Copper and Silver Ion Disinfection of Bacteria and Viruses. *Crit. Rev. Environ. Sci. Technol.* **1989**, *18* (4), 295–315.

(39) Ma, R.; Wang, G.; Tian, Y.; Wang, K.; Zhang, J.; Fang, J. Non-Thermal Plasma-Activated Water Inactivation of Food-Borne Pathogen on Fresh Produce. *J. Hazard. Mater.* **2015**, *300*, 643–651.

(40) Brandenburg, R.; Bogaerts, A.; Bongers, W.; Fridman, A.; Fridman, G.; Locke, B. R.; Miller, V.; Reuter, S.; Schiorlin, M.; Verreycken, T. White Paper on the Future of Plasma Science in Environment, for Gas Conversion and Agriculture. *Plasma Process. Polym.* **2019**, 1700238.

(41) Su, X.; Feng, M.; Rogers, S.; Holsen, T. M.; Thagard, S. M. The Role of High Voltage Electrode Material in the Inactivation of E. Coli by Direct-in-Liquid Electrical Discharge Plasma. *Plasma Chem. Plasma Process.* **2019**, 1–20.

(42) Skoog, D. A.; Holler, F. J.; Crouch, S. R. *Principles of Instrumental Analysis*; Cengage learning, 2017.

(43) Harris, D. C. *Quantitative Chemical Analysis*; Macmillan, 2010.

(44) Kissinger, P.; Heineman, W. R. *Laboratory Techniques in Electroanalytical Chemistry, Revised and Expanded*; CRC press, 2018.

(45) Cammann, K. *Working with Ion-Selective Electrodes: Chemical Laboratory Practice*; Springer Science & Business Media, 2012.

(46) Copeland, T. R.; Skogerboe, R. K. Anodic Stripping Voltammetry. *Anal. Chem.* **1974**, *46* (14), 1257A-1268a.

(47) Bard, A. J.; Rubenstein, I. *Electroanalytical Chemistry: A Series of Advances*; CRC press, 1996; Vol. 19.

(48) Osteryoung, R. A.; Christie, J. H. Theoretical Treatment of Pulsed Voltammetric Stripping at the Thin Film Mercury Electrode. *Anal. Chem.* **1974**, *46* (3), 351–355.

(49) ISO, I. S. O. 9276-2 Representation of Results of Particle Size Analysis—Part 2: Calculation of Average Particle Sizes/Diameters and Moments From Particle Size Distributions. ISO Geneva: 2001.

(50) Olson, E. Particle Shape Factors and Their Use in Image Analysis Part 1: Theory. *J. GXP Compliance* **2011**, *15* (3), 85.

(51) ASTM, E. 799-03 Standard Practice for Determining Data Criteria and Processing for Liquid Drop Size Analysis; American Society for Testing and Materials, 1992.

(52) ISO, B. S. 13320. Particle Size Analysis-Laser Diffraction Methods. *ISO Stand. Auth.* **2009**.

(53) Hallett, F. R. Particle Size Analysis by Dynamic Light Scattering. *Food Res. Int.* **1994**, *27* (2), 195–198.

(54) Studer, A. M.; Limbach, L. K.; Van Duc, L.; Krumeich, F.; Athanassiou, E. K.; Gerber, L. C.; Moch, H.; Stark, W. J. Nanoparticle Cytotoxicity Depends on Intracellular Solubility: Comparison of Stabilized Copper Metal and Degradable Copper Oxide Nanoparticles. *Toxicol. Lett.* **2010**, *197* (3), 169–174.

(55) Nicholls, D. *Complexes and First-Row Transition Elements*; Macmillan International Higher Education, 2017.

(56) Cotton, F. A.; Wilkinson, G.; Gaus, P. L. Basic Inorganic Chemistry,(1995). John Wiley & Sons, New York.

(57) Zhuang, J.; Zhang, L.; Lu, W.; Shen, D.; Zhu, R.; Pan, D. Determination of Trace Copper in Water Samples by Anodic Stripping Voltammetry at Gold Microelectrode. **2011**.

(58) Ives, D. J. G.; Janz, G. J.; King, C. V. Reference Electrodes: Theory and Practice. *J. Electrochem. Soc.* **1961**, *108* (11), 246C.

(59) Sukeri, A.; Bertotti, M. Nanoporous Gold Surface: An Efficient Platform for Hydrogen Evolution Reaction at Very Low Overpotential. *J. Braz. Chem. Soc.* **2018**, *29* (2), 226–231.

(60) Jeyabharathi, C.; Ahrens, P.; Hasse, U.; Scholz, F. Identification of Low-Index Crystal Planes of Polycrystalline Gold on the Basis of Electrochemical Oxide Layer Formation. *J. Solid State Electrochem.* **2016**, *20* (11), 3025–3031.

(61) Burke, L. D.; Nugent, P. F. The Electrochemistry of Gold: I the Redox Behaviour of the Metal in Aqueous Media. *Gold Bull.* **1997**, *30* (2), 43–53.

(62) Grishina, E. P.; Udalova, A. M.; Rumyantsev, E. M. Anodic Oxidation of Copper in Concentrated Sulfuric Acid Solutions. *Russ. J. Electrochem.* **2002**, *38* (9), 1041–1045.

(63) Instruments, M. Zetasizer Nano Series User Manual. *MAN0317* **2004**, *1*, 2004.

(64) Dhineshbabu, N. R.; Rajendran, V.; Nithyavathy, N.; Vetumperumal, R. Study of Structural and Optical Properties of Cupric Oxide Nanoparticles. *Appl. Nanosci.* **2016**, *6* (6), 933–939.

(65) Ju, H.; Leech, D. Effect of Electrolytes on the Electrochemical Behaviour of 11-(Ferrocenylcarbonyloxy) Undecanethiol SAMs on Gold Disk Electrodes. *Phys. Chem. Chem. Phys.* **1999**, *1* (7), 1549–1554.

(66) Chen, Q.; Li, J.; Li, Y. A Review of Plasma–Liquid Interactions for Nanomaterial Synthesis. *J. Phys. D. Appl. Phys.* **2015**, *48* (42), 424005.

(67) Atiyeh, B. S.; Costagliola, M.; Hayek, S. N.; Dibo, S. A. Effect of Silver on Burn Wound Infection Control and Healing: Review of the Literature. *burns* **2007**, *33* (2), 139–148.